

⁸⁷**Rubidium Bose-Einstein condensates: Machine
Construction and Quantum Zeno Experiments**

by

Erik William Streed

Submitted to the Department of Physics
in partial fulfillment of the requirements for the degree of

Doctor of Philosophy

at the

MASSACHUSETTS INSTITUTE OF TECHNOLOGY

January 2006

© Massachusetts Institute of Technology 2006. All rights reserved.

Author
Department of Physics
January 9, 2006

Certified by
Wolfgang Ketterle
John D. MacArthur Professor of Physics
Thesis Supervisor

Certified by
David E. Pritchard
Cecil and Ida Green Professor of Physics
Thesis Supervisor

Accepted by
Thomas J. Greytak
Professor of Physics, Associate Department Head for Education

⁸⁷Rubidium Bose-Einstein condensates: Machine Construction and Quantum Zeno Experiments

by

Erik William Streed

Submitted to the Department of Physics
on January 9, 2006, in partial fulfillment of the
requirements for the degree of
Doctor of Philosophy

Abstract

This thesis details construction of a new apparatus for the production of ⁸⁷Rb Bose-Einstein condensates and a subsequent quantum Zeno effect experiment.

An experimental apparatus for producing large Bose-Einstein condensates of ⁸⁷Rb is described in detail. A high flux thermal atomic beam is decelerated by a Zeeman slower and is then captured and cooled in a magneto-optical trap. The atoms are then transferred into a cloverleaf style Ioffe-Pritchard magnetic trap and cooled to quantum degeneracy with radio frequency induced forced evaporation. Condensates containing up to 20 million atoms can be produced every few minutes.

The quantum Zeno effect is the suppression of transitions between quantum states by frequent measurement. Oscillation between two ground hyperfine states of a magnetically trapped ⁸⁷Rb Bose-Einstein condensate, externally driven at a transition rate ω_R , was substantially suppressed by destructively measuring one of the levels with resonant optical scattering. While an ideal continuous measurement will stop the transition, any real measurement method will occur at a finite rate. The suppression of the transition rate in the two level system was quantified for pulsed measurements with a time between pulses δt and weak continuous measurements with a scattering rate γ . We observe that the weak continuous measurements exhibit the same suppression in the transition rate as the pulsed measurements when $\gamma\delta t = 3.60(0.43)$. This is in agreement with the previously predicted value of 4. Increasing the measurement frequency suppressed the transition rate to $0.005\omega_R$.

Thesis Supervisor: Wolfgang Ketterle
Title: John D. MacArthur Professor of Physics

Thesis Supervisor: David E. Pritchard
Title: Cecil and Ida Green Professor of Physics

**“The universe is a surprisingly benevolent place.” -Prof. Daniel
Kleppner**

Acknowledgments

No man is an island. No thesis is solely the work of one person. I must express my gratitude to the many people who have assisted me. First I must acknowledge my research advisers Wolfgang Ketterle and Dave Pritchard. They have vastly expanded the frontiers of condensed matter and atomic physics. Both are blessed with keen insight into the nature of scientific discovery. To my original academic adviser Dan Kleppner, for allowing me to defer enrollment for a year and whose sage observation adorns this tome. My lab mates Dominik Schenble, Yoshio Torii, Mindy Kellogg, Micah Boyd, Gretchen Campbell, Jongchul Mun, and Patrick Medley are all good people to work with and were generally tolerant of my quirks. Two undergraduate researchers Xin "James" Sun and Pavel Gorelick were intrepid enough to be my advisees during the construction phase of the Rubidium BEC machine. I hope they benefited as much from the experience as I did. Fred Cote who recently retired from supervising the Student Shop and Carol Costa our departed group secretary are two very special people who both strove to make MIT a more humane place. Maxine Samuels, Lorraine Simmons, Mary Young, Dave Foss, Al McGurl and Bill Gibbs of the Research Laboratory for Electronics provided excellent support to all of us in the Ketterle group. Samson Timoner provided me with motivation from beyond the pale edge of graduation, the MIT thesis LaTeX files, and occasionally a car. Wren Montgomery demonstrated for me that graduate school can be much much worse, but also that it can get much much better. Dave Kielpinski, my future boss, presented me with an offer I couldn't refuse. For my grounding in mathematics I must give credit to the University of Minnesota Talented Youth in Mathematics Program. To my parents Pam and Karl Streed, without whom I wouldn't have made it this far.

I'd also like to thank my girlfriend Allison Roberts and my brother Kurt Streed for being there when I really needed it.

Construction of the ^{87}Rb Bose-Einstein condensate machine was supported by the United States National Science Foundation (NSF) Center for Ultracold Atoms (CUA). The Quantum Zeno experiments were supported by the United States Army Research Office MURI program and the CUA.

Contents

1	Preface	8
2	Introduction	10
2.1	On Bose-Einstein Condensation	10
2.1.1	The Phase Transition	13
2.1.2	Properties of a Pure Condensate	13
2.1.3	Loss processes	15
3	A large atom number ^{87}Rb Bose Einstein Machine	18
3.1	System Overview	18
3.2	High Flux Rb Oven	21
3.2.1	Effusive Ovens	21
3.2.2	Operation	23
3.2.3	Design table	25
3.3	Zeeman Slower	25
3.3.1	Slower Construction	28
3.4	Lasers	29
3.4.1	Fiber Coupling	31
3.4.2	Injection Locking	32
3.5	Computer Control and Imaging	32
3.5.1	Free Expansion	33
3.5.2	State Analysis	34
3.5.3	Repumping effects	34
3.5.4	Camera	35
3.6	Magneto Optical Trap	35
3.7	Magnetic Trapping	36
3.7.1	Fields in a Ioffe-Pritchard Magnetic Trap	36
3.7.2	Circuitry	39
3.7.3	Turnoff	42
3.7.4	Wire	43
3.7.5	Cooling	44

3.7.6	Fabrication	45
3.8	Evaporation	45
3.9	Anomalous Losses in Deep Traps	47
3.9.1	Motivation	47
3.9.2	Technique	47
3.9.3	Theory	48
3.9.4	Results	48
4	The Quantum Zeno Effect in Bose-Einstein Condensate	51
4.1	Previous Works	51
4.1.1	Pulsed Measurements	53
4.1.2	Continuous Measurement	53
4.1.3	Relevance	55
4.1.4	Limitations	55
4.2	Implementation	56
4.2.1	Two level system	56
4.2.2	State Measurement by Light Scattering	61
4.2.3	Simultaneous Detection	62
4.2.4	Pulsed Measurement Experiments	64
4.2.5	Continuous Measurement Experiments	68
4.3	Technical Limitations	71
4.3.1	Optical Opacity	71
4.3.2	RF Detuning	73
4.3.3	Clock shift	75
4.3.4	Polarization	76
4.3.5	Superradiance	76
4.3.6	Collisions	77
4.4	Conclusions	79
A	Rubidium Oven Plans	81
B	Publication: Large Atom Number BEC Machines	90
C	Publication: Continuous and Discrete Quantum Zeno Effect	106
D	Degenerate Bose gases in one and two dimensions	112
D.1	Confinement to one dimension	112
D.1.1	Tonks-Girardeau Transition	113
D.2	Confinement to two dimensions	114
D.2.1	Berezinskii-Kosterlitz-Thouless Transition	114

E Rubidium Properties	117
E.1 Physical Properties of Rubidium	117
E.1.1 Vapor Pressure	118
E.1.2 Spectroscopy Cell Maintenance	118

Chapter 1

Preface

Dear Reader,

This is a physics thesis. I have written down extensive technical details on the construction of a machine built at MIT to produce Bose-Einstein condensates of ^{87}Rb atoms. In addition I describe the results of a series of experiments demonstrating the quantum Zeno effect performed with this apparatus. Before diving into these topics I'd like to use this space to place my graduate work in a much broader context and voice some concerns for the future. I live in a society that is increasingly dominated by the effects from advances in science and changes in technology. The rapidly crumbling barriers to accessing many types of information has increased the velocity at which scientific research is performed. Several segments of western society and other societies have reacted adversely to these changes. The consequences of these reactions has impacted United States science policy and influenced the direction of my personal and professional lives.

During my adult lifetime I have witnessed a dramatic change in the accessibility of information through the Internet. In the summer of 1996 I worked as an undergraduate research assistant for Prof. John Roberts at Caltech. I investigated the conformational chemistry of β -alanine [1] by varying the dielectric constant of the surrounding solvent. Prior to starting this job I had broken my foot and was in a cast for most of the summer. I spent a miserable week limping around Millikan Library, chasing down articles listed in Chemical Abstracts to find information on the the temperature dependence of the dielectric constant of ethanol/water solutions [2]. With the changes brought about by the Internet, today this same task would take me less than three minutes. An inexperienced undergrad might require an hour or two to retrieve the relevant information. This ease of access to a broad variety of information will continue to profoundly change our lives into the foreseeable future.

However ease of access to information should not be confused with dissemination of knowledge or the development of wisdom. One of the places that these differences are most important is the growing debate over the place and function of science in our society. Currently these contentions revolve around questions in the biological realm regarding the nature and origin of life. Contention between Darwin's theory of evolution and religious

beliefs has lead to temporary corruptions of science education in Kansas, Pennsylvania, and Georgia. Some scientific discoveries, such as that the earth is flat, are at odds with certain religious teachings. However many others can be reconciled by clearly delineating the bounds of science. Namely that science is composed of theories which are disprovable. The universe is much more then this. I predict that the emerging rift between the scientific community and communities of faith (Christian, Muslim, etc.) will increase to a dangerous degree unless active measures are taken to demarcate this difference.

The reduction of financial support by the federal government to research in the physical sciences has been influenced by the priorities of religious groups within the United States. Upon completion of my graduate program at MIT I will undertake a post doctoral appointment at Griffith University in Brisbane, Australia. Budget cuts to science programs have unquestionably contributed to my employment outside of the country. While I feel my return to the United States is likely, it is by no means certain in an era of declining funding for my field.

Erik

Chapter 2

Introduction

This is a thesis about the quantum nature of our universe. Most of our daily experiences can readily be explained by the classical mechanics of Newton and electromagnetic theory of Maxwell. The quantum nature of our universe is both subtle and profound in its impact. Negatively charged electrons do not spiral into the positive charge of the atomic nuclei because uncertainty in their position and momentum balances localization around the nucleus against their rate of movement about the region. A quantum state can exist in a superposition of many different states with differing characteristics so long as one does not measure it.

That quantum mechanics successfully predicts physical phenomena is sufficient to satisfy quantum pragmatists, who view the theory only as a means to an end. However, quantum idealists are concerned by what monsters might be masked in its mechanisms. This thesis touches both topics. First there is a description of the construction, characterization, and operation of a machine to cool ^{87}Rb from a boiling hot vapor to ultra cold temperatures a few billionths of a degree above absolute zero. At these low temperatures the quantum state of Bose-Einstein condensate can be achieved for experimentally obtainable densities. The second component of this thesis details an experimental demonstration of the Quantum Zeno effect, where measurements are used to inhibit quantum dynamics and partially freeze a two level system in its initial state. The Quantum Zeno effect is an essential experiment in quantum mechanics since it relates the quantum system to the classical measurement apparatus.

2.1 On Bose-Einstein Condensation

Bose-Einstein condensation is both a particular and peculiar state of matter. It was first suggested by Einstein [3], who applied the statistical model Bose [4] used for photons to particles. Bose derived the Planck's formula for black body radiation, a well established experimental phenomena, from statistical considerations. Einstein predicted that for particles the entire system would occupy the ground state at sufficiently low temperatures. This

transition from a classical thermal gas to a quantum degenerate Bose-Einstein condensate occurs when the phase space density, $\rho = n\lambda_{dB}^3$ is increased to ~ 1 , where n is the number density of particles per unit volume and λ_{dB} is the thermal de Broglie wavelength [5] of the atoms. In quantum mechanical terms phase space density is the probability of finding an atom in a particular state.

So in principle, getting a BEC is easy: you simply cool down until the critical phase space density is reached. In practice, the procedure is more complicated. The physics of different cooling techniques limit the range of their effectiveness. Ice water is very good at cooling down a hot coffee, but will not get you very far in making liquid helium. This thesis describes the variety of different techniques used to both cool the atoms and increase their density. Table 2.1 shows how we increase phase space density by roughly 16 orders of magnitude to achieve Bose-Einstein condensation in ^{87}Rb .

To put this number in perspective, the difference in number between you, the reader, occupying a single seat in a stadium and an entire stadium full of people is four to five orders of magnitude. The difference in number between you, the reader, and all the other people on the planet is between 9 and 10 orders of magnitude. Combining these two if every person on the planet were in the unlikely position of carrying a stadium in their pocket, what our Bose-Einstein condensate machine does is to reduce the situation of an atom from possibly being located in any seat in any pocket of any person to one particular seat we have designated in our pocket. This seat, or quantum state, has the fortunate distinguishing property of being the lowest energy state. By cooling, or successively persuading the atom to forsake the higher energy seats we can condense it down to one particular location. While astrophysicists may work with a greater range of phenomena, their systems can't be contained in a single lab, nor can an experiment be triggered with the push of a single button.

Prior to 1995 Bose-Einstein condensation of particles was limited to explaining the superfluid properties of cryogenic liquid ^4He below the Λ transition at 2.2K. Most solid material, like the stainless steel used to construct vacuum and cryogenic chambers, has strong interactions between its components which prevent the de Broglie wavelength from increasing much beyond the size of an atom-atom bond length. The attraction between ^4He atoms is the weakest of any traditional condensed matter system, enough so that the BEC transition can be approached in the liquid state. Unfortunately even though the interaction is weak, the high densities present in this system complicate theoretical modeling.

The development of laser cooling techniques [6–13] in the 1980's revolutionized the field of atomic physics and resulted in the awarding of 1997 Nobel Prize in Physics [14–16] to several pioneers in the field. The temperatures reached by these techniques, a few millionths of a degree above absolute zero, and were far below that reached through cryogenic methods. It became conceivable that laser cooled atoms could be further chilled and their density increased to the point of Bose-Einstein condensation. While subsequent laser cooling tech-

Stage	n (/cm ³)	Temperature	Velocity ^a	ρ
Oven	10^{13}	383K	334 m/s	10^{-14}
Thermal Beam	10^7	n/a	334 m/s	10^{-20}
Slowed Beam	10^7	n/a	43 m/s	10^{-18}
Loading MOT ^b	10^{10}	150 μ K	210 mm/s	10^{-7}
Compressed MOT ^b	10^{11}	300 μ K	300 mm/s	4×10^{-7}
Molasses ^b	10^{11}	10 μ K	54 mm/s	6×10^{-5}
Magnetic trap	10^{11}	500 μ K	380 mm/s	2×10^{-7}
BEC Transition	3×10^{13}	500 nK	12 mm/s	2.61
Pure BEC	10^{14}	250 nK ^c	8.5 mm/s	100

Table 2.1: Typical phase space densities (ρ) during BEC production. Numbers given are for the ⁸⁷Rb apparatus.

^amost probable

^bTypical values, not measured separately

^cChemical potential

niques were able to approach but not reach condensate, an alternative technique of radio frequency induced evaporative cooling used by groups at MIT, U. Colorado, and Rice led to the achievement of condensation in 1995. The 2001 Nobel Prize in Physics would subsequently be awarded to three of these investigators [17, 18]. Major work by many groups around the world has now extended these cooling techniques to an impressive number of atomic species: ⁸⁷Rb [19], ²³Na [20], ⁷Li [21, 22], ¹H [23], ⁸⁵Rb [24], ⁴He* [25, 26], ⁴¹K [27], ¹³³Cs [28], ¹⁷⁴Yb [29], and ⁵²Cr [30]. Recent informal discussions have suggested that a Strontium isotope may be the next contender to join the list of condensed atoms.

A distinguishing characteristic of most Bose-Einstein experimental apparatuses is the method in which atoms are laser cooled and then loaded into a trap for evaporative cooling. Our approach at MIT employs atomic ovens and Zeeman slowing. Other approaches use variations of a vapor cell magneto-optical trap (MOT), in a double MOT configuration, surface MOT [31], or as a source of low velocity atoms [32, 33]. An important figure of merit of a BEC experiment is the number of atoms in the condensate. Large atom number allows better signal-to-noise ratios, greater tolerance against misalignments, and greater robustness in day-to-day operation. Since 1996, the MIT sodium BEC setups have featured the largest alkali condensates. They routinely produce condensates with atom numbers between 20 and 100 million. Since the diode lasers used to cool rubidium are less expensive and more reliable than the dye lasers needed for sodium, most new groups have chosen to work with rubidium. The majority of rubidium experiments use vapor cell MOTs, however the typical sizes of the condensates created with vapor cells MOTs are smaller than those

realized with a Zeeman slower. The construction of vapor cell MOT rubidium condensate machines is extensively detailed in the literature [34].

When the Center for Ultracold Atoms was created at MIT and Harvard, a major goal for the Center was to create ^{87}Rb condensates with large atom number using the techniques developed for ^{23}Na condensates. A large part of my graduate career at MIT was spent transferring these techniques and constructing our ^{87}Rb BEC machine.

The most recent, third-generation, sodium and rubidium experiments at MIT were both designed with an additional vacuum chamber (“science chamber”) into which cold atoms can be moved using optical tweezers. The multi-chamber design allows us to rapidly reconfigure the experimental setup in the science chambers while keeping the BEC production chamber under vacuum. This has allowed very different experiments to be performed in rapid succession [35–46] without major modifications to the BEC production side of the machine.

2.1.1 The Phase Transition

The Bose-Einstein condensation phase transition occurs when the uncertainty in each particles location, or the de Broglie wavelength $\lambda_{dB} = \sqrt{\frac{2\pi\hbar^2}{k_B T m}}$ is close to the spacing between particles $n^{-1/3}$, or more specifically $n\lambda_{dB}^3 \approx 2.612$. As the atoms are cooled into the condensate their energy is dominated by atom-atom interactions rather than their kinetic energy (the Thomas-Fermi limit).

This is not a feature of an ideal condensate, but an effect specific to the condensed species atomic state. The energy from the atom atom interactions is known in the Bose-Einstein condensate literature as the mean field energy. It is proportional to the density and the s-wave scattering length. In the Thomas-Fermi approximation the mean field energy (V_{int}) of the condensate matches the potential energy (V_{trap}) and both greatly exceed the kinetic energy. In a condensate the sum of the two is equal to the chemical potential (μ) such that the density is complementary to the shape of the potential ($V_{int} + V_{trap} = \mu$). The result of this phase transition is shown in Fig. 2-1, where the dramatic difference in profile between the thermal and BEC atoms is shown. Of particular note is the extremely high peak density in a condensate accompanied by a sharp edge in the distribution due to the fixed energy or chemical potential of the condensate. The thermal distribution has a statistical distribution of energy among its atoms resulting in a boundary that is fuzzy.

2.1.2 Properties of a Pure Condensate

The edge of the condensate is defined by the Thomas-Fermi radius r_i , where the potential energy matches the chemical potential from the mean field. In a harmonic trap this results in a parabolic spatial distribution of the density $n(x, y, z)$

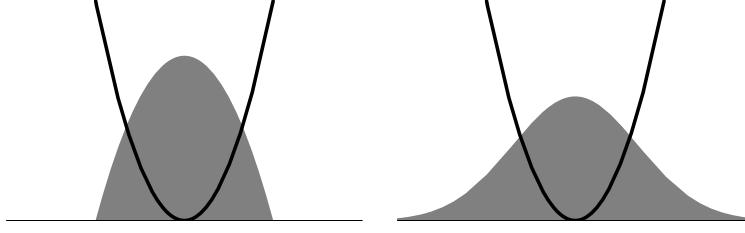


Figure 2-1: Distribution of atoms in a harmonic trap for BEC (left) and thermal (right) states in 1 dimension. The BEC profile complements that of the trapping potential and has a sharp boundary. The thermal profile is more diffuse and has a fuzzy boundary.

$$n(x, y, z) = n_p \sqrt{1 - \frac{x^2}{r_x^2} - \frac{y^2}{r_y^2} - \frac{z^2}{r_z^2}} \quad (2.1)$$

where n_p is the peak density. Integrating this density over the occupied ellipsoid where $n(x, y, z) > 0$ gives a total atom number

$$N = \frac{8\pi}{15} r_x r_y r_z n_p \quad (2.2)$$

with the average density throughout the occupied volume $\bar{n} = \frac{2}{5} n_p$. At the center of the trap the potential energy vanishes and the chemical potential is entirely that of the mean field

$$\mu = \frac{4\pi\hbar^2 a}{m} n_p \quad (2.3)$$

where m is the mass of the particle and a is the s-wave scattering length.

Moving out from the center of the condensate to the end, the harmonic trapping potential energy

$$U_{trap} = \frac{1}{2} m (\omega_x^2 x^2 + \omega_y^2 y^2 + \omega_z^2 z^2) \quad (2.4)$$

is equal to the mean field chemical potential at the point where the density drops to zero.

$$\mu = \frac{1}{2} m \omega_x^2 r_x^2 \quad (2.5)$$

$$\mu = \frac{1}{2} m \omega_y^2 r_y^2 \quad (2.6)$$

$$\mu = \frac{1}{2} m \omega_z^2 r_z^2 \quad (2.7)$$

Combining these, we can solve for the chemical potential μ in terms of the number of atoms N

$$\mu = \frac{\hbar\bar{\omega}}{2} \left(15N \frac{a}{\bar{a}} \right)^{2/5} \quad (2.8)$$

where $\bar{\omega} = (\omega_x\omega_y\omega_z)^{1/3}$ is the geometric mean trap frequency and $\bar{a} = \sqrt{\frac{\hbar}{m\bar{\omega}}}$ is the geometric mean of the quantum harmonic oscillator length. This formula can also be recast to determine the peak density n_p from the atom number N .

$$n_p = \left(\frac{225N^2}{8\pi a^3 \bar{a}^{12}} \right)^{1/5} \quad (2.9)$$

2.1.3 Loss processes

Trapping ultracold atoms requires that they be isolated from the surrounding environment. The laser and magnetic trapping techniques confine the atoms, out of contact with the room temperature chamber walls. Collisions with background gas molecules result in loss from the trap, requiring low vacuum pressure for long atom cloud lifetime. At the high densities found in condensates, two and three body inelastic scattering processes can also result in heating and loss of atoms from the trap. The trapped atoms are surrounded by the room temperature black body radiation from the chamber walls. In cryogenic liquid helium systems this would cause extremely rapid heating because of the relatively large optical absorption cross section. The trapped alkali atoms are transparent to almost all of the black body spectrum due to their sparse and narrow linewidth transitions and are generally decoupled from the influence of this radiation.

Vacuum Pressure

At nanokelvin temperatures, all room temperature particles are extremely energetic in comparison with the trapped atoms. A collision with a background particle will typically impart enough energy to knock an ultracold atom out of the trap. This process occurs at a constant rate, independent of density, temperature or phase state (thermal vs. BEC). The small scattering cross section between the background particles and the trapped atoms allows us to magnetically trap ultracold atomic clouds with lifetimes of several minutes in the $< 10^{-11}$ torr ultrahigh vacuum (UHV) environment of the main production chamber. This duration is far longer than any experiments we will likely attempt in the near future and effectively sets the background decay rate at zero. Attempts to measure this lifetime accurately ran into the technical limitation of our control computer only being able to hold sequences less than about five minutes in length due to memory constraints.

To achieve pressures $< 10^{-11}$ torr we have followed the general guidelines set out in Ref. [47] for constructing vacuum systems. The main chamber body was constructed of nonmagnetic 304 stainless steel and then electropolished to reduce the surface roughness. To minimize the number of components inside the vacuum system the magnetic trap coils are placed outside the vacuum chamber. Informal discussion with groups that magnetic trap coils inside the chamber report that they are vulnerable to coupling in RF noise from switching high current power supplies, resulting in anomalous trap losses. The only com-

ponent placed inside our main vacuum chamber was the RF evaporation antenna (Fig. 3-2).

In the science chamber vacuum pressure can be a limiting factor. The science chamber typically has several pieces of hardware inside the vacuum system, such as wire traps, coils, or specially prepared materials such as hard drive platters. These specialty items often cannot be baked at the high temperatures used in the main chamber. Instead the science chamber is baked out to $\sim 10^{-10}$ torr without the temperature sensitive materials to reduce the gas load when the temperature sensitive materials are installed. Typical science chamber lifetimes are a few minutes, longer than the few seconds typically needed for a typical experiment.

Inelastic collisions

Inelastic collisions are a dominant source of losses at BEC densities. In collisions between two or three particles, the state of the product particles can change so long as overall physical quantities such as energy, momentum, and angular momentum are conserved. Dipolar relaxation is an inelastic collision process where changes in the internal states of the atoms is converted to kinetic energy. Atoms in spin states $|F, m_F\rangle$ which are “stretched” (e.g. $F = |m_F|$) do not undergo spin relaxation at low magnetic field since changing spin states would violate conservation of angular momentum. At higher magnetic field the mixing between states breaks down this conservation as atoms in a particular state will have characteristics of several $|F, m_F\rangle$ states. By further increasing the magnetic field the angular momentum of the electron and nuclear spins decouple and are conserved separately, inhibiting dipolar relaxation. The low field $|F, m_F\rangle$ basis is appropriate for describing the states of the ^{87}Rb atoms in our magnetic trap.

If three atoms undergo a simultaneous collision three body recombination can occur, resulting in the production of an dimer molecule and atom pair. The energy driving these collisions is the binding energy associated with the product molecular vibrational levels rather than hyperfine energy differences in dipolar collisions. Three body decay is often the dominant source of intrinsic losses in ^{87}Rb Bose-Einstein condensates.

Calculating measurable loss rates for two and three body processes in condensates requires converting between the peak density n_p and the first and second order density moments $\langle n \rangle$ and $\langle n^2 \rangle$. The generic density weighted function

$$\langle \eta \rangle = \frac{1}{N} \int \eta(\vec{r}') n(\vec{r}') d^3 \vec{r}' \quad (2.10)$$

gives first and second order density moments $\langle n \rangle = \frac{2}{7} n_p$ and $\langle n^2 \rangle = \frac{8}{21} n_p$ for a BEC in the Thomas-Fermi limit. For three body decay the atom loss rate is $\Gamma_3 = K_3 \langle n^2 \rangle = K_3 \frac{8}{21} n_p^2$. Both the two and three body decay processes are concentrated at the center of the trap, where the highest densities occur.

Blackbody Radiation

The trapped atoms are exposed to black body radiation from the surrounding room temperature chamber, but are transparent to most of the spectrum. The transitions to which the black body radiation can couple are the optical transitions used for laser cooling and the microwave hyperfine transitions. For optical transitions, which have energies much greater than $k_B T$, the excitation rate is $\frac{3}{\tau_{opt}} \exp(-\hbar\omega_{opt}/k_B T)$, where ω_{opt} is the frequency of the transition and τ_{opt} is the lifetime of the excited state. For rubidium in a 25°C chamber this gives a characteristic excitation lifetime of $\sim 10^{11}$ years. Raising the chamber temperature to 680°C increases the optical excitation rate into the experimentally relevant domain of once per minute. The hyperfine transitions are significantly lower in energy compared to $k_B T$ and have an excitation rate of $\frac{3}{\tau_{hfs}} \frac{k_B T}{\hbar\omega_{hfs}}$, which is once per year at 25°C in ^{87}Rb . Neither of these excitation rates are limitations on current experiments.

Chapter 3

A large atom number ^{87}Rb Bose Einstein Machine

This chapter contains an expanded version of the portions of "Large atom number Bose-Einstein Condensate machines" [48] specific to the ^{87}Rb BEC machine. Material edited from the published version is included here. Appendix B contains a copy of the manuscript RSI MS# A050544R as accepted for publication on December 13, 2005.

3.1 System Overview

Fig. 3-1 shows the layout of our vacuum system. An ultracold Bose-Einstein condensate is made through a four stage process. In the first stage a thermal beam of rubidium atoms emanates from the oven. Next, the ^{87}Rb atoms in the beam are decelerated with the Zeeman slower. In the main chamber, these slowed atoms are captured and cooled with a six-beam magneto-optical trap (MOT) [9], constituting the third stage. The MOT is loaded with atoms from the Zeeman slower until it reaches equilibrium. To begin an experiment and start the final stage the atoms are optically pumped into the $F=1$ hyperfine ground state. Turning on the Ioffe-Pritchard magnetic trap captures atoms in the weak field seeking $F=1, m_F=-1$ state. The trapped atoms are evaporatively cooled by removing hotter atoms through radio frequency (RF) induced transitions to untrapped states. Reducing the RF frequency lowers the effective depth of the magnetic trap, allowing us to progressively cool to higher densities and lower temperatures until the atoms reach BEC. Magnetically trapped atoms in the $F=2, m_F=+2$ state have also been evaporated to BEC.

Ultracold atoms can be transported from the main chamber into the science chamber by loading the atoms into the focus of an optical tweezer and then translating the focus. In this manner ^{23}Na BECs were transported [35]. The axes of the oven and Zeeman slower are tilted by 57° from horizontal to allow a horizontal orientation for the weak trapping axes

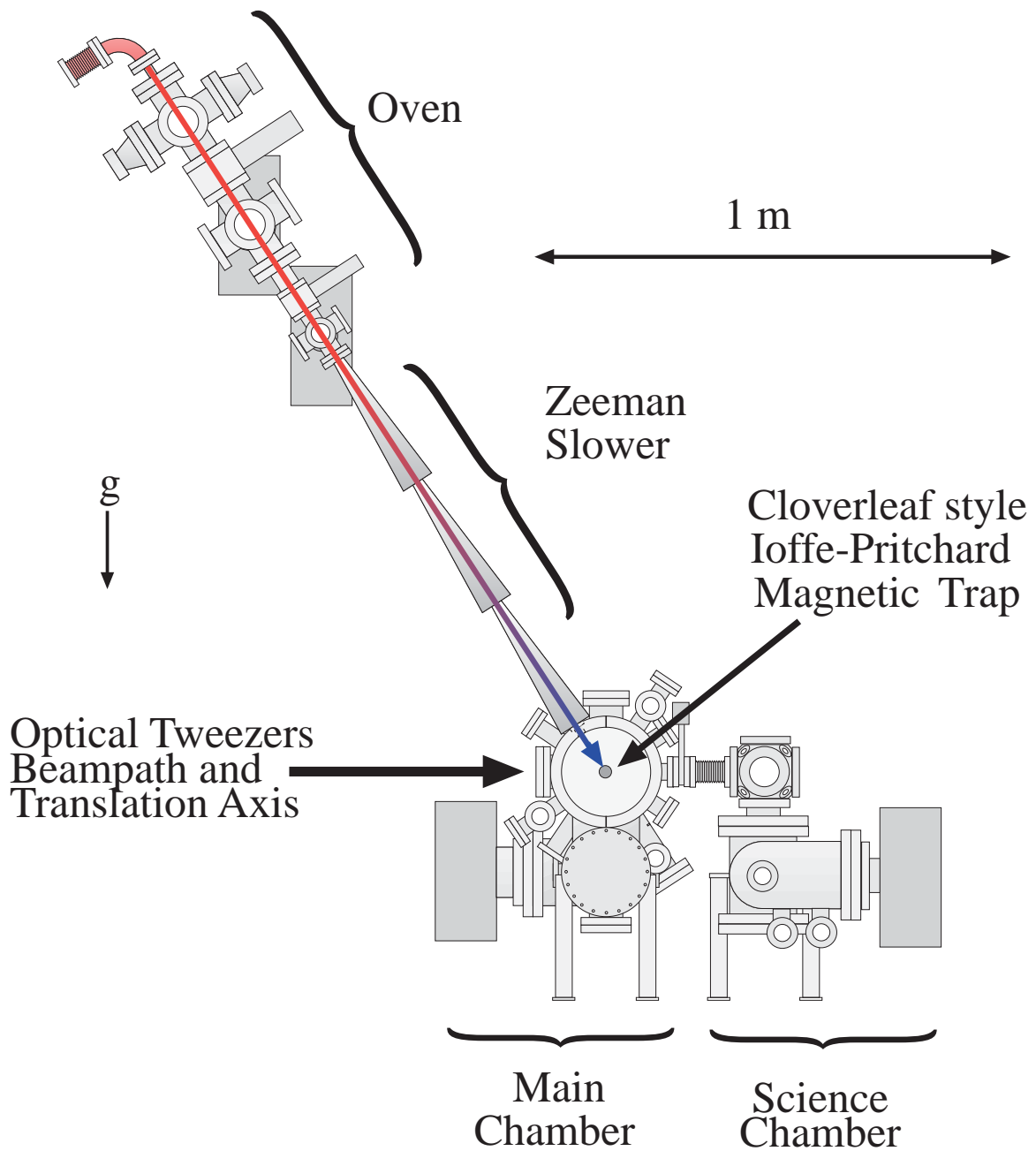


Figure 3-1: Vacuum system diagram and major subsystems.

of both the optical tweezers and magnetic trap. Vibrational heating during transport cited in [35] was reduced by the use of Aerotech ABL2000 series air bearing translation stages. Technical problems related to the greater mass and higher three body recombination rate in ^{87}Rb were overcome by transporting ultracold atoms just above the transition temperature

T_c , and then evaporating to BEC at the destination. The greater mass results in greater inertia and hence the need for a steeper optical potential to translate the atoms. The restricted optical access (Fig. 3-2) limited our ability to make a steep optical potential with a tight focus. This meant we needed to use higher powers to create the optical gradient necessary to transport the ^{87}Rb atoms. Ch. 3.9 discusses investigations where the deep trap depths, regardless whether they were optical or magnetic, were found to be unsuitable for holding dense ^{87}Rb Bose-Einstein condensates.

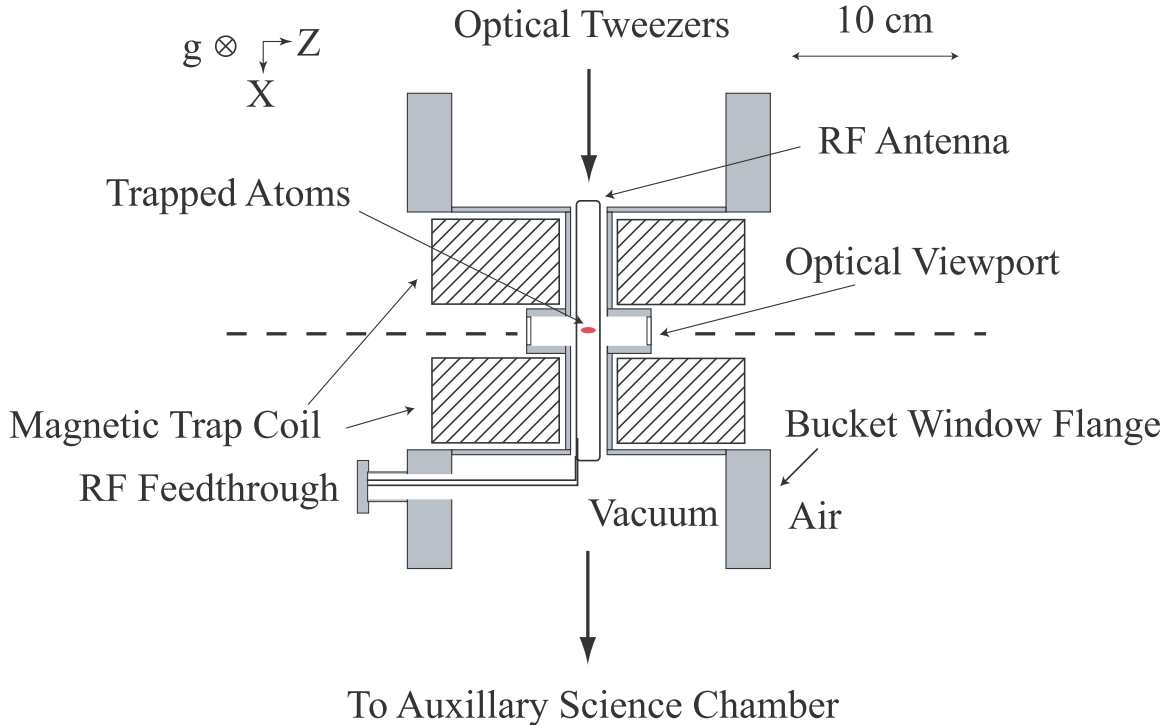


Figure 3-2: Main chamber vacuum system cross section showing re-entrant bucket windows, magnetic trap coils, and RF antenna. View from above.

The cloverleaf-style Ioffe-Pritchard magnetic trap coils fit inside two re-entrant bucket windows ¹, allowing them to be outside the chamber with an inter coil spacing of 25 mm (Fig. 3-2). The Zeeman slower tube is mounted between the main chamber and the oven chamber. The Zeeman slower coils surrounding the Zeeman slower tube are also outside of the vacuum system, but cannot be removed without breaking vacuum.

After assembling the chamber, we pumped out the system and reached UHV conditions by heating the system to accelerate outgassing. We heated the main chamber to 230°C and the Zeeman slower to 170°C (limited by the coil epoxy). Using a residual gas analyzer to

¹Simon Hanks of UKAEA, D4/05 Culham Science Center, Abingdon, UK

monitor the main chamber, we baked the chamber until the partial pressure of hydrogen was reduced to less than 10^{-7} torr and was at least ten times greater than the partial pressure of other gases. A typical bakeout lasted between 3 and 9 days, with temperature changes limited to less than $25^{\circ}\text{C}/\text{hour}$. Typical pressures immediately after the bakeout were in the low 10^{-11} to mid 10^{-12} torr. To reduce the pressure further we deposited a titanium film inside the lower part of the main chamber by passing current through a filament type titanium sublimation (Ti:sub) pump. During the bakeout we repeatedly ran a smaller amount of current through each of the filaments (degassing) to boil off trapped gases within them. The vacuum in the main chamber is preserved after bakeout with a 75 L/s ion pump and the titanium film. We used a new ion pump and took caution to only run the pump once the pressure was below 10^{-9} torr. This enhances the pumping speed because the pump has not yet been saturated. With the gas loads found in our main chamber we expect the pump to run at constant pumping speed for years to decades before saturating. While we acknowledge the merit of using dry pumps as recommended in Ref. [34], we use oil sealed rotary vane roughing pumps with long foreline tubes to back our turbo pumps. Our procedure is to immediately turn on the turbo pump once the roughing pump is turned on. This may reduce the backstreaming of oil vapor into the main chamber. In a similar manner, when we bring the chamber up to atmosphere we close off the roughing line at the turbopump and allow the unpowered turbopump to spin down. When the turbopump has spun down to a few thousands revolutions per second we introduce a dry venting gas (typically nitrogen or argon). Spinning down takes around 30 minutes if the bearings are in good condition. Please refer to Sec. 3.4 of Ref. [49] for more details of our bakeout procedures.

3.2 High Flux Rb Oven

3.2.1 Effusive Ovens

We generate a large flux of thermal ^{87}Rb atoms for Zeeman slowing from an effusive atomic beam oven (Fig. 3-3). An effusive beam is created by atoms escaping through a small hole in a heated chamber [50]. The vapor pressure of rubidium is very different from that of sodium, requiring a different design than that used in previous sodium machines. At room temperature, the vapor pressure of sodium ($\approx 3 \times 10^{-11}$ torr [51]) is compatible with our UHV main chamber environment, while that of rubidium ($\approx 4 \times 10^{-7}$ torr [52]) is not. This dictated that the design of the rubidium oven not risk the contamination of the main chamber with rubidium. A positive side of the lower vapor pressure of rubidium is the lower operating temperatures we can use to obtain similar fluxes (110-150°C Rb, 260-350°C Na.) We expect that the rubidium oven design would also work for sodium [49]. Another difference is that only 28% of the atoms are of the desired ^{87}Rb isotope, with the balance being ^{85}Rb . Naturally occurring sodium has only one isotope, ^{23}Na . Isotopically enhanced

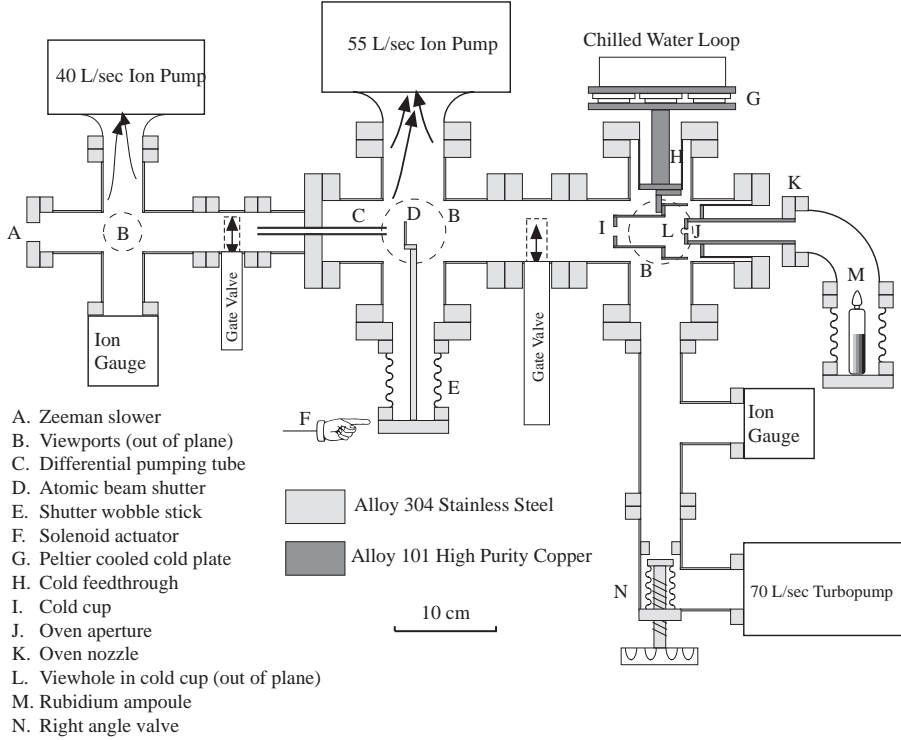


Figure 3-3: Effusive rubidium beam oven. Rubidium metal (M) is heated to between 110°C and 150°C , creating a $p_{\text{Rb}} \sim 0.5$ millitorr vapor which escapes through a 5 mm diameter hole (J). A 7.1mm diameter hole in the cold cup (I), 70 mm from the nozzle, allows 0.3% of the emitted flux to pass through, forming an atomic beam with a flux of $\sim 10^{11}$ atoms/s. The remainder is mostly (99.3%) captured on the -30°C , $p_{\text{Rb}} \approx 2.5 \times 10^{-10}$ torr, surface of the Peltier cooled cold cup. We chop this beam with a paddle (D) mounted to a flexible bellows (E). The differential pumping tube (C) and Zeeman slower tube (A) consecutively provide 170x and 620x of pressure reduction between the oven and main chambers.

^{87}Rb salts are available, but were not considered due to the extreme additional cost and complexity they would entail.

To sustain a high flux atomic beam, the background vacuum pressure must be low enough that the mean free path between collisions is much greater than the length of the beam. To generate an effusive beam with a thermal distribution of velocities the size of the hole through which the atoms escape must be smaller than the mean free path $l = 1/n\sigma$ inside the oven, where n is the density of atoms per unit volume and σ is the atom atom scattering cross section. While at low temperatures the scattering is dominated by the lowest few partial waves, at higher temperatures such as those found in the oven the scattering behavior is classical and can be approximated as hard sphere scattering. The atomic radius 0.25 nm [53] was used to calculate the scattering cross section of $\sigma = 19.6 \times 10^{-16}\text{cm}^2$. For comparison, in the s-wave scattering regime below $\sim 200\mu\text{K}$, the scattering length is ~ 5.3 nm. While any atom-atom scattering event will reset the phase of a radiating atom, a small angle scattering will not significantly affect the direction of an atomic beam. Calculations

of the scattering cross section σ based on the long range attractive potential for hot atoms will overestimate the effective scattering cross section σ because of the inclusion of these long range, small angle scattering events.

A combination of active pumping and passive geometrical techniques were used to reduce extraneous rubidium transfer to the main chamber. A cold cup (I) is used to reduce rubidium vapor in the oven chamber by almost completely surrounding the oven aperture (J) with a cold surface at -25°C . After bakeout, the combination of cold cup and oven chamber ion pump has achieved pressures as low as $\sim 10^{-9}$ torr, although we have successfully made BECs with pressures of up to $\sim 10^{-6}$ torr in this region. The combination of a differential pumping tube, an ion pump, and the Zeeman slower tube provides a pressure differential of over 3 orders of magnitude between the oven and main chamber. This is sufficient to isolate the UHV environment from an oven pressure dominated by rubidium vapor at room temperature. When the oven is opened to replace rubidium and clean the cold cup, the main chamber vacuum is isolated with a pneumatic gate valve. A second gate valve can be used in case of failure of the first. While not used in our system, designers may want to consider gate valves with an embedded window available from VAT to allow optical access along the Zeeman slower or tweezer beam lines during servicing.

The cold plate is chilled to -30°C with six Ferrotec 6320/185/065/S two stage thermoelectric coolers (TECs) powered with 3A DC current. A 40 psi low pressure chilled water loop operating at 18°C removes the heat generated by the hot side of the TECs. To prevent ice from accumulating inside the TECs they were factory sealed with silicone. The entire cold plate/feed through assembly is encased in an airtight plastic box to prevent ice buildup on the chilled components. Typical mean time before failure at 3A for the Peltier coolers is ~ 3 years of continuous operation. At their maximum specified current of 6A we have observed that the lifetime of the TECs is shortened to less than half a year.

3.2.2 Operation

Rubidium is a highly reactive metal, responding vigorously to the presence of oxygen or water. Our oven design and procedures have been structured to minimize the hazards to operating personnel. As students and not employees we are not covered by workers compensation insurance for medical costs relating to industrial accidents. During operation, the machine is run as a sealed system, without the turbo-mechanical pump, to prevent accidental loss of the main chamber vacuum. Oven temperatures from 150°C down to 110°C produce similar sized ^{87}Rb BECs. Reducing the oven temperature increases the time between rubidium changes to greater than 1000 hrs of operating time. This long operating cycle precluded the need for more complex recycling oven designs [54]. Informal discussions with groups that have built candlestick ovens revealed that the flux of atoms below the mean velocity is often reduced from that expected from the Boltzman distribution, making the flux of low velocity atoms available with a Zeeman slower dependent on the actual rather

then ideal velocity distribution.

To prevent accumulation of metal at the aperture (Fig. 3-3, Part J), the oven nozzle temperature (Fig. 3-3, Part K) is kept higher ($\sim 10^\circ\text{C}$ in rubidium and $\sim 90^\circ\text{C}$ in sodium) than the rest of the oven. The velocity distribution of the beam is determined by the nozzle temperature (Fig. 3-3, Part K). On the other hand, the vapor pressure in the oven, which controls the beam flux, is dominated by the coldest spot in the elbow and bellows. The factor of two discrepancy between the observed and calculated (Table 3.1) rubidium oven lifetimes at 110°C can be accounted for by a spot $\sim 10^\circ\text{C}$ colder than the lowest measured oven temperature. The specifics of this cold spot depend on how the oven is insulated. We typically insulate with a layer of loose fiberglass insulation covered with aluminum foil. Three type K thermocouples are attached at the nozzle, elbow and bellows to monitor the temperatures. The oven is heated with one tape heater wrapped around the nozzle's copper shank and three band heaters attached to the elbow and bellows junctions. Each heater is independently controlled with a Variac variable voltage transformer. The Variacs are adjusted so that in equilibrium the oven runs $15\text{-}20^\circ\text{C}$ hotter than desired. Power to the Variacs is then controlled by an Omega Engineering CN16D24-C24, Intelligent Temperature Controller wired to one of the thermocouples. This allows us to finely adjust the temperature of the oven, and do so reproducibly so long as the wrapping insulation is not modified. An isolated serial port connected to the temperature controller allows remote monitoring, shutdown, and startup of the oven. The typical warm up time is 40 minutes.

Servicing

Servicing the oven consists of two operations: removing the rubidium which has been deposited on the cold cup and replacing the ampoule. During servicing, a clean ampoule is essential for rapid recovery of good vacuum pressure. The ampoule is cleaned by submerging it in a 50/50 mixture by volume of acetone and isopropanol for 20 minutes, then air drying it. This removes most of the water from the glass surface, which would otherwise require more time to pump away. In the rubidium experiment the cleaned ampoule is placed in the oven while still sealed and baked for 24 hours under vacuum at $150\text{-}180^\circ\text{C}$ to remove the remaining contaminants before it is broken.

Solid rubidium melts at 39.3° , slightly above room temperature. When Rb metal is exposed to air, the various reactions will often generate enough heat to melt the metal, creating a potentially hazardous situation of reactive liquid metal pouring down unexpected places. For safety reasons we use only a small amount of Rubidium metal in our atomic beam oven. Ampoules of 5 gm, packed under an inert Argon atmosphere are used to charge the oven. Typically we allow a maximum of 10-15 gm of Rb to be deposited on the cold cup before servicing. The procedure we have found is most effective for neutralizing these quantities of Rb is to slowly quench it with water in an inert atmosphere. A deep sink filled with dry ice works well. To service the Rb oven we first flood the chamber with dry Ar or

N_2 gas. We then remove the nozzle flange and unscrew the cold cup. Using a pair of pliers we extract the cold cup and put it in a metal bucket and then cover the top with aluminum foil. Adding dry ice to the bottom helps drive out the oxygen and water vapor which could react with the Rb metal deposited on the cold cup. The metal bucket is then taken to the deep sink filled with dry ice. Water is added drop by drop to react with the Rb metal. When a drop of water hits rubidium metal the results are fizzing, producing hydrogen gas, and occasionally small red flames. This is why it is essential to neutralize the Rb metal with only a drop of water at a time. Once all the Rb metal has been reacted the cold cup can then be flushed with water to dissolve any remaining Rubidium salts.

3.2.3 Design table

To design the rubidium oven a spread sheet (Table 3.1) was developed to allow different parameter configurations to be tested without constructing prototypes. The one adjustable parameter in the Rubidium oven is the temperature, which sets the vapor pressure and the velocity distribution emerging from the oven. In a three dimensional gas the ideal Boltzman distribution of velocities is

$$f(v) = \sqrt{\frac{2}{\pi}} \frac{v_z^2}{\tilde{v}^3} \exp\left(-\frac{v^2}{2\tilde{v}^2}\right) \quad (3.1)$$

where the characteristic velocity $\tilde{v} = \sqrt{k_B T/m}$ is a function of the temperature and particle mass [55]. Sampling this velocity distribution by poking a small hole in a chamber of gas in thermal equilibrium gives an atomic beam with a velocity distribution

$$f(v_z) = \frac{v_z^3}{2\tilde{v}^4} \exp\left(-\frac{v_z^2}{2\tilde{v}^2}\right) \quad (3.2)$$

If the free path of an atom is smaller than the hole size, the hole is no longer small in terms of that atom and we can no longer consider the oven to be sampling the Boltzman distribution. A collisionally dense gas cloud forms in front of the nozzle, causing a condition referred to as stalling. Smaller holes will stall at high temperatures/pressures, but produce smaller fluxes. We chose to use a large hole diameter of 5mm to prevent clogging and provide a more generous tolerance for misalignment of the Zeeman slowing laser beam.

3.3 Zeeman Slower

The atomic beam is slowed from thermal velocities by nearly an order of magnitude by scattering photons from a resonant, counter-propagating laser beam. When a photon with momentum $\hbar k$ ($k = 2\pi/\lambda$) is absorbed or emitted by an atom with mass m , the atom conserves momentum by recoiling with a velocity change of $v_r = \hbar k/m$. Atoms can resonantly scatter photons up to a maximum rate of $\Gamma/2$, where $1/\Gamma = \tau$ is the excited-

Temp (°C)	Velocity ¹ (m/s)	Pressure [52] (torr)	Density #/cm ³	Free Path (m)	Flux Density #/cm ² /sec	Total Flux ² #/sec	Lifetime ³ (hrs)
-40	261	4.60E-11	1.90E+06		1.30E+10	2.60E+09	
-30	266	2.50E-10	1.00E+07		7.30E+10	1.40E+10	
-20	272	1.20E-09	4.70E+07		3.40E+11	6.80E+10	
-10	277	5.30E-09	1.90E+08		1.40E+12	2.80E+11	
0	282	2.00E-08	7.20E+08		5.50E+12	1.10E+12	
10	287	7.10E-08	2.40E+09		1.90E+13	3.70E+12	
20	292	2.30E-07	7.50E+09		6.00E+13	1.20E+13	
25	295	4.00E-07	1.30E+10		1.00E+14	2.00E+13	
30	297	6.80E-07	2.20E+10		1.80E+14	3.40E+13	
40	302	2.00E-06	6.00E+10		5.00E+14	9.70E+13	
50	307	4.90E-06	1.50E+11	8700	1.20E+15	2.40E+14	
60	312	1.20E-05	3.40E+11	3800	2.90E+15	5.60E+14	
70	316	2.60E-05	7.40E+11	1700	6.30E+15	1.20E+15	
80	321	5.70E-05	1.50E+12	820	1.30E+16	2.60E+15	3696
90	325	1.20E-04	3.10E+12	410	2.70E+16	5.40E+15	1815
100	330	2.30E-04	6.00E+12	210	5.40E+16	1.10E+16	926
110	334	4.50E-04	1.10E+13	110	1.00E+17	2.00E+16	489
120	339	8.30E-04	2.00E+13	63	1.90E+17	3.70E+16	267
130	343	1.50E-03	3.60E+13	36	3.30E+17	6.50E+16	151
140	347	2.60E-03	6.10E+13	21	5.70E+17	1.10E+17	87
150	351	4.40E-03	1.00E+14	13	9.60E+17	1.90E+17	52
160	355	7.30E-03	1.60E+14	7.8	1.60E+18	3.10E+17	32
170	360	1.20E-02	2.60E+14	4.9	2.50E+18	5.00E+17	20
180	364	1.90E-02	4.00E+14	3.2	4.00E+18	7.80E+17	13

Table 3.1: Oven Design Parameters

state lifetime. This results in a maximum spontaneous emission acceleration $a_{max} = \frac{\hbar k \Gamma}{2m}$ ($1.1 \times 10^5 \text{m/s}^2$). As the atoms decelerate, the reduced Doppler shift is compensated by tuning the Zeeman shift with a magnetic field [6] to keep the optical transition on resonance. We designed the slower to decelerate the atoms at a reduced rate $f a_{max}$ where $f \sim 50\%$ is a safety factor to allow for magnetic field imperfections and finite laser intensity.

Our slower is designed along the lines of Ref. [56], with an increasing magnetic field and σ^- polarized light scattering off the $F=2, m_F=-2 \rightarrow F'=3, m_{F'}=-3$ cycling transition. Before the slowing begins, the atoms are optically pumped into the $F=2, m_F=-2$ state. The large magnetic field at the end of the slower corresponds to a large detuning from the low velocity, low magnetic field resonance frequency. This large detuning allows the slowing light to pass through the MOT without distorting it due to radiation pressure. Within the slower coils, the quantization axis is well-defined by the longitudinal magnetic field and optical pumping out of the cycling transition is strongly suppressed by the combination of light polarization and Zeeman splitting.

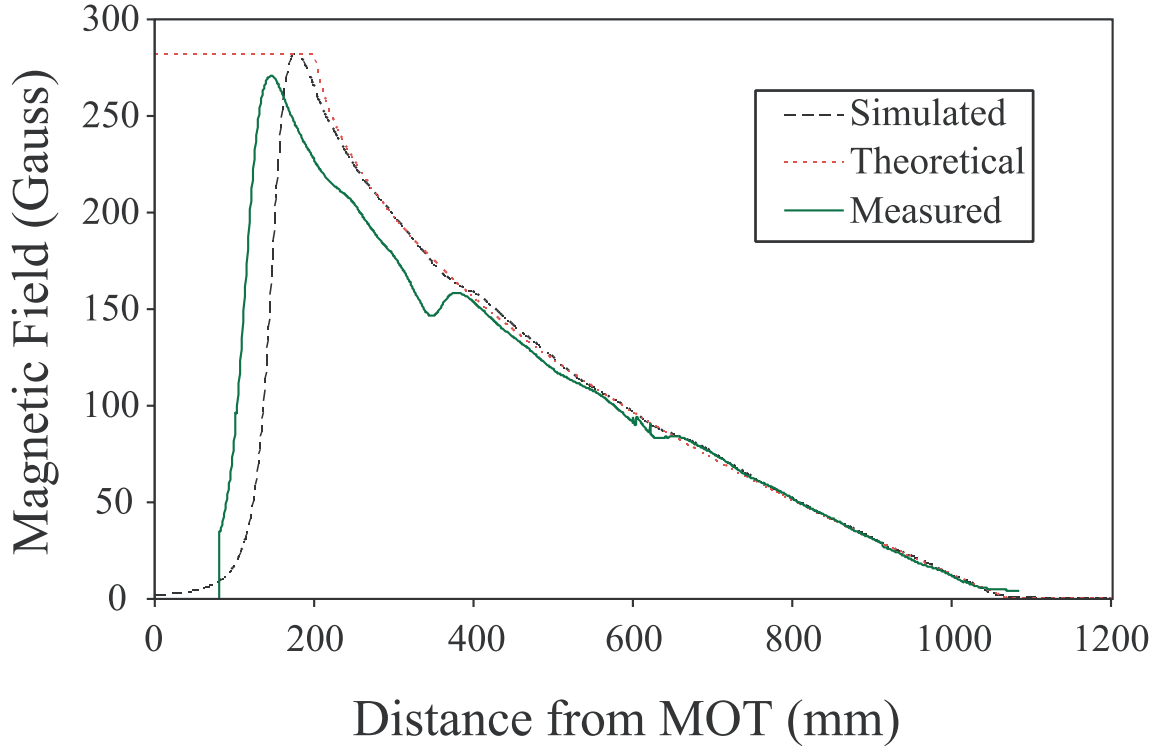


Figure 3-4: Magnetic field profile of the rubidium Zeeman slower, not including uniform bias field. The theoretical line shows the desired magnetic field profile for atoms decelerated from 330 m/s to 20 m/s at 60% of the maximum intensity limited deceleration ($f=53\%$ of a_{max} .) The simulated line depicts the expected field from slower coils with the winding pattern in Fig. 3-5 of Appendix 3.3. The prominent bumps shown above in the measured field were subsequently smoothed with additional current carrying loops.

We slow ^{87}Rb atoms from an initial velocity of ~ 350 m/s with a tailored 271 G change in the magnetic field (Fig. 3-4). An additional uniform ~ 200 G bias field was applied along the length of the slower to ensure that neighboring hyperfine levels were not near resonance in either the slower or the MOT. The slower cycling transition light is detuned -687 MHz from the $F=2 \rightarrow F'=3$ transition. The slowing laser intensity is $I/I_{sat} \approx 8$, giving a maximum theoretical deceleration of 89% of a_{max} . To maximize the number of atoms in the slowed $F=2, m_F=-2$ state “Slower repumping” light copropagates with the cycling transition light and is detuned -420 MHz from the $F=1 \rightarrow F'=1$ transition to match the Doppler shift of the unslowed thermal atoms from the oven. A flux of $\sim 10^{11}$ ^{87}Rb atoms/s with a peak velocity of 43 m/s was measured from our slower with an oven temperature of 150°C. This is significantly greater flux than the 8×10^8 Rb/sec vapor cell loading rate quoted by [34]. Recently a higher flux (3.2×10^{12} Rb/s) design was demonstrated [57]. This approach used

several additional techniques to increase the flux, including an optical molasses collimating stage.

Every photon which scatters off an atom to slow the atom in the Zeeman slower is radiated in a random direction, increasing the atoms' spread in transverse velocity. The beam emerging from the tube needs to have sufficient forward mean velocity to load the MOT efficiently. Because of the random direction of the emission recoil, N photon scatterings increase the transverse velocity by $v_r\sqrt{N/3}$. The initial and recoil velocities in the ^{87}Rb slower increase the transverse velocity by $\approx 0.8\text{m/s}$, resulting in a collimated slowed beam whose transverse width is smaller than the size of the MOT beams. From this we estimate that most of the slowed atoms are captured in the MOT.

An additional concern is the fate of the rubidium atoms after the experiment. Whether they are captured by the MOT or not, almost all of the atoms in the atomic beam are deposited into the main chamber. If these atoms are not pumped away the ultrahigh vacuum will be compromised. As an insurance measure an additional cold plate was installed near the slower window on the main chamber to capture desorbed Rb. Vacuum pressure has not been an issue and we have never needed to chill this cold plate to preserve the main chamber environment.

3.3.1 Slower Construction

The vacuum portion of the ^{87}Rb slower is a 99 cm long nonmagnetic 304 stainless steel tube with a 19 mm OD and 0.9 mm wall. The rear end of the tube is connected to the main chamber by a DN 16 CF rotatable flange, while the oven end of the tube has a narrow, 50mm long flexible welded bellows ending in another DN 16 CF rotatable flange. The retaining ring on this flange was cut in half for removal, so that the premounted coil assembly could be slid over the vacuum tube.

As shown in Fig. 3-1 the slower tube enters the main chamber at an angle of 33° from the vertical to accommodate access for optical tweezers. The oven and the Zeeman slower are supported two meters above the experimental table in order to preserve the best optical and mechanical access to the main chamber. Aluminum extrusion from 80/20 Inc. was used to create the support framework.

Our ^{87}Rb slower was fabricated with a single layer bias solenoid and three increasing field coils (Fig. 3-1 and 3-5), segmented for better cooling. The optimum configuration of currents and solenoid winding shapes was found by computer simulated winding of the solenoids one loop at a time, starting at the high field end and tapering the last few loops to best match the desired field profile. An alternative fabrication technique would be to apply a large uniform bias field and subtract away unwanted field with counter current coils. This technique can smooth out the bumps in the magnetic field shown in Fig. 3-4. Residual field from the Zeeman slower can have a detrimental effect on the MOT, shifting its location suddenly during turnoff. A coil canceling out the residual bias field of the slower at the

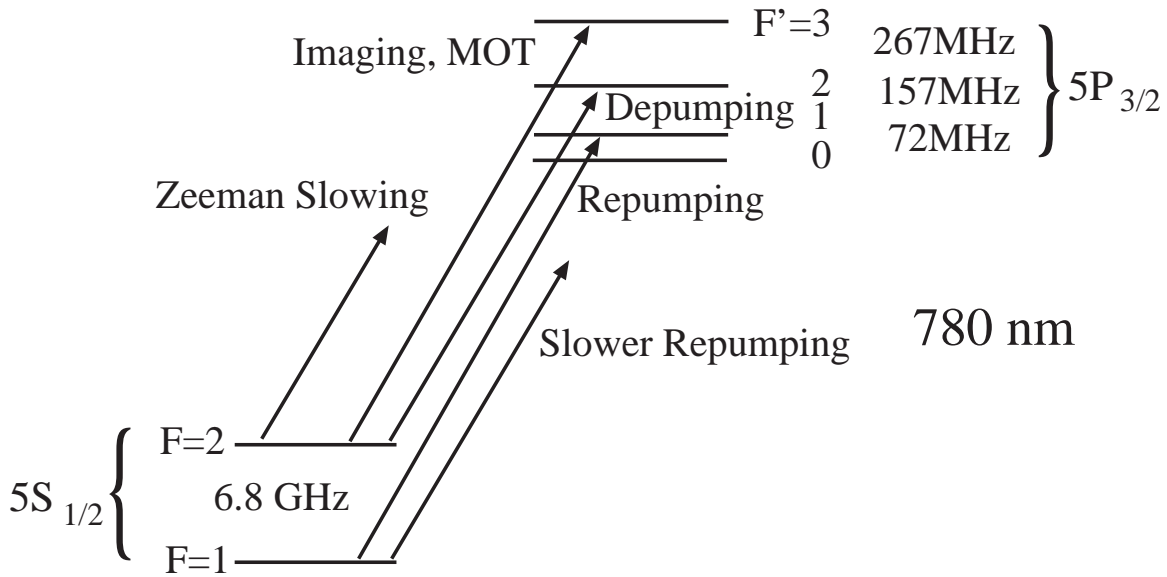


Figure 3-6: Simplified energy level structure of ^{87}Rb with relevant transitions, hyperfine splittings, and laser frequencies.

tive saturated absorption spectroscopy lock [58, 59]. This modulation-free technique optically creates a derivative signal of the absorption spectra that is locked with a proportional+integral gain servo loop. The locking signal fluctuation indicates a frequency jitter of $< 1\text{MHz}$ over several seconds, which is much less than the 6.1 MHz natural linewidth of ^{87}Rb . The large frequency shifts used for the slower cycling and repumping light reduced the available power to a few mW. Each of these beams is amplified to 35-40 mW by injection locking [60] a free running Sanyo DL7140-201 laser diode before combining the beams on a non polarizing beamsplitter and coupling into a fiber.

The ^{87}Rb MOT uses a total of 60 mW of light near the $F=2 \rightarrow F'=3$ cycling transition for trapping/cooling. The $F=2 \rightarrow F'=3$ transition in the MOT is only approximately a closed cycle and atoms are often optically pumped into the $F=1$ ground state. To repump these atoms back into the $F=2$ state we use 10 mW of light on the $F=1 \rightarrow F'=1$ transition. In addition, to transfer atoms from the $F=2$ to $F=1$ manifold, e.g. prior to loading them into the magnetic trap, we introduce a few mW of “depumping” light resonant with the $F=2 \rightarrow F'=2$ transition. Zeeman slowing uses 18 mW of slower cycling light and 6 mW of slower repumping light. All powers are quoted after fiber coupling, measured as delivered to the apparatus table. Recent advances in single frequency high power fiber and diode pumped solid state lasers, such as IPG Photonics EAD and RLM series amplifiers, have made nonlinear techniques such as sum frequency generation [61, 62] and frequency doubling [63] interesting alternatives as resonant light sources.

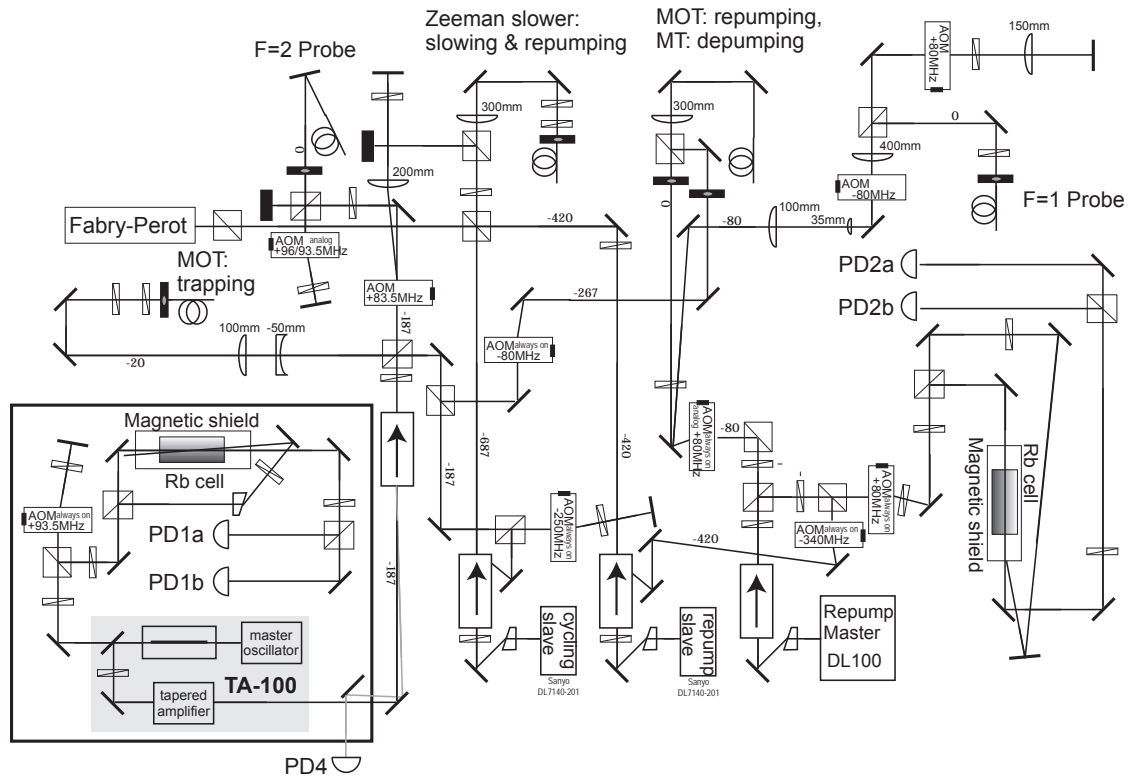


Figure 3-7: Layout of the laser optical table. Numbers indicate frequency offsets in MHz. All detectors are Thorlabs Model DET110. ECLDs are Toptica DL100. Slave lasers are Sanyo DL7140-201S laser diodes. The Fabry Perot is a 1.5 GHz Free Spectral Range Toptica FPI-100. Optical isolators (boxes with arrows) are Optics For Research IO-5-780-HP. AOMs are from Isomet and InterAction.

3.4.1 Fiber Coupling

Most of the fibers in our system distributing 780 nm light are model Thorlabs P3-4224-FC-5 FC APC angle polished fiber patch cables with FC type connectors. When coupling with a CM230TM-B aspheric collimating lens typical coupling efficiencies range from 50-80%, depending on the input beam quality. These fibers are not polarization preserving. Stress birefringence causes these fibers to act as a series of random thickness waveplates. We found that once put in place the fibers polarization rotation effects were constant unless unless moved. With the addition of $\lambda/2$ and $\lambda/4$ waveplates before the coupler, and a polarizing beam splitting cubes to cleanup the polarization on the table we developed a working solution without the need for multiple expensive polarization preserving fibers. There is one polarization preserving fiber for 780 nm light in the system. The F=1 probe beam is coupled into an OZ Optics PMJ-3A3A-780-5/125-3-4-1 polarization preserving PANDA fiber patch cable. To prevent light which leaks through the AOMs from entering the fibers we used Varian Associates Uniblitz Model LS6ZM2 mechanical shutters. We measured

opening delay times of 3-6 ms, depending on the quality and age of the drive electronics.

3.4.2 Injection Locking

To increase the power of the slower and slower repumper light from a few mW to tens of mW we use an injection locking technique to convert a free running laser diode into a slaved amplifier. In most cases we use an optical isolator to prevent back reflections or other stray laser beams from being coupling into the laser diode. This backcoupled light can cause the laser diode to become unstable or act unpredictably. In the case of injection locking we are purposely introducing this light to override the free running behavior of the laser oscillator.

The freerunning lasers in our case are Sanyo DL7140-201S laser diodes mounted in a Thorlabs TCLDM-9 TE cooled laser diode mount and driven with a Thorlabs TEC2000 Temperature controller and LDC500 current controller. The injection light is coupled in through the rejection port of an optical isolator (Optics for Research IO-780-HP4). We have had the best results when the Sanyo diodes were first temperature tuned so that when free running they are near resonance with the Doppler broadened Rb absorption line (~ 8 GHz wide). The spectrum of the slave diode is monitored on a Fabry Perot spectrometer (Toptica FPI-100). When the alignment is correct and the laser diode becomes locked, the laser line becomes much narrower, and will scan back and forth if the injection signal is scanned. Better alignment allows this locking behavior to occur with less power. A full discussion of injection locking can be found in [60].

3.5 Computer Control and Imaging

Two computers run the apparatus; one controls the various parts of experiment and the other processes images from a camera which images the atoms. The control computer has custom built National Instruments (NI) LabWindows based software to drive analog (2 NI Model PCI 6713, 8 channels of 12 bit analog, 1MS/s update) and digital (2 NI Model PCI-6533, 32 channels of binary TTL, 13.3 MS/s update) output boards. The control computer also controls an Agilent 33250A 80MHz function generator through a GPIB interface, and triggers a Princeton Instruments NTE/CCD-1024-EB camera through a ST-133 controller to capture the absorption images.

All of our measurements are performed by taking an image of the the atoms. At the end of an experiment the trap is quickly turned off at the atoms are allowed to freely expand as they fall under the influence of gravity. The expansion during the time of flight (TOF) between trap turnoff and imaging greatly expands the imaged size of the condensate in the tightly confining axes. The expansion of thermal atoms is driven by their kinetic energy. In the Thomas Fermi limit condensates have no kinetic energy. Their free flight dynamics are instead driven by the density dependent mean field energy.

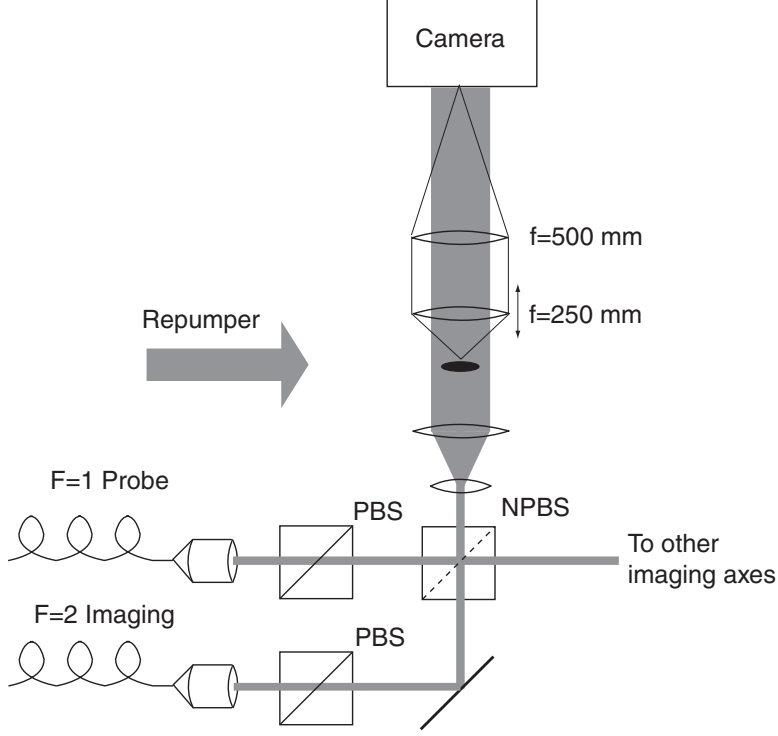


Figure 3-8: Layout of vertical imaging axis in main chamber. F=1 probe light or F=2 Imaging light can illuminate the condensate with a 4 mm beam. Each beam passes through a polarizing beamsplitter (PBS) to give it a definite linear polarization. The two beams, with orthogonal linear polarizations, are overlapped on a nonpolarizing beamsplitting cube (NPBS) for convenience in delivery and later separation in other imaging system. The 50 mm diameter, $f=250$ objective lens is mounted on a vertical translation stage to adjust the focus for different time of flights. Repumping light is introduced off axis.

3.5.1 Free Expansion

The cold atoms are released from the trap and allowed to expand to increase their size prior to imaging. Bose-Einstein condensates expand because their mean field repulsion is no longer balanced by the harmonic trapping potential and therefore converts to kinetic energy in time $\sim 1/\omega_x$. In a similar manner without the trapping potential the kinetic energy of thermal atoms cause them to expand ballistically. Both of these effects are most prominent in the tightly confining direction, increasing the apparent size between 10 and 100 times for typical trap frequencies and times of flight.

$$n_C^{2D}(x, z, t) = n_p^{2D} \left(1 - \frac{x^2}{r_x^2(t)} - \frac{z^2}{r_z^2(t)} \right)^{3/2} \quad (3.3)$$

Conversion of the mean field repulsion into kinetic energy results in a scaling but not distortion of the signature parabolic shape [64]. For cigar shaped cylindrically symmetric traps with aspect ratio $\epsilon = \omega_z/\omega_x \ll 1$ the free expansion can be approximated as

$$r_x(\tau) = r_x(0)\sqrt{1 + \tau^2} \quad (3.4)$$

$$r_z(\tau) = r_z(0) \left(1 + \epsilon^2 \left[\tau \arctan \tau - \ln \sqrt{1 + \tau^2} \right] \right) \quad (3.5)$$

where $\tau = \omega_x t$ is in units of the radial trap frequency normalized time. Typical aspect ratios in magnetic traps are $\epsilon = 0.05 - 0.1$. In typical optical traps $\epsilon < 0.02$.

The non condensed thermal cloud has a two dimensional projection of the Gaussian density distribution

$$n_{NC}^{2D}(x, z, t) = n_p^{2D} \exp \left(-\frac{x^2}{2\sigma_x^2(t)} - \frac{z^2}{2\sigma_z^2(t)} \right) \quad (3.6)$$

where $\sigma_i^2 = k_B T / m (1/\omega_i^2 + t^2)$ and n_p^{2D} is the peak density of the image.

In the long time limit the thermal cloud takes on a circular shape as velocity rather than original location dominates the density distribution. The mean field interaction in the BEC inverts its aspect ratio from $1/\epsilon$ to $\epsilon\pi/2$. This combined with the sharp increase in density provide an extremely clear signature of the condensation phase transition.

3.5.2 State Analysis

During free fall a magnetic field gradient can be applied to perform Stern-Gerlach state separation to resolve different Zeeman levels. Atoms in the F=1 or F=2 states can be selectively imaged using light resonant with either the F=1 probe or F=2 imaging light. The F=2 to 3 transition is a cycling transition and in our experience provides the best imaging. F=1, F=0 imaging provides a similar cycling transition for the F=1 level. More complicated simultaneous state analysis techniques have been developed and are discussed in Ch. 4.

3.5.3 Repumping effects

The optical pumping of the atoms from the F=1 to F=2 hyperfine level will induce a recoil in the atoms. This can potentially introduce unwanted distortions in imaging F=1 atoms. If the repumping occurs immediately before imaging the recoil velocity kick will not affect the atoms' location and there will be no deformation to the density distribution. On the other hand, if repumping occurs too long before imaging the atoms will move and smear out the density distribution. This increases the apparent size of the condensate and also creates the appearance of thermal atoms when none are present. For a 6 μm pixel size and $v_r=6$ mm/s it will take an atom 1 ms to move one pixel. We typically repump for 50-200 μs immediately before imaging, so at this magnification recoil blurring should not be a problem. The repump light must be modulated with an AOM to achieve this level of

timing accuracy. Mechanical shutters have an opening time of several ms and are less than favorable for precision work.

3.5.4 Camera

To image the atoms three pictures are taken with a Princeton Instruments NTE/CCD-1024-EB camera controlled by a ST-133 controller: a picture of the illuminated atoms, a picture of the illumination without the atoms, and a background picture without illumination. An absorption image is calculated by taking the ratio of the illuminated images after the background image is subtracted from each illuminated image.

In several experiments and alignment techniques it is necessary to shine non imaging laser light along an imaging axis. If the light is of high power, such as an optical tweezers beam, it could damage the camera. Lower power light, such as used in the quantum Zeno effect experiments in Ch. 4, while not destructive can still saturate the CCD detector, ruining the image. To protect the camera from such non imaging light a 1" diameter mechanical shutter, Vincent Associates Uniblitz Model VS25S-2-ZM-0 driven with a Model VMM-D4 four channel driver, was added.

3.6 Magneto Optical Trap

The MOT [9] is the workhorse of atomic physics for creating large samples of ultracold atoms. We use a six-beam configuration, which doubles as an optical molasses when the magnetic gradient field is off. Similar to Ref. [34] the ^{87}Rb apparatus uses a bright MOT instead of a dark-spot MOT [65]. The ^{87}Rb MOT equilibrates to around 4×10^{10} atoms after ~ 2 s of loading, operating in a magnetic field gradient of 16.5 G/cm with cycling beams detuned -18 MHz from the $F=2 \rightarrow F'=3$ transition and a peak intensity 5.3 mW/cm². To increase the efficiency of the transfer into the magnetic trap, we briefly compress the ^{87}Rb MOT and then switch off the magnetic field gradient to cool the atoms with optical molasses. The ^{87}Rb MOT is compressed by linearly ramping the gradient to 71 G/cm in 200 ms and simultaneously sweeping the detuning to -45 MHz in 400 ms. We use 5ms of "gray" molasses, where the repumper power is dropped by 95%, the optical trapping power is ramped down to 50%, and the detuning is swept from -18MHz to -26MHz. The molasses phase requires the cancellation of imbalances in intensity between beams and also of residual magnetic fields [66]. After the molasses phase, 0.5-1 ms of "depumping" light is applied to put all the ^{87}Rb atoms into the $F=1$ level before loading into the magnetic trap. Exact MOT and molasses parameters were found through empirical optimization, and all listed numbers should be considered as rough guides.

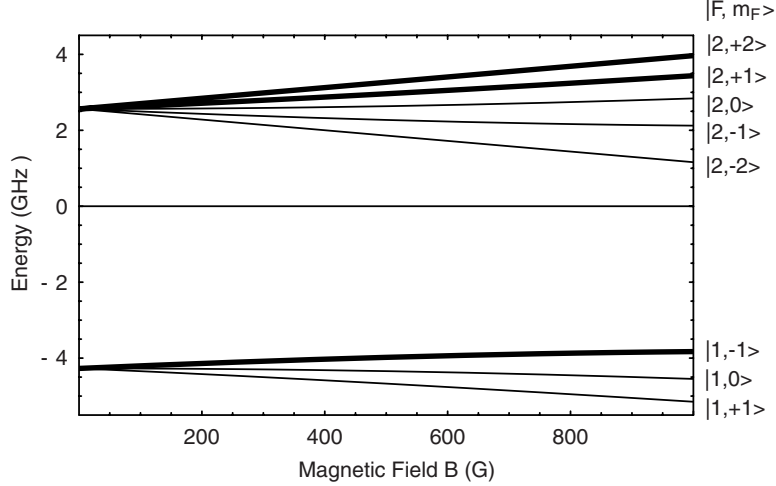


Figure 3-9: Zeeman energy diagram of the ^{87}Rb ground state hyperfine structure dependence on magnetic field. Heavy lines indicate the magnetically trappable weak field seeking states.

3.7 Magnetic Trapping

We trap ^{87}Rb atoms in the weak magnetic field seeking hyperfine ground states near the minimum of an inhomogeneous magnetic field produced by a cloverleaf style Ioffe-Pritchard trap [67]. Fig. 3-9 shows the energy dependence of the different hyperfine states with magnetic field strength. Three of the eight hyperfine ground states ($|2,+2\rangle, |2,+1\rangle, |1,-1\rangle$) are weak field seeking and have a potential energy dependence linearly proportional to the magnetic field strength. In order to trap atoms, the attraction to the magnetic field minimum must be sufficiently strong to overcome the force of gravity. Fortunately the single unpaired electron in ^{87}Rb gives these states magnetic moments of $\approx \mu_B$, $\approx \mu_B/2$, and $\approx \mu_B/2$ and allows the moderate magnetic field gradients of 15 G/cm, 30 G/cm, and 30 G/cm to exert a force on an atom equal to that of gravity. Magnetic field gradients stronger than this will successfully trap atoms. The $|2,0\rangle$ state, while also weak field seeking, is magnetic field insensitive at low field because of its quadratic, rather than linear dependence on magnetic field strength. This functional difference would make it very difficult to trap magnetically due to the very large magnetic field gradients necessary to overcome the pull of gravity.

3.7.1 Fields in a Ioffe-Pritchard Magnetic Trap

The field near the center of a Ioffe-Pritchard trap can be expressed as

$$\mathbf{B} = B_0 \begin{pmatrix} 0 \\ 0 \\ 1 \end{pmatrix} + B' \begin{pmatrix} x \\ -y \\ 0 \end{pmatrix} + \frac{B''}{2} \begin{pmatrix} -xz \\ -yz \\ z^2 - \frac{1}{2}(x^2 + y^2) \end{pmatrix} \quad (3.7)$$

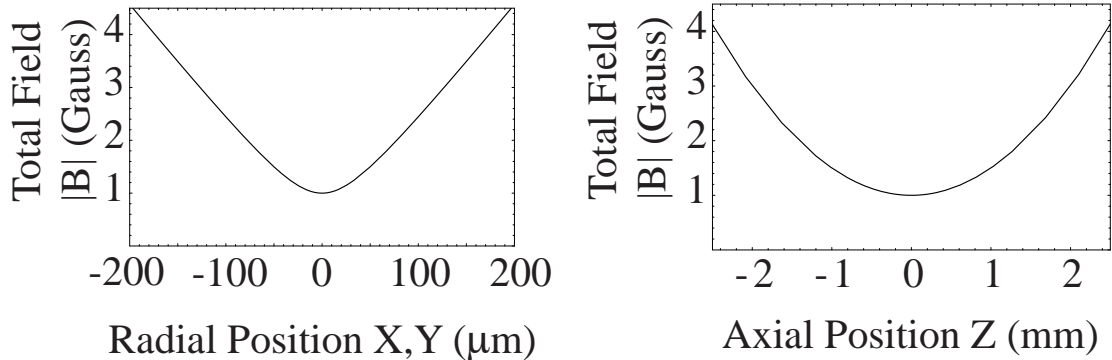


Figure 3-10: Profile of the Ioffe-Pritchard trap magnetic field magnitude. The trap parameters are $B'=223$ G/cm, $B''=100$ G/cm², and $B_0=1$ G.

where B_0 is the Ioffe bias, B' is the radial (x,y) gradient, and B'' is the axial (z axis) curvature. The energy $U = \mu_m |\mathbf{B}|$ can be expanded in a Taylor series to determine the trap frequencies.

$$\omega_{x,y} = \sqrt{\frac{\mu_m}{m} \left(\frac{B'^2}{B_0} - \mu_m B''/2 \right)} \quad (3.8)$$

$$\omega_z = \sqrt{\frac{\mu_m}{m} B''} \quad (3.9)$$

Typical trap parameters of $B'=223$ G/cm, $B''=100$ G/cm², $B_0=1$ G (Fig. 3-10, Table 3.2) have frequencies of $(\omega_{x,y}, \omega_z)/2\pi = (200, 9)$ Hz for ⁸⁷Rb in the $|1, -1\rangle$ state. In our large aspect ratio cigar shaped traps the z-axis field curvature $B''/2$ reduction in the radial trap frequencies $\omega_{x,y}$ is typically less than a few percent and can generally be disregarded. In creating traps with near spherical geometries, such as those used for lattice loading or vortex experiments, this reduction effect plays an important role and cannot be disregarded.

Majorana spin flip losses occur when atoms in a magnetic trap pass through a region of low magnetic field such that their motional and magnetic state energies are similar and hence mix. The result is that a fraction of the atoms leave the region no longer in one of the weak field seeking states and are expelled from the trap. Majorana losses can be calculated from the Landau-Zener formula.

The finite minimum bias field of the Ioffe-Pritchard trap provides good protection against Majorana losses so long as the energy E of the atoms $E \ll \mu_m^3 B_0^3 / (\hbar \omega_{x,y})^2$, the adiabatic limit of the Landau-Zener formula. For typical Ioffe-Pritchard traps, such as one with a 1G bias field and 200 Hz trap frequency this energy is equivalent to a temperature of 412 K, much greater than the overall trap depth of a few mK. However tightly confining traps with large aspect ratios are of interest for studies of lower dimensional systems. An easy way to

increase the radial trapping frequency of a Ioffe-Pritchard trap (Eq. 3.9) is to lower the Ioffe bias B_0 . It is useful to determine how far the Ioffe bias B_0 could be reduced and still treat the trapping potential as harmonic. We estimate the length of the harmonic region as B_0/B' and equate it to the spatial size of ground state quantum harmonic oscillator $\sqrt{\hbar/m\omega}$. This turns out to be equivalent to reasserting the condition for the onset of Majorana losses $\mu_m B_0 = \hbar\omega_{x,y}$. The maximum radial trap frequency in this limit is $\omega_{x,y} = \left(\frac{\mu_m^2 B'^2}{m\hbar}\right)^{1/3}$. For $|1, -1\rangle$ atoms in a 200 G/cm field gradient this gives a maximum calculated 18 kHz trap frequency in a bias field of 18 mG. Technical limitations to lowering the Ioffe bias B_0 to these levels are drifts and noise in the ambient magnetic field. Jitter in magnetic field will cause the trap frequency to fluctuate and randomly squeeze the condensate, causing heating and complicating measurements. Another complication is that the magnitude of the RF evaporation fields will become comparable to that of the Ioffe bias and the atoms behavior will be strongly affected by the RF coupling.

Gravitational Sag

The force of gravity pulls the center of the trap below the magnetic field minimum. This introduces a transverse component to the magnetic field such that it is oriented at an angle θ from the long axis (z) of the condensate. Quantifying the difference in these two directions is important for experiments where different polarizations of probe light cause different effects, such as in superradiance [44, 45, 68] or Quantum Zeno experiments (Ch. 4). In tightly confining magnetic traps a small sag $y_0 = g/\omega_y^2$ will result in a transverse magnetic field component $B_y = B'y_0$ that tilts the total magnetic field vector off the condensate axis by $\tan \theta = B_y/B_0$.

$$\theta \approx \frac{1}{\omega_y} \sqrt{\frac{mg^2}{B_0\mu_m}} \quad (3.10)$$

To calculate the exact effects of gravitation sag we can use a one dimensional model incorporating Eq. 3.7 to express the potential energy U of the system

$$U = mgy + \mu_m \sqrt{(B_0 - B''/4y^2)^2 + B'^2 y^2} \quad (3.11)$$

and solve for the sag y_0 at a given Ioffe Bias B_0 and trapping frequencies.

Spatial Inhomogeneity

One inconvenience to trapping atoms in an spatially inhomogeneous magnetic field is that the finite extent of the cloud will introduce differences in total magnetic field and orientation of the magnetic field across the sample of trapped atoms. While external forces such as gravity will always displace the trap center from the magnetic field minimum, large displacements will greatly increase the total inhomogeneity. These effects are important in

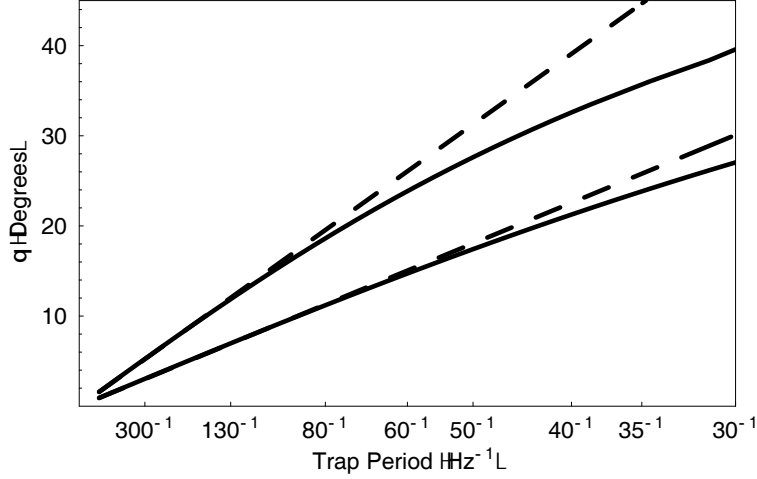


Figure 3-11: Angle θ between condensate axis and magnetic field vector as a function of radial trap frequency. Solid lines are calculated from Eq. 3.11 with $B''=100$ G/cm² (9 Hz axial trap frequency) and Ioffe bias fields B_0 of 1.0 (Upper) and 3.0 G (Lower). Dashed lines show the small sag approximation Eq 3.10. .

considering the variable effective trap depths created by an RF knife in a weak trap.

Figure 3-12: Displacement in a harmonic oscillator increases the inhomogeneous magnetic field spread.

$$\Delta B = \frac{2mg\Delta y}{\mu_m} \quad y_0 > \Delta y \quad (3.12)$$

$$\Delta B = \frac{mg\Delta y}{\mu_m} + \frac{E}{\mu_m} \quad y_0 < \Delta y \quad (3.13)$$

$$\Delta y = \sqrt{\frac{2Ey_0}{mg}} \quad (3.14)$$

where $y_0 = g/\omega_y^2$ is the displacement from the magnetic field minimum and Δy is the spread in location for an energy E . The trap switches from being slightly sagged to weak when $mg y_0 = 2E$.

3.7.2 Circuitry

The IGBTs are designed for use in AC/DC power switching hardware, so can be run at most at half their rated current value due to power dissipation problems. The IGBTs are limited by their internal thermal resistance. We used water cooled copper heatsink baseplates with a thin layer Arctic Silver thermal grease to provide the best thermal contact to the

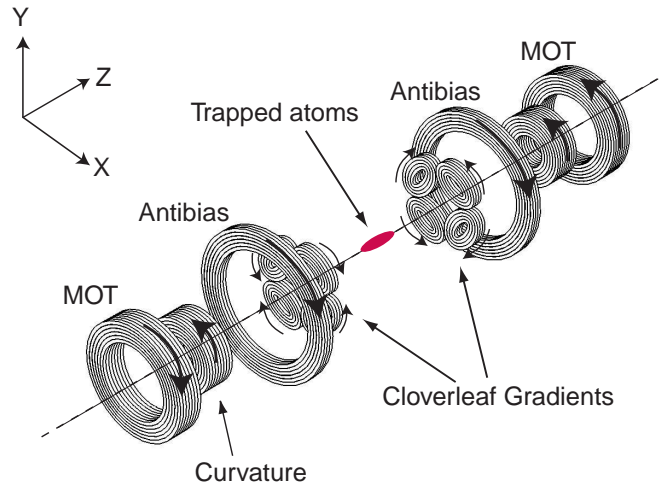


Figure 3-13: Exploded view of the cloverleaf style Ioffe-Pritchard trap coils. Arrows indicate the direction of current flow. MOT coils are energized during magnetic trapping.

IGBT baseplate. The baseplates were lapped on a granite block to provide a lower thermal interface resistance. At peak power the IGBTs dissipate a maximum of $\sim 1\text{kW}$.

Coil	Winding		Current (A)	Inner \emptyset (cm)	Field
	Turns	Layers			
Antibias	3	6	95	10.5	$B'' = +9 \text{ G/cm}^2$ $B_0 = -243 \text{ G}$
Curvature	8	6	95	3.2	$B'' = +90 \text{ G/cm}^2$ $B_0 = +251 \text{ G}$
Gradient	3	4	470	0.8 x 2.3	$B' = 223 \text{ G/cm}$
MOT	7	4+2 ^a	15	~ 7 , to fit	16.5 G/cm in \hat{z}

Table 3.2: Magnetic trap coil winding and performance specifications. Fig. 3-13 illustrates their assembly and direction of current flow.

^aSegmented for improved cooling.

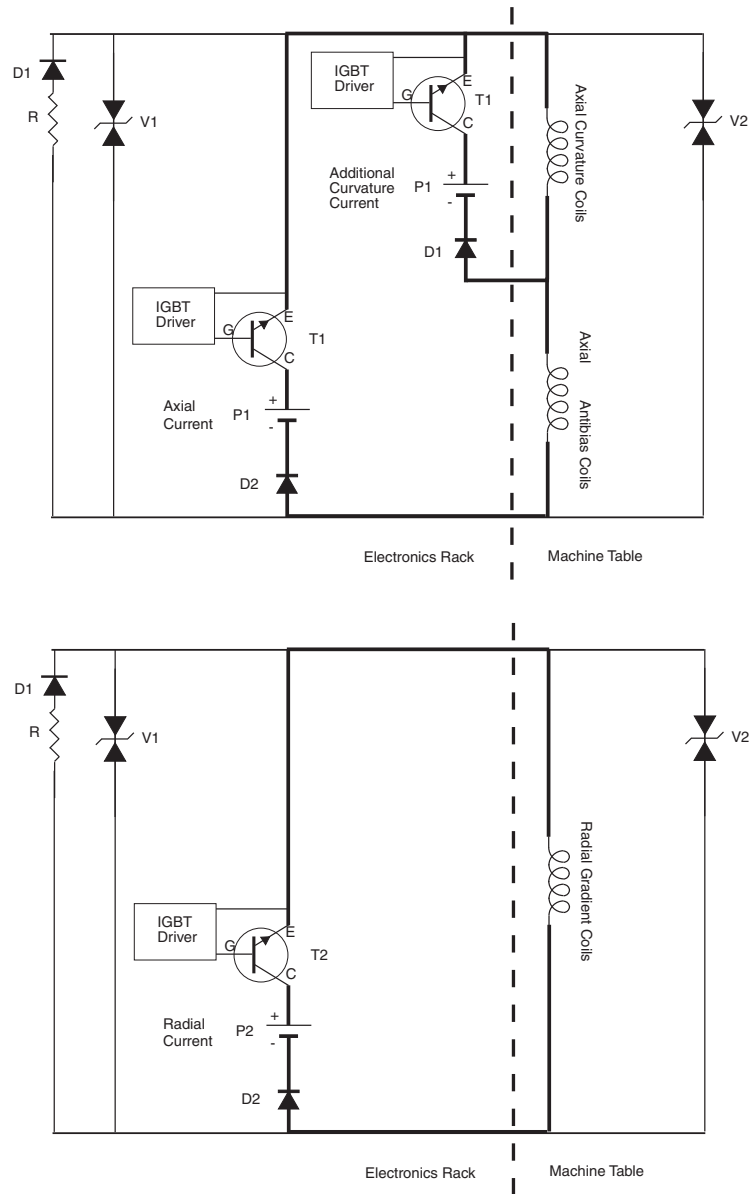


Figure 3-14: Magnetic trap electrical circuits. Heavy lines indicate thick 0000 Gauge stranded copper wire. Components: P1 Lambda EMI EMS 20V 250A 5kW DC Power supply, P2 Lambda EMI EMS 30A 500V DC 15kW Power supply, D1 a high breakdown voltage diode rated for transient currents in excess of 500 A, D2 International Rectifier SD600N04PC high current diode (600 Amp, 1200 V, attached to a water cooled plate), Varistor V1 GEL8130L10 (130 V), Varistor V2 ZNRV20180 (30 V), R 1Ω thin film non-inducting resistor. T1 and T2 are PowerEx CM600HA-24H and CM1000HA-24H Integrated Gate Bipolar Transistors, mounted to water cooling plates. IGBT Driver is a PowerEx BG1A-F circuit board.

3.7.3 Turnoff

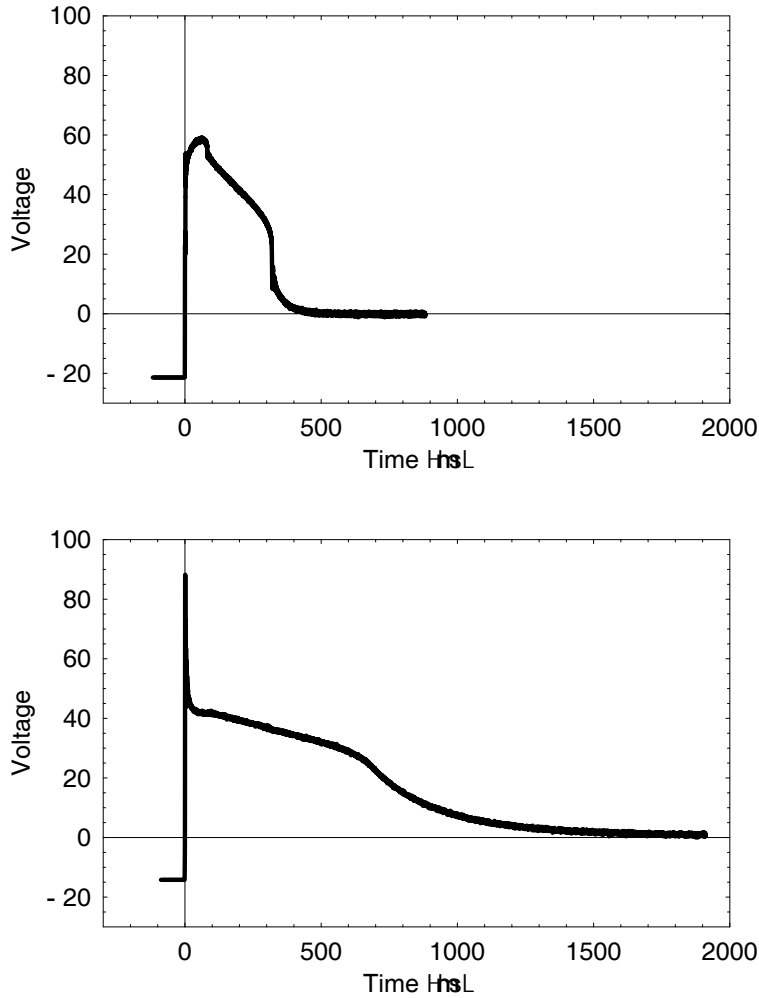


Figure 3-15: Magnetic trap electrical turnoff characteristics. Upper is voltage measured across radial confinement gradient coils. Lower is voltage across axial curvature and antibias coils. The linear and exponential decay regions show that the turnoff is first limited by the varistor and then by diode/resistor component of the circuit.

The large voltage spikes (Fig. 3-15) from quickly turning off the large inductive loads of the magnetic trap coils can damage the delicate computer control systems. All control signals to the magnetic trap power supplies and switching circuits were isolated with either an INA117 high common mode voltage difference amplifier for analog signals or a NEC PS2501-1 opto-isolator for digital signals. The electrical turnoff of the magnetic trap measured in Fig. 3-15 by RF resonance is much shorter than the magnetic field decay observed by the atoms in Fig. 3-16 because of eddy currents induced in the stainless steel structure of the vacuum chamber surrounding the magnetic trap.

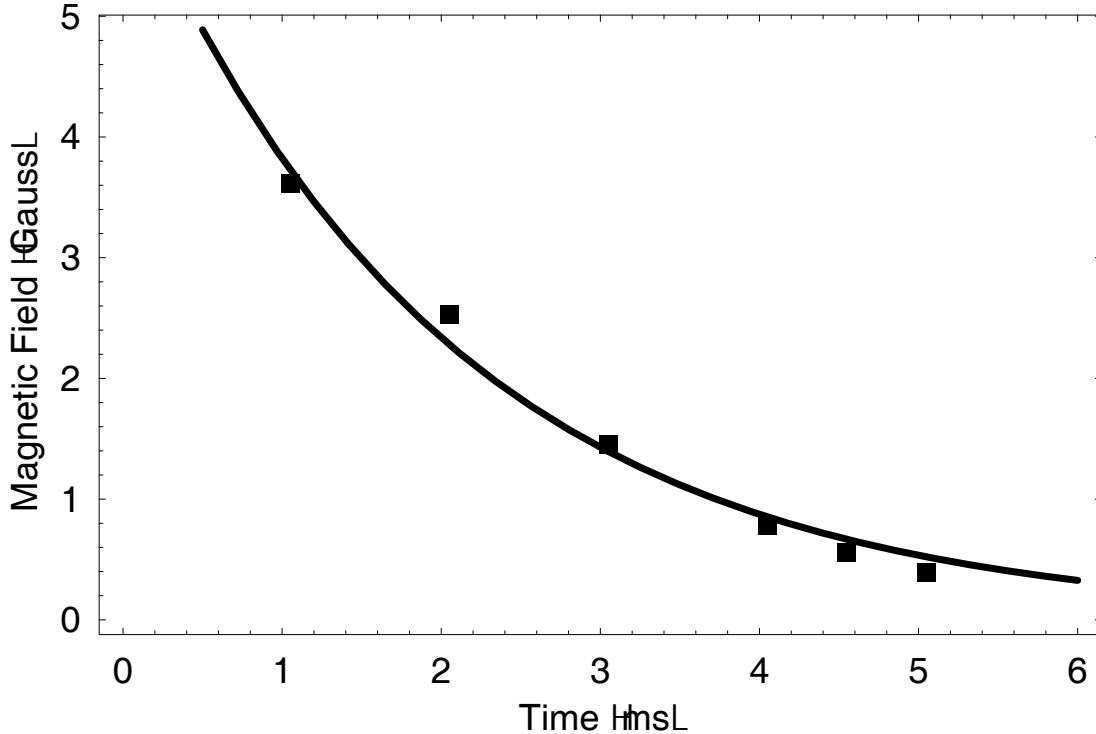


Figure 3-16: Decay of magnetic field after IGBT turnoff in main chamber as measured by RF resonance. Magnetic trap with 48 A axial, 192 A gradient currents before turnoff. Trap frequencies 63x63x6.6 Hz. Trap magnetic field minimum 3.0 G. Decay is fit is to $B_0 \exp(-t/\tau)$ where $B_0 = 6.24 \pm 0.45$ G and $\tau = 2.03 \pm 0.15$ ms.

3.7.4 Wire

Both the slower and the magnetic trap coils were fabricated using square hollow core (0.125 in./side, 0.032 in. wall) Alloy 101 soft temper copper tubing from Small Tube Products, Inc. of Altoona, PA, wrapped with double Dacron glass fuse insulation by Essex Group Inc., Magnet Wire & Insulation of Charlotte, NC. The coils are held together with Hysol Epoxi-Patch 1C White high temperature epoxy that is bakable to 170°C. Chilled water is forced through the hollow core of the copper wires to dissipate the ≈ 10 kW of power generated from resistive heating in the magnetic trap and Zeeman slower coils. 200 psi of differential pressure is required for sufficient coolant flow. We designed all our coils to increase the cooling water temperature by less than 50°C. Ch. 3 of Ref. [69] has an extensive discussion of water cooling in continuously powered resistive magnets. For our wire the following empirical relationships and numbers were measured,

$$\rho = 2.65 \times 10^{-3} \quad (3.15)$$

$$Q = 2.07\sqrt{\frac{\Delta P}{L}} \quad (3.16)$$

$$\Delta T = 259I^2\rho\sqrt{\frac{L^3}{\Delta P}} \quad (3.17)$$

where Q is the water flow rate in ml/sec, $I^2 \rho L$ is the power dissipated by the coil, ΔP the pressure drop in psi (1 psi=6.89 kPa), and L the length of the coil in meters.

3.7.5 Cooling

To dissipate the ~ 15 kW of heat our BEC machine generates during operation we use a closed loop Thermo NESLAB System III Liquid to Liquid heat exchanger tied to the MIT chilled water distribution system. The 40 psi pressure provided by the NESLAB is sufficient to cool the IGBTs and the rubidium oven cold plate TECs, but must be boosted to ~ 230 psi by a high pressure pump to provide sufficient flow for cooling the magnetic trap. Table 3.3 lists flow rates for the magnetic trap.

The buildup of algae in closed loop chilled water systems is a major source of clogging. We treat the water with 1gm per 3.7 L of Chloramine-T [70] to retard these growths. Fernox Copal Central Heating Protector is also added as a corrosion inhibitor at a concentration of 100mL per 6 L. This is of particular importance to protect any aluminum components from electrolytically disintegrating.

Ch. 3 of [69] has a good discussion of cooling high current current magnets.

Coil	East (ml/min)	West (ml/min)
Grad A	1330	1450
Grad B	1450	1400
Grad C	1450	1400
Grad D	1400	1400
Axial Antibias	660	800
Axial Curvature	610	580
MOT A	680	600
MOT B	870	850

Table 3.3: Magnetic trap water cooling flow rates for the BEC IV magnetic trap. Measured on September 10, 2005 before the low pressure return manifold. Distribution manifold pressure 245 psi. The East side is the Laser table side of machine. The West side is control computer side of machine.

Additional resources on Ioffe-Pritchard magnetic traps can be found in Sec 2.3.2 of [71] and Ch. 5. of [72].

Coil	East (m Ω)	West (m Ω)
Grad A	5.150	4.935
Grad B	5.095	4.970
Grad C	5.205	4.990
Grad D	4.995	5.120
Axial Antibias	185.8	185.5
Axial Curvature	208.0	207.7
MOT A	19.92	20.73
MOT B	13.47	13.98

Table 3.4: Magnetic trap resistances. Gradients measured with 200A, 11.7 V total drop. Axial with 100 A, 10.9 V. MOT with 10 A, 2.38 V. Measured at junction between water cooled copper leads and lugs.

3.7.6 Fabrication

All of the components for each half of the magnetic trap were epoxied together for stability. Each assembly was then mounted in the bucket windows with an aluminum mounting plate backed by four threaded Alloy 316 stainless steel rods. No ferromagnetic materials were used in the mounting because of concern for irreproducibility from hysteresis effects. Table 3.2 lists the windings and typical parameters for each coil.

3.8 Evaporation

Evaporative cooling works by selectively removing hot atoms from the trapped cloud, while the remaining atoms rethermalize to a lower temperature. The efficiency of cooling depends on η , the ratio of trap depth or energy of the escaping atoms to the temperature $k_B T$, and is reduced by the rate of heating. The speed of evaporation depends on how quickly the atoms rethermalize through elastic collisions. The elastic collision rate is the product of the scattering cross section $\sigma = 8\pi a^2$, density n , and the mean velocity \bar{v} of the atoms.

In a magnetic trap evaporation is implemented through RF induced transitions between trapped and untrapped states. A given RF frequency corresponds to a shell of constant $\mu_m |\mathbf{B}|$ where the transitions occur. Atoms that pass through this shell enter untrapped states and are lost; thus RF provides a flexible mechanism to control the magnetic trap depth. Our RF antenna consists of two rectangular loops of wire, 10 cm x 2 cm, positioned 3 cm above and below the condensate as depicted in Fig. 3-2. Evaporation works equivalently well for ^{23}Na and ^{87}Rb , with ^{23}Na 's lower mass resulting in higher trap frequencies, which roughly compensates for its smaller elastic cross section (Table 3.5).

To evaporate thermal atoms to a BEC, we sweep the RF frequency over several seconds using an Agilent 33250A synthesizer amplified with a 5 W RF amplifier (Mini-Circuits ZHL-5W-1). Typical evaporation curves for ^{87}Rb would ramp from 60 MHz down to ~ 0.8 MHz in 15 to 40 seconds, with similar parameters for ^{23}Na . Forced RF evaporative cooling

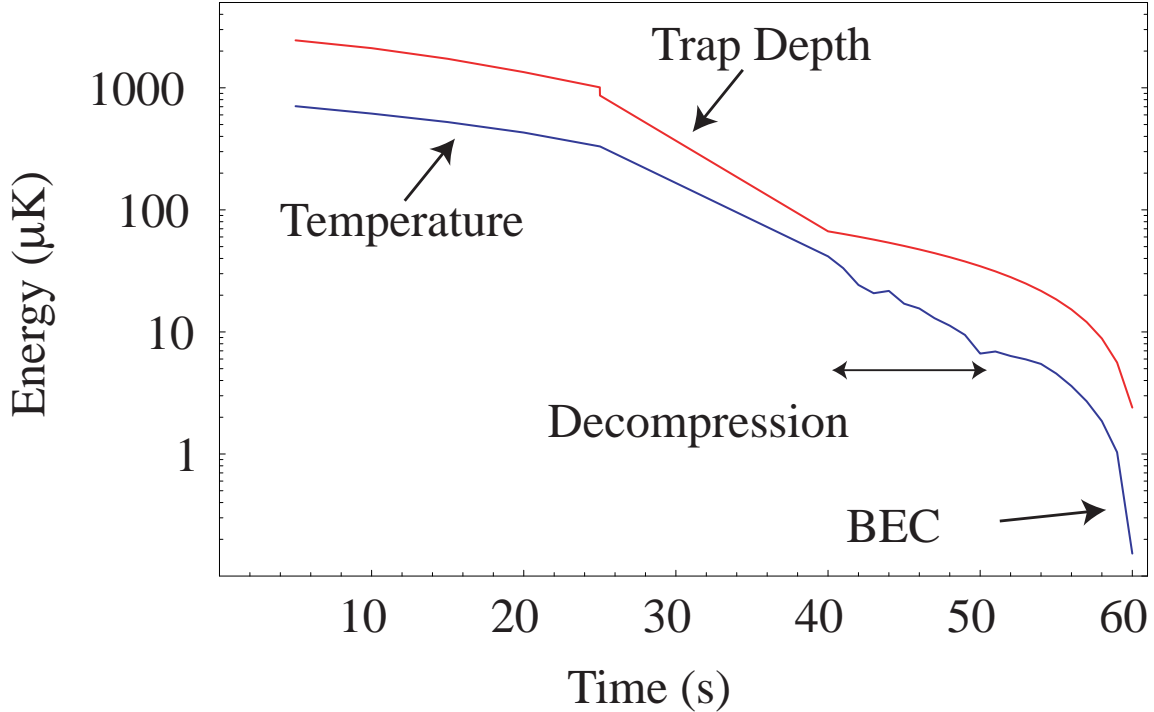


Figure 3-17: Typical temperature and trap depth during evaporation to BEC in ^{87}Rb . The trap is decompressed between $t=40\text{-}50$ s by changing the trap parameters $B' = 223 \rightarrow 54$ G/cm, $B'' = 99 \rightarrow 25$ G/cm 2 , and $B_0 = 1.4 \rightarrow 0.87$ G. Temperature was determined by fitting after ballistic expansion.

is very efficient, increasing phase space density by $> 10^6$ (Table 2.1). Fig. 3-17 shows the drop in temperature as the trap depth (calculated from the RF frequency) is lowered during evaporation of ^{87}Rb . Evaporation curves are frequently adjusted in the interest of tuning evaporation speed, atom number, density, and/or reproducibility. For instance, the atom number can be increased by decompressing the magnetic trap near the end of the evaporation. This reduces the effects of three body recombination heating by lowering the final condensate density. Such decompression techniques have allowed us to create nearly pure condensates with $N_c \approx 20 \times 10^6$ in both ^{87}Rb and ^{23}Na with lifetimes in excess of 5 seconds.

Decompressing the trap shifts its center due to gravitational sag and imperfections in the balance of magnetic fields between the coils. Such movements can excite oscillations in the cloud, which results in the condensation of BECs which are not at rest. Even in the absence of excitations, the magnetic field gradients must exert a force on the atoms which is greater than gravity for them to remain trapped. This limits the extent to which magnetic traps can be decompressed. Specially designed gravito-magnetic traps have been decompressed down to 1 Hz [38] to investigate very cold, dilute BECs.

3.9 Anomalous Losses in Deep Traps

3.9.1 Motivation

Transporting atoms in an optical tweezer requires an optical gradient steep enough and a trap depth deep enough to retain the atoms as they are accelerated. In our setups the optical axis is the same as the direction of the transport. This means that the direction of weakest confinement is also the direction which is accelerated during transport. The restricted optical access (Fig. 3-2) limits our ability to make a steep optical potential with a tight focus. In adapting the BEC transport technology from ^{23}Na BECs [35] to ^{87}Rb the greater mass required us to use more optical power and hence a greater trap depth in order to make a sufficiently steep optical potential for transport. Large ^{87}Rb BECs held in optical traps more than a few μK deep were observed to decay at a rate much greater than that expected from three body recombination. While three body related losses were observed in optically trapped ^{23}Na [35], the factor of four difference in the three-body rate coefficients (Table 3.5) was insufficient to explain this major discrepancy in behavior.

	^{87}Rb	^{23}Na
D ₂ line λ (nm)	780	589
D ₂ linewidth $\Gamma/2\pi$ (MHz)	6.1	9.8
Gravity mg/k_B (nK/ μm)	102	27
Gravity $mg/g_F m_F \mu_B$ (G/cm)	30	8.1
Three body constant K_3 (cm^6/s)	8×10^{-30} [73]	2×10^{-30} [74]
Scattering length a (nm)	5.3 [75]	2.8 [76]
Recoil velocity v_r (mm/s)	5.9	29

Table 3.5: Select properties ^{87}Rb and ^{23}Na F=1, $m_F = -1$ ground states. Unless noted, quantities are derived from Ref. [77] and [51].

3.9.2 Technique

The anomalous losses from dense ^{87}Rb BECs in deep traps was investigated in a magnetic trap instead of an optical trap. While it is easier experimentally to create tight trapping and hence high densities in an optical trap, both the trap frequencies and trap depth are functions of the optical power. This makes it difficult to separate density dependent effects, which are strongly affected by the trap frequency, from trap depth effects. In contrast, in a magnetic trap the trap depth can be controlled independently of the trap frequencies by adjusting the RF frequency which flips atoms to untrapped states.

At typical densities of condensates, the lifetime and heating are usually dominated by three-body recombination decay. Three body recombination results from the simultaneous

collision of three atoms which results in the formation of a diatomic molecule. The diatomic molecule and remaining atom fly apart with a total kinetic energy equal to the binding energy of the diatomic molecule, typically in the highest vibrational state. The molecular binding energy can be estimated from the scattering length as $E_0 \sim \hbar^2/ma^2$ [78] ($\sim 200\mu\text{K}$ in ^{87}Rb , $\sim 2.7\text{ mK}$ in ^{23}Na).

3.9.3 Theory

There are two possible processes, both involving secondary collisions, which can greatly enhance the heating and losses due to the primary three-body collisions. The first process is collisional avalanches, similar to a chain reaction, where the energetic products of three-body recombination collide with additional atoms while leaving the condensate. This process depends on the collisional opacity $\sim n\sigma l$, where $\sigma = 8\pi a^2$ is the atom atom scattering cross section, and should increase dramatically when the condensate exceeds the critical opacity of 0.693 [79]. This process occurs entirely within the condensate volume and hence is independent of trap depth.

The second process can already occur at lower collisional opacities and relies on the retention of primary or secondary collision products by the trap in the so-called Oort cloud [71, 80]. The retention of these atoms in the trap can cause heating and loss in the condensate as they oscillate through the condensate volume. The retention of collision products in the Oort cloud should depend on whether the trap depth is larger or smaller than their energies.

3.9.4 Results

Fig. 3-18 shows the initial loss rates measured for a large and a small BEC as a function of the magnetic trap depth. At low trap depths ($5\mu\text{K}$) both the large and small condensate decay rates are in agreement with established three body recombination rates [73]. Therefore, the avalanche effect does not significantly contribute to the observed decay rate, although the calculated collisional opacity for the larger condensate was 0.88 and may not be far away from the onset of avalanches. In Ref [79] evidence for avalanches was observed at a collisional opacity of 1.4.

At high trap depths, the decay rate strongly increases for larger condensates and shortens the lifetime to less than 500 ms. In contrast, at low trap depths the large condensate had a lifetime of greater than 20 seconds, in agreement with the expected losses from three body decay. For trap depths greater than $\sim 50\mu\text{K}$ the large ^{87}Rb condensate decay rate saturates, suggesting a maximum Oort energy.

We speculate that this enhancement of three-body related losses was not observed in ^{23}Na for several reasons. The primary decay products are mono-energetic and will escape unless the trap depth is greater than their kinetic energy (min $\sim 70\mu\text{K}$ for ^{87}Rb , $\sim 900\mu\text{K}$ for ^{23}Na). On their way out of the condensate volume, some of the primary three body decay

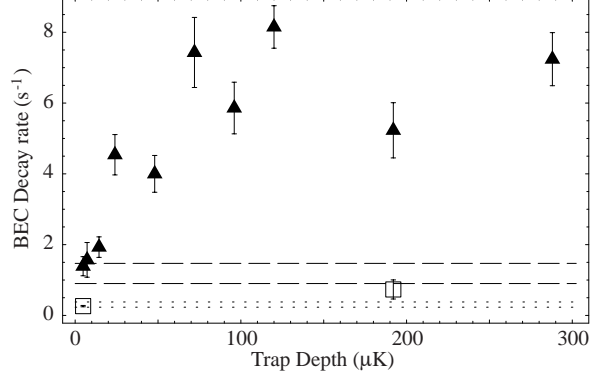


Figure 3-18: Initial loss rates for ^{87}Rb BEC in deep traps. Trap depth dependence of the loss for large and small ^{87}Rb BECs in a 220 Hz x 220 Hz x 9 Hz magnetic trap. The trap depth was controlled by RF truncation. Condensates were nearly pure ($N_c/N > 90\%$) and consisted of $F=1$, $m_F=-1$ atoms. Solid triangles are data for a large condensate, $N_c = 2.7 \times 10^6$ atoms, peak density $n_p = 6.1 \times 10^{14}/\text{cm}^3$, expected three body decay time $\tau_3 = 0.85 \pm 0.22$ s (dashed horizontal lines) [73], and calculated collisional opacity of 0.88 [79]. Open squares are data for a small condensate, $N_c = 5 \times 10^5$ atoms, peak density $n_p = 3.1 \times 10^{14}/\text{cm}^3$, expected three body decay time $\tau_3 = 3.3 \pm 0.8$ s (dotted horizontal lines), and a calculated collisional opacity of 0.32. The error bars represent the statistical uncertainty in the decay curves. Additional scatter in the data is due to fluctuations in the atom number.

products will collide with additional condensate atoms. In ^{23}Na the elastic scattering cross section σ is 3.6 times smaller than for ^{87}Rb , making these secondary collisions less likely. The products of such secondary collisions have a range of energies. In ^{23}Na these secondary products will typically have much higher energies, reducing their chance of remaining in the trap. In addition, the retained Oort particles need to collide with the condensate to cause additional loss. These subsequent collisions can further populate the Oort cloud.

For traps whose depths are in the intermediate region, below the minimum energy of the primary three body recombination products, the combination of greater primary three body decay rate, greater collision opacity, and greater fraction of secondary products retained by the Oort cloud lead to an estimated loss rate several orders of magnitude higher for ^{87}Rb than ^{23}Na in condensates of similar size and density. The anharmonic and aspheric trapping geometry reduces the frequency at which the trajectories of the particles in the Oort cloud intersect with the condensate volume.

The restricted optical access (Fig. 3-2) of our experiments limits the longitudinal (tweezer axis) trap frequency per unit trap depth. This requires optical trap depths for transporting condensates in our systems that are a significant fraction of the primary ^{87}Rb decay product energy, but a small fraction of that for ^{23}Na . Therefore ^{23}Na condensates can be easily transported using optical tweezers. For ^{87}Rb the preferred method is to transport a cloud at temperatures just above condensation, where the density is lower, and evaporate

to BEC after transport.

Chapter 4

The Quantum Zeno Effect in Bose-Einstein Condensate

The following is an expanded version of the paper “Continuous and Pulsed Quantum Zeno Effect” enclosed in Appendix C. This paper is in preparation for submission to publication.

The quantum Zeno effect (QZE) is the suppression of transitions between states by frequent measurement. Like Bose-Einstein condensation, the quantum Zeno effect is a purely quantum phenomena. It was first considered as a theoretical problem relating to the decay of an unstable charged particle as it was measured traveling across a bubble chamber [81]. Measuring the state of a classical system does not change its behavior. Quantum measurements however are invasive, irreversibly changing the system’s behavior. Under ideal continuous measurement the unstable particle would paradoxically remain in its initial state and not decay. This is the opposite to what is observed in real life bubble chambers. The QZE is the quantum equivalent to the watched tea kettle that never boils. Understanding quantum measurement is essential in linking quantum systems to their classical surroundings.

4.1 Previous Works

Several demonstrations of the quantum Zeno effect have been previously reported in the literature. These can be broadly separated in to quantitative and qualitative demonstrations. Qualitative experiments show a decrease in the transition rate with an increase in the measurement frequency. In quantitative experiments the decrease in the transition rate in terms of the measurement frequency can be predicted without any free parameters. Qualitative experiments are important for practical applications of the quantum Zeno effect, where an absolute reduction in a transition rate is the desired goal. Quantitative experiments are important for the application of the quantum Zeno effect to problems in fundamental physics, where the agreement between theory and experiment can be used to

bound the possible effects of predicted phenomena. All prior quantitative work has involved discrete pulsed measurements. The discrete nature of the pulsed measurements used in these experiments are an approximation. They are implemented through the modulation of continuous processes such as scattering photons or tunneling. Linking the continuous and pulsed regimes is therefore important to using the quantum Zeno effect for tests of fundamental physics. In addition continuous processes typically require fewer interactions and so are more economical for the practical inhibition of transfer rates between states.

Driven Rabi Oscillation

Most of the previous Zeno experiments were in the context of measuring a two level system. The system is externally driven to oscillate between the two states at a rate ω_R . Measurements will alter this evolution. For an ideal two level system starting in state A, the probabilities of finding the system in a particular state after time t are

$$P_A(t) = \cos^2(\omega_R t/2) \quad (4.1)$$

$$P_B(t) = \sin^2(\omega_R t/2) \quad (4.2)$$

where a period of time $t=\pi/\omega_R$ (a “ π ” pulse time) transfers 100% of the population from state A to state B. For times small compared with a π pulse this can be approximated as

$$P_A(t) = 1 - (\omega_R t/2)^2 \quad (4.3)$$

$$P_B(t) = (\omega_R t/2)^2 \quad (4.4)$$

Repeated measurements at a rate $1/\delta t$ will alter the two state systems evolution. After N measurements in a time $T = N\delta t$ the population in state A is

$$P_A(T) = (\cos^2(\omega_R \delta t/2))^{T/\delta t} \quad (4.5)$$

When $\omega_R \delta t \ll 1$ this can be approximated as

$$P_A(T) \approx (1 - (\omega_R^2 \delta t/4) \delta t)^{T/\delta t} \quad (4.6)$$

$$P_A(T) \sim \exp(-T\omega_R^2 \delta t/4) \quad (4.7)$$

The transfer rate from state A to state B can be made smaller by shrinking δt . By reducing δt to arbitrarily small values the probability that the the system is found in state B vanishes and the system is frozen in its initial state A. This reduction in rate, or lengthening in lifetime, is the signature of the quantum Zeno effect.

4.1.1 Pulsed Measurements

In the original demonstration of the quantum Zeno effect [82] externally driven oscillation between two ground hyperfine states of trapped ${}^9\text{Be}^+$ ions were interrupted by frequent optical scattering measurements to a third level [83]. The optical transition was chosen so that ions in the measured state would not scatter photons that returned the ion to the unmeasured state. Experiments were performed for a fixed π pulse time with $N=1,2,4,8,16,32$, or 64 measurements. Florescence detection was used to determine the population of the different states. One complication in this experiment was imperfections in the scattering measurement. Each measurement optically pumped a few of the ions into other ${}^9\text{Be}^+$ ground states. For the greatest number of measurements ($N=64$) the optical pumping corrections were equal in size to the quantum Zeno effect signal. Optical pumping is a systematic limitation to quantum Zeno experiments with ions for a large number of measurements.

A single ion version of this quantum Zeno experiment was later performed in ${}^{171}\text{Yb}^+$ [84]. Experiments with single ions are conceptually very desirable. There is no possibility of ensemble averaging or multi-body effects affecting the results. Similar to the previous ion experiment [82] experiments were performed for a fixed π pulse time with $N=0,1,2,3$ or 9 measurements. In addition to the optical pumping limitations, experiments with single ions are challenging due to the lower florescence signal levels.

The inhibition of decay in an unstable system was demonstrated in 2001 [85]. Cold neutral sodium atoms were accelerated in an optical lattice. If the acceleration was too rapid the atoms would probabilistically tunnel through the barrier rather than increase their momentum. Measurements were performed by reducing the acceleration so no atoms would tunnel. For the maximum reported number of measurements ($N=7$) an increase in the survival probability from 0.6 to 0.8 was observed. This technique may be limited by several momentum resolution issues. The measurement period must be long enough for the atoms to resolve if they are trapped or are tunneling to a lower momentum band of the lattice. The tunneling rate may depend on the temperature of the trapped atoms. These experiments also demonstrated anti quantum Zeno effect, where measurements enhanced rather than inhibited the decay out of an unstable system.

4.1.2 Continuous Measurement

Previous experimental results for the measurement of the continuous quantum Zeno effect [86–89] are qualitative rather than quantitative in nature. Comparison with theory always involved fitting the observed Zeno effect to one or more free parameters. These experiments have focused on the application of the quantum Zeno effect to suppressing precession [87–89] and relaxation [86] in spin polarized gases.

Collisions in a gas cell were used to demonstrate the quantum Zeno effect in 1997 [86]. The ortho and para nuclear spin isomer states of ${}^{13}\text{CH}_3\text{F}$ gas relax to a statistical mixture due to inelastic collisions between either two molecules or a molecule and the gas cell wall.

The higher the collision rate typically the higher the spin relaxation rate. Each type of collision acts as a quantum measurement. It was observed that in spin polarized samples increasing the pressure by 12 times reduced the relaxation rate by 60% [86].

The application of the continuous quantum Zeno effect to suppress spin precession was investigated in ions [87] and neutral atoms [88]. Spin precession occurs when a transverse magnetic field is suddenly applied to a spin polarized sample. In the quantum mechanical context, the spins are projected from being in a pure state (aligned with the magnetic field) into a superposition of states. The phases of the different states vary in time and interfere to create a rotating rather than static magnetic moment. Spatially inhomogeneous magnetic fields and collisions will then rapidly depolarize the sample.

The strongest demonstration of the continuous quantum Zeno effect in this regard was performed with trapped $^{24}\text{Mg}^+$ ions [87]. Free Larmor spin precession of ground hyperfine states from a static magnetic field was suppressed by state selective measurement using circularly polarized resonant laser light. An $>\sim 80\%$ drop in fluorescence was observed with increasing laser power, indicating that the transfer from the unmeasurable to the measured states from the Larmor precession was being suppressed by measurement. A control experiment with linearly polarized light showed no such reduction in fluorescence. Micromotion in the RF Paul trap holding the ions was estimated to Doppler broaden the resonance width by an amount comparable to the optical linewidth.

In a similar optical pumping type scheme the absorption for circularly polarized light in a room temperature ^{85}Rb vapor cell was reduced by 15% with increasing optical intensity [88]. This scheme was limited by collisional mixing of the Zeeman levels with atoms from velocity classes not addressed by the measurement laser. A transient, rather than steady state continuous quantum Zeno effect was also claimed in a room temperature ^{87}Rb vapor cell [89]. The non-exponential decay component of a Hanle-EIT transient was measured when a transverse magnetic field was quickly switched on. The data presented show the decay rate saturating with increasing optical intensity, but does not show or quote a reduction in this rate.

All three atomic style continuous quantum Zeno experiments [87–89] use a combination of Larmor precession and an intense measurement laser beam. Near saturation the laser beam significantly mixes the excited and ground states. The excited states in these systems have a hyperfine structure which will also precess. Since the state mixing near saturation is both significant and dependent on laser intensity, it is difficult to extract from these phenomenological reports a quantitative measurement of the quantum Zeno effect. In comparison, the work on the pulsed quantum Zeno effect [82, 84, 85] is in good quantitative agreement with theory for a small to moderate numbers of pulses.

4.1.3 Relevance

Usages for the quantum Zeno effect can be separated into three categories: tests of fundamental physics, quantum information, practical process enhancement. Measurements are an essential part of quantum theory in that they link quantum systems to the classic world. Tests of this fundamental aspect are important to increasing our understanding of how quantum mechanics works, or fails to work. Quantum computing and quantum cryptography have measurements at the heart of how their processes deliver useful results. State preservation is beneficial for processes which depend on a particular quantum state of matter for their operation, such as spin polarized gases for medical imaging.

Successful demonstrations of the quantum Zeno effect can bound or exclude the effects of various extensions to quantum mechanics [90, 91] such as string theory or quantum gravity. The demonstrated QZE [82] was used to bound stochastic perturbations in the Schrödinger equation to M_σ to $> 2 \times 10^{-15}$ GeV. Experiments from particle physics were used to obtain a similar bound [90]. A proposal [92] has suggested exploiting the quantum Zeno effect to detect the previously unseen effect of general relativity on electromagnetism through its coupling to a spin system. The accuracy of classical physical measurements, such as force [93], are ultimately limited by Zeno effects. The consequences of measurements inadvertently affecting the behavior of atomic clocks [91] has been investigated theoretically.

Several authors [94–97] have suggested protocols to manage decoherence and error propagation in quantum computers through the quantum Zeno effect. The security of quantum encryption protocols [98] hinges on our certainty in the nature of measurement. Interaction free measurements (IFM) [99, 100] are closely related to the QZE. In this case the detection of a photon indicates the absence of absorption by a target. In the limit of an ideal IFM a vanishingly small probability of absorption provides information about the presence or absence of a target.

Reduced absorption sensing through quantum measurement effects is of particular interest for neutron tomography [101]. Neutrons are a wonderful probe of the nuclear structure of matter but the damage induced by their absorption precludes most uses. Reducing the dosage necessary for successful image resolution could broaden its possible applications. The quantum Zeno effect is also of relevance for the preparation and preservation of spin polarized gas samples. Spin polarized gases have promising applications in the medical imaging [102, 103]. Conventional magnetic resonance imaging is dependent on the concentration of hydrogen in tissues. A spin polarized gas sample can provide a strong magnetic resonance signal of gas filled cavities such as the lungs, which have low tissue densities.

4.1.4 Limitations

In theory the Heisenberg uncertainty principle limits the rate at which meaningful measurements can be performed. For measurements made at a rate $1/\Delta t$, the energy spacing ΔE between the levels must exceed $\hbar/\Delta t$. Most real quantum systems will have imperfections

which will typically limit their performance long before reaching the Heisenberg limit. The measurement mechanism (optical scattering, collisions, etc.) will have imperfections as will the system itself. In practice such imperfections in real measurements [104] will cause parasitic losses which limit the maximum realizable suppression of evolution (freezing) [105]. The quantum Zeno effect freezes the system in its initial state. The longer the lifetime of the initial state, the stronger we can consider it to be frozen. The measurement rate which produces the maximum lifetime of the initial state demonstrates the “optimal” [105] quantum Zeno effect for that particular system. For experiments which occur in a fixed time period [82, 84, 105] this is the number of measurements N which maximizes the initial state survival probability $P(N)$.

4.2 Implementation

The quantum Zeno effect was demonstrated in a ^{87}Rb Bose-Einstein condensate where scattering measurements with photons were used to suppress the quantum evolution of a driven two level system. This is similar to the established technique in trapped ion QZE experiments [82, 84]. ^{87}Rb atoms in the $5\text{S}_{1/2} |1, -1\rangle (|F, m_F\rangle)$ hyperfine ground state were evaporatively cooled to create a Bose-Einstein condensate of $N_c = 5.0(0.5) \times 10^6$ atoms in a $\{63, 63, 6.6\}$ Hz magnetic trap [48]. We removed $\sim 99\%$ of the atoms with two nearly adiabatic RF sweeps, each of which outcoupled 90% of the atoms [106], to create a smaller condensate of $N_c = 5.0(0.5) \times 10^4$ for the start our QZE experiments. An RF knife maintained a magnetic trap depth of $5 \mu\text{K}$. Observed lifetime of the initial BEC was greater than 5 s.

4.2.1 Two level system

Our two level system consists of Bose condensed ^{87}Rb atoms in the $|1, -1\rangle$ or $|2, +1\rangle$ states. The ground hyperfine states of alkali atoms such as ^{131}Cs and ^{87}Rb are among the best characterized real quantum systems. Their robustness lead to their adoption in constructing precisions devices such as atomic clocks [107]. Both states are magnetically trappable and have identical magnetic moments at 3.23 G [75]. This creates a minimum where the total transition energy between the two states is insensitive to magnetic field. The different scattering lengths of the two states results in a density dependent clock shift [75] due to the difference in the mean field energy. To obtain a uniform transition energy across the magnetically trapped condensate the magnetic bias field was lowered slightly to 3.0 G, introducing a small inhomogeneous magnetic shift that compensated the density dependent clock shift. The difference of two quanta of angular momentum prevents a single photon 6.8 GHz microwave transition from driving resonant oscillations between the $|1, -1\rangle$ and $|2, +1\rangle$ states. Instead, a two photon transition drives oscillations between the $|1, -1\rangle$ and $|2, +1\rangle$ states (Fig. 4-2). Fig. 4-1 shows how the 6.8 GHz microwave and 1.68 MHz radio frequency

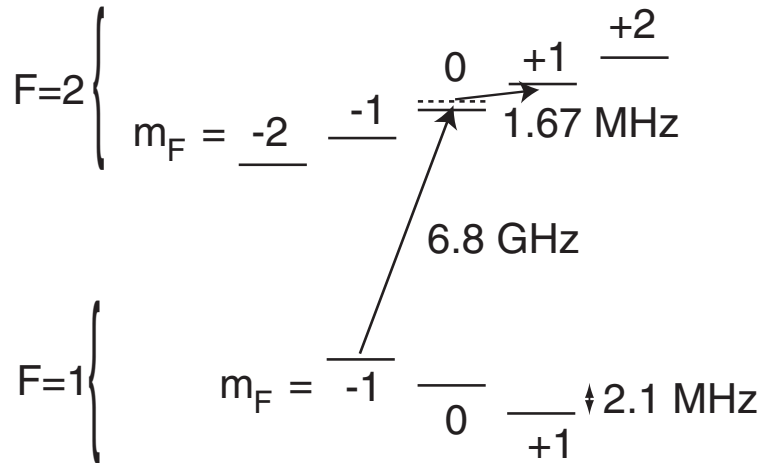


Figure 4-1: Energies of ^{87}Rb ground state hyperfine levels in a 3.0 G magnetic field. The two photon transition between $|1, -1\rangle$ and $|2, +1\rangle$ is indicated by black arrows. The 6.8 GHz microwave transition links the $|1, -1\rangle$ to a virtual intermediate $|2, 0\rangle$ state, detuned +420 kHz from resonance. The 1.67 MHz RF resonantly completes the two photon transition by linking the virtual intermediate state to the actual, on resonance $|2, +1\rangle$ state. The magnetic field splits the states of the two hyperfine levels by 2.1 MHz.

(RF) components of the two photon transition coupling through a virtual level formed by detuning 420 kHz above the $|2, 0\rangle$ state. Since we are off resonance no appreciable population is ever measured in the $|2, 0\rangle$ state. Without scattering measurements the populations of the system oscillates between the two levels as given by Eq. 4.2 at a rate ω_R .

Ground State Hyperfine Energies of ^{87}Rb

The electronic structure of ^{87}Rb can be well approximated as a single bound electron interacting with a positively charged nucleus. The ground electronic state can be considered as a single electron (spin $J=1/2$). This spin interacts with the nuclear spin ($I=3/2$ in ^{87}Rb), resulting in a splitting of the electronic ground states into two hyperfine states with slightly different energies. The Briet-Rabi formula gives the exact energies in a magnetic field of a such a spin ($J=1/2$) interacting with a spin I , each with Landé g factors g_J and g_I . The Hamiltonian of this system is

$$H = A\mathbf{I} \cdot \mathbf{J} + \mu_B g_J \mathbf{J} \cdot \mathbf{B} + \mu_B g_I \mathbf{I} \cdot \mathbf{B} \quad (4.8)$$

where \mathbf{B} is the externally applied magnetic field vector. Diagonalizing this matrix determines the energies of the various states as a function of magnetic field and is exactly solvable

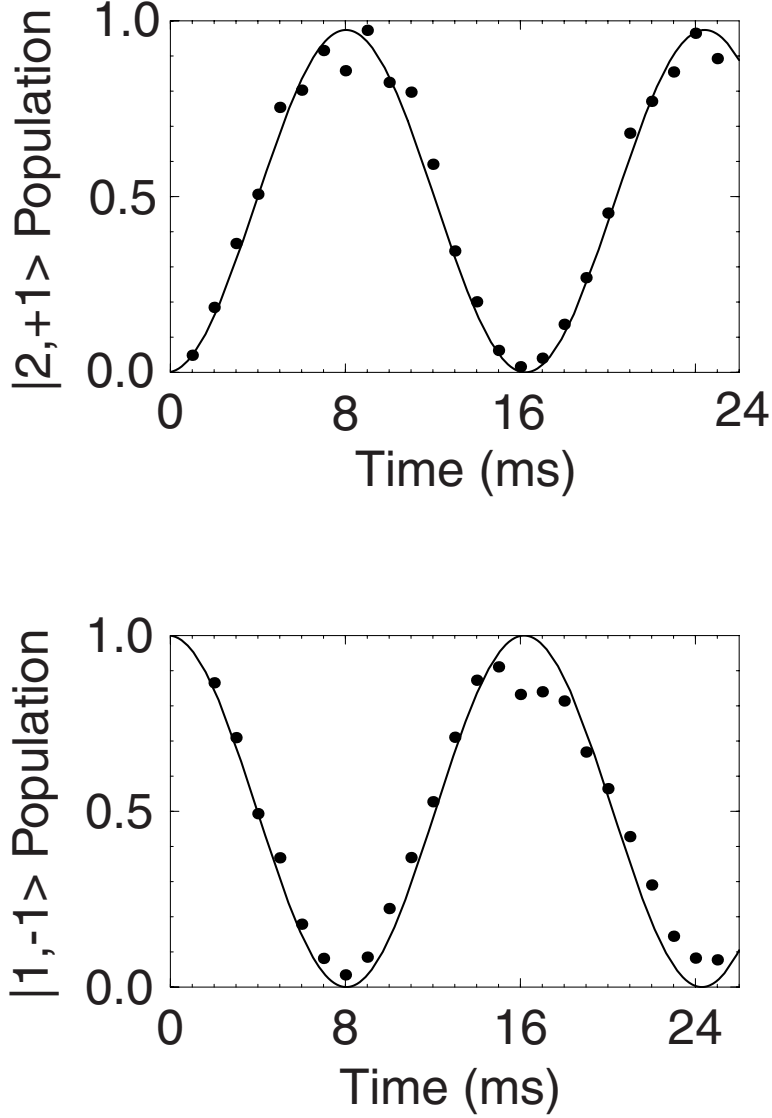


Figure 4-2: Experimentally observed time evolution of the population in the $|2,+1\rangle$ and $|1,-1\rangle$ states when driven on resonance by the two photon transition. Fit is to Eq. 4.2 with $\omega_R/2\pi = 61.5(0.5)$ Hz. The raw image data for select times in these plots are shown in Fig. 4-6

in the $J=1/2$ case. The solution is the Breit-Rabi formula

$$E |J = 1/2, I, m\rangle = -\frac{\Delta E_{hfs}}{2(2I+1)} g_I \mu_B m \pm \frac{\Delta E_{hfs}}{2} \sqrt{1 + \frac{4mx}{2I+1} + x^2} \quad (4.9)$$

where $m = m_I + m_J$, $\Delta E_{hfs} = A(I + 1/2)$, $x = (g_J - g_I) \mu_B B / \Delta E_{hfs}$, and B is the magnitude of the magnetic field. The energy splitting between states is ΔE_{hfs} at zero magnetic field. The energies can be separated into two different regimes of magnetic field intensity. In the strong field regime (Paschen-Bach) the spins are decoupled from each other

and m_I , m_J , I and J are good quantum numbers to describe the state of the system. In the weak magnetic field regime the spins are strongly coupled to each other and description of the total spin $F = I + J$ and $m_F = m = m_I + m_J$ are good quantum numbers. For a nuclear spin $I=3/2$ system such as ^{87}Rb the energies at low magnetic field approximate to

$$E |F = 2, m\rangle = +\frac{3}{8}\Delta E_{hfs} + \frac{1}{4}(g_J + 3g_I)m\mu_B B - \frac{(g_I - g_J)^2(m^2 - 4)\mu_B^2}{16\Delta E_{hfs}}B^2 \quad (4.10)$$

$$E |F = 1, m\rangle = -\frac{5}{8}\Delta E_{hfs} - \frac{1}{4}(g_J - 5g_I)m\mu_B B + \frac{(g_I - g_J)^2(m^2 - 4)\mu_B^2}{16\Delta E_{hfs}}B^2 \quad (4.11)$$

where $m = m_F$ and $\Delta E_{hfs} = h\nu_{hfs}$.

μ_B	1.399 624 624 (56) MHz/G [108]
ΔE_{hfs}	h 6.834 682 610 904 29(9) GHz [109]
g_J	2.002 331 13(20) [110]
g_I	-0.000995141 4(10) [110]
I	3/2

Table 4.1: Ground State hyperfine structure constants for ^{87}Rb .

Substituting in the ground state hyperfine parameters (Table 4.2.1) for ^{87}Rb we can give numerical approximations for the energies of each state at low magnetic field. These formulas are given in terms of the practical lab units Hz and Gauss.

$$E |F = 1, m_F = -1\rangle \approx h \left(-\frac{5}{8}\Delta\nu_{hfs} + 702,369B - 215.68B^2 \right) \quad (4.12)$$

$$E |F = 1, m_F = 0\rangle \approx h \left(-\frac{5}{8}\Delta\nu_{hfs} - 287.57B^2 \right) \quad (4.13)$$

$$E |F = 1, m_F = +1\rangle \approx h \left(-\frac{5}{8}\Delta\nu_{hfs} - 702,369B - 215.68B^2 \right) \quad (4.14)$$

$$E |F = 2, m_F = +2\rangle = h \left(\frac{3}{8}\Delta\nu_{hfs} + 1,403,350B \right) \quad (4.15)$$

$$E |F = 2, m_F = +1\rangle \approx h \left(\frac{3}{8}\Delta\nu_{hfs} + 699,583B + 215.68B^2 \right) \quad (4.16)$$

$$E |F = 2, m_F = 0\rangle \approx h \left(\frac{3}{8}\Delta\nu_{hfs} + 287.57B^2 \right) \quad (4.17)$$

$$E |F = 2, m_F = -1\rangle \approx h \left(\frac{3}{8}\Delta\nu_{hfs} - 699,583B + 215.68B^2 \right) \quad (4.18)$$

$$E |F = 2, m_F = -2\rangle = h \left(\frac{3}{8}\Delta\nu_{hfs} - 1,403,350B \right) \quad (4.19)$$

The formulas for the $|F = 2, m_F = -2\rangle$ and $|F = 2, m_F = +2\rangle$ spin stretched states are both exact and linear. Since they are not superpositions of differing nuclear and electron

spin there is no mixing of states as the magnetic field is varied. The transition energy between the $|F = 2, m_F = +1\rangle$ and $|F = 1, m_F = -1\rangle$ can be calculated. It has a minimum at a magnetic field of 3.22892 G. The quadratic variation of the transition frequency with a change in magnetic field goes as 431.36 Hz/G^2 .

Two photon resonance in ^{87}Rb

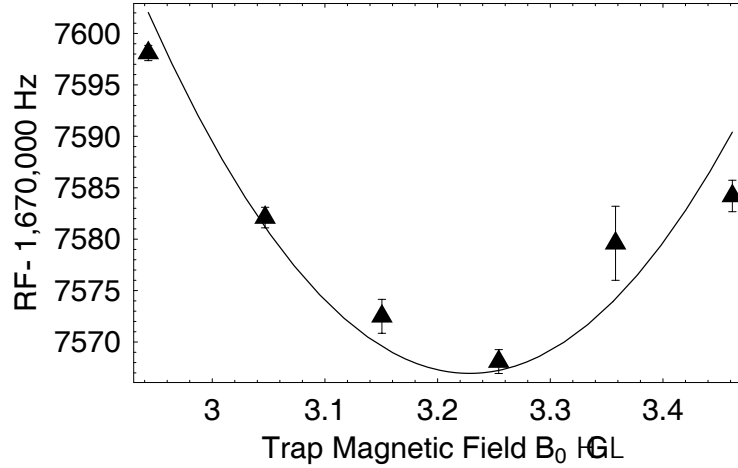


Figure 4-3: Observed two photon transition frequency as a function of trap magnetic field minimum. Curve is expected transition frequency, shifted by -540 Hz to compensate for aging of the frequency standard.

The two photon transition is driven with $\sim 5 \text{ W}$ of 6.833 GHz microwaves and $\sim 5 \text{ W}$ of 1.68 MHz RF. The microwave frequency is fixed while the RF frequency can be varied. To determine when the magnetic bias field is exactly 3.23G we measured the two photon transition frequencies at several different magnetic trap bias fields. The RF knife for evaporation operates near the one photon RF resonance. By selecting an RF knife frequency resonant with the atoms the contents of the trap are quickly lost. Measuring the loss vs. RF frequency gives a calibration of the magnetic field. Fig. 4-3 shows the dependence of the two photon transition energy as a function of observed magnetic field.

In adding together the microwave and RF frequencies we determined that our measured two photon resonance was offset from the expected value by $\sim -540 \text{ Hz}$! For comparison the clock shift is $\sim 15 \text{ Hz}$. This shift occurred because of the extreme age (> 30 years) of the reference oscillator. The RF and microwave synthesizer were synchronized to the 10 MHz clock signal provided by the microwave synthesizer. This offset did not drift during the course of the experiments. Assuming a linear drift, the quartz reference oscillator is aging at a rate of $< 2.6 \times 10^{-9} / \text{yr}$. This is reasonable value for the frequency stability drift.

4.2.2 State Measurement by Light Scattering

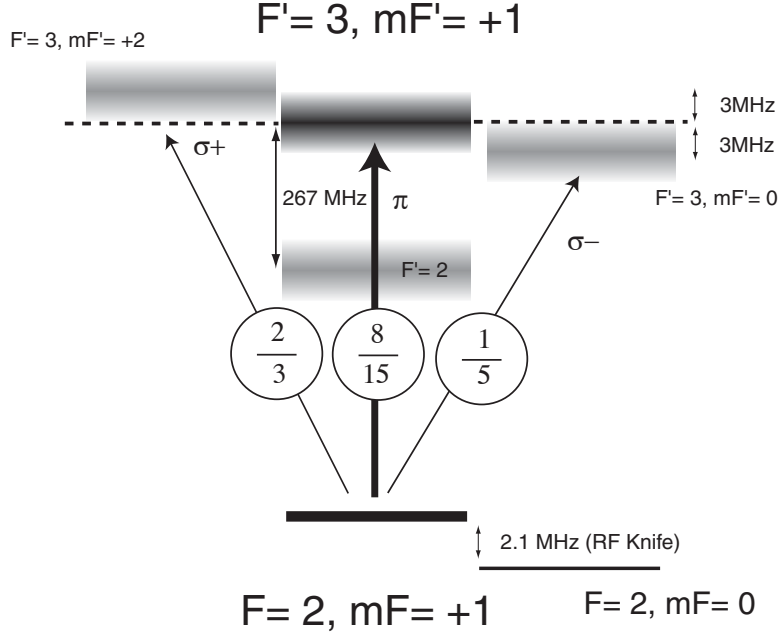


Figure 4-4: Selected energies of the $5P_{1/2}$ excited state hyperfine structure in ^{87}Rb near the 780 nm scattering measurement optical transition. The measurement light is nominally π polarized (Bold arrow) and tuned to the $5S_{1/2} |2, +1\rangle \rightarrow 5P_{3/2} |3, +1\rangle$ optical transition with a magnetic field of 3.0 G. Adjacent states are also shown, with associated transition polarization (thin arrows) and detuning. Grey bands indicate the broadening of the energy levels due to the 6.06 MHz natural linewidth. Numbers in circles are the Clebsch-Gordan coefficients $C_{e,g}^2$ for each polarization, normalized so that a closed cycling transition (between only two states) has $C_{e,g}^2 = 1$.

Scattering measurements were performed by 780 nm π polarized light tuned with an acousto-optic modulator to resonance with the $5S_{1/2} |2, +1\rangle \rightarrow 5P_{3/2} |3, +1\rangle$ optical transition at 3.0 G (Fig. 4-4). The photon recoil energy, $T_r=362\text{nK}$ distinguishes scattered atoms from the subrecoil $\mu=15\text{nK}$ BEC atoms. Repeated scatterings will eject the scattered atoms from the trap. The low condensate collisional opacity of 0.05 reduces the probability of a secondary collision with the scattered atoms before they have received the ~ 14 recoils necessary to be ejected from the trap. The laser beam has a $1/e^2$ diameter of $d_0 = 9.5(0.1)$ mm and is monitored with a photodiode. After the QZE experiment is completed we turn off the magnetic trap and allow the surviving atoms to expand with 41 ms of free expansion. An RF pulsed based state transfer technique was developed to allow simultaneous detection of the $|1, -1\rangle$ and $|2, +1\rangle$ populations. Scattering measurements of atoms in the $|2, +1\rangle$ state reduces the total BEC population. In our system the quantum Zeno effect was observed in the increasing lifetime of atoms in the initial $|1, -1\rangle$ state with more frequent scattering measurements of the $|2, +1\rangle$ state.

4.2.3 Simultaneous Detection

Accurate measurement of the Rabi frequency ω_R of the two level system is important for quantifying the quantum Zeno effect. Our condensate machine has shot to shot variations in the condensate atom number of $\sim \pm 5\%$. On a few exceptional occasions the machine has exhibited variations as low as $\sim \pm 2\%$ over the span of an hour or two. This level of stability has not been reproducible. These shot to shot variations impede the accurate determination of the Rabi frequency. Because of these fluctuations it was highly desirable to devise to image the population in both the $|1, -1\rangle$ and $|2, +1\rangle$ states simultaneously.

Selective accelerating one of the states with a near resonant Bragg pulse was initially considered. This technique had been previously used on the machine and the laser hardware was already setup. However it also required optical access along the tweezer port direction and would preclude timesharing with experiments being performed in the science chamber.

During our initial investigation of Raman superradiance [45] we were confounded by atoms which were scattered into states which did not agree with conservation of angular momentum. The problem was eliminated when we added an RF TTL switch to the RF used for evaporative cooling, turning it off before the magnetic trap turnoff. The presence of a small amount of resonant RF interacting with the changing magnetic fields was coupling atoms through adiabatic passage into other states. Knowing that $F=1$ and $F=2$ hyperfine manifolds had differing numbers of states and slightly different transition frequencies I set about inducing this effect intentionally with the goal of sweeping the $|1, -1\rangle$ and $|2, +1\rangle$ into states with different magnetic moments so that they could be Stern-Gerlach analyzed with a magnetic field gradient.

Landau-Zener Tunneling

The probability P that an atom will make a transition when the drive frequency is swept across a resonance is determined by the Landau-Zener tunneling formula.

$$P = 1 - \exp\left(-\pi \frac{\Lambda^2}{d\omega/dt}\right) \quad (4.20)$$

where Λ is the coupling between the levels and $d\omega/dt$ is the sweep rate. For low coupling (low RF power) and/or a fast sweep rate, the transfer is diabatic and does not change the apparent state of the system. In the energy picture (Fig. 4-5, Left side) the energies of the two states cross but they do not interact with each other. If the coupling is high (appreciable RF power) and the sweep rate is low the states will mix and emerge swapped at the end of the sweep (Fig. 4-5, Right side). In this case there is an avoided crossing and the coupling bends the energy levels.

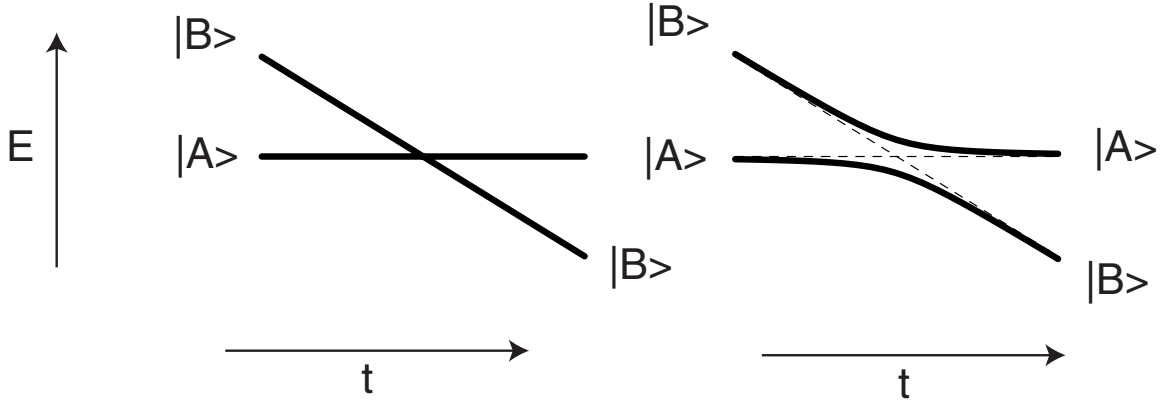


Figure 4-5: Energies of two states $|A\rangle$ and $|B\rangle$ as a function of time during a sweep across a resonance. Left figure shows the energies if the states are not coupled. A fast, diabatic, sweep will follow the heavy lines on this graph. Right figure shows the avoided crossing in energy caused by coupling. A slow, adiabatic, sweep will follow the heavy lines on this graph.

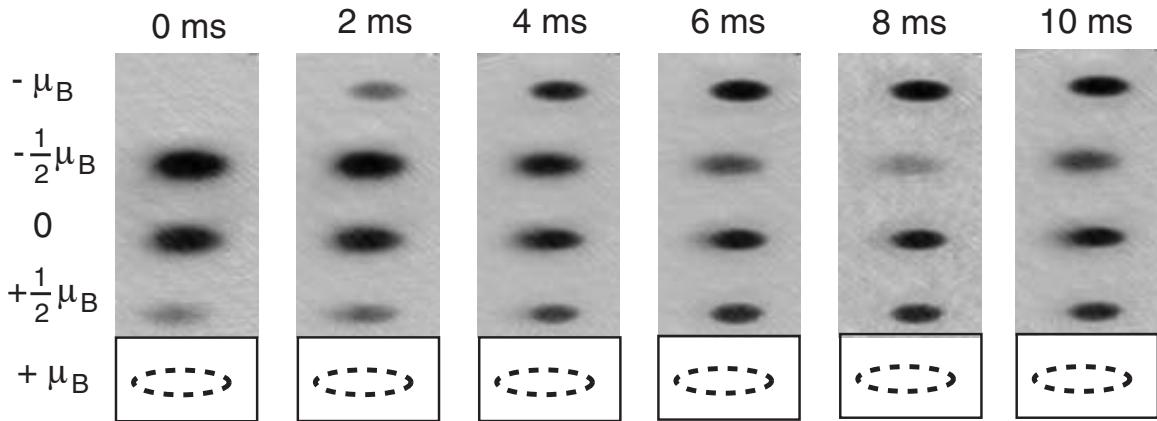


Figure 4-6: Images of Rabi oscillating atoms after state mapping RF pulse and Stern-Gerlach analysis. The top most spot corresponds with atoms initially in the $|2, +1\rangle$ state and the second from the top corresponds to atoms initially in the $|1, -1\rangle$ state. Table 4.2 gives a full listing of the state mapping ratios. As a consequence of obtaining spatial good separation between the different magnetic states the $|2, +2\rangle$ atoms were clipped out of the image. Their position is indicated by the box and dashed outline. Images correspond to select times in Fig.4-2.

State Mapping

An RF pulse with a frequency of 400kHz and 1 ms in duration was applied 4 ms after the magnetic trap turnoff to transfer the $|1, -1\rangle$ and $|2, +1\rangle$ state atoms into different, magnetically separable hyperfine states. The observed decay of the magnetic bias field during this time is graphed in Fig. 3-16, indicating that the RF transition frequency is changing

at a rate of -200 kHz/ms. A magnetic gradient was then used to perform Stern-Gerlach state analysis, spatially separating the atoms as a function of their magnetic moment μ_m . As described in Sec. 3.5.1 during the first few ms after the magnetic trap is turned off the condensate expands due to the mean field repulsion. After the first few ms the density has dropped appreciably and the expansion is collision free. To prevent collisions from inducing state changes the RF pulse was applied during this later, collision free time.

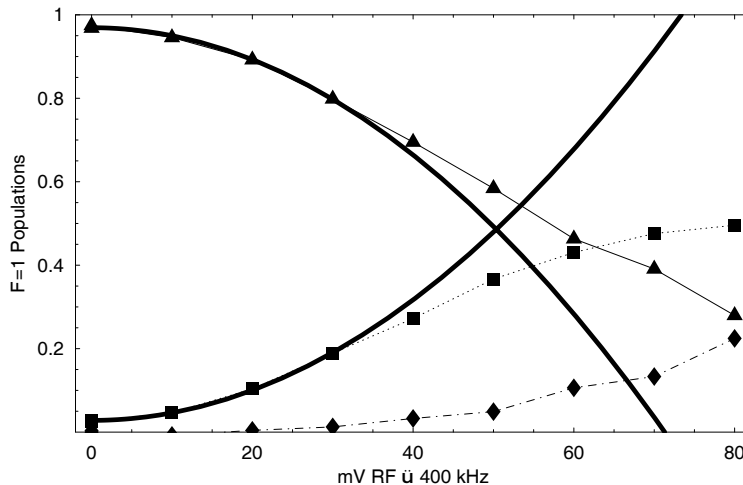


Figure 4-7: Calibration of Landau-Zener transfer between $F=1$ states from RF induced Zeeman sweep as a function of RF signal generator voltage (lab units proportional to Λ). Data is observed transfer from $|1, -1\rangle$ (Triangles) into $|1, 0\rangle$ (Boxes) and $|1, +1\rangle$ (Diamonds) as a function of signal generator RF voltage. Heavy lines are quadratic fits of the low Λ limit of Eq. 4.20 to the data.

Table 4.2 gives the mapping ratios for our two initial states into their respective hyperfine manifolds. The amplitude of the RF was adjusted so that almost no $|2, +1\rangle$ atoms were mapped into the $|2, -1\rangle$ state while the number of $|1, -1\rangle$ mapped into the $|1, +1\rangle$ was maximized. The zeroing out of the transfer to $|2, -1\rangle$ was found to be insensitive to changes in RF amplitude of less than $\sim 5\%$. The zeroing out of the population occurs because of interference between the different couplings. It is present only because the Landau-Zener transitions are neither fully in the adiabatic or diabatic regimes. For higher RF amplitudes (adiabatic limit) both initial states were mapped into the corresponding $-\frac{1}{2}\mu_B$ states, an unresolvable situation. Fig. 4-7 and 4-8 show a calibration of the transfer rate in terms of lab units (Signal generator mV RF) by approximating Eq. 4.20 for small coupling Λ . The combined fits give Λ as 61.1 (0.4) Hz/mV RF.

4.2.4 Pulsed Measurement Experiments

We measured the quantum Zeno effect induced by repeated strong measurements on a driven Rabi system. Scattering measurement pulses 10 μs in duration, power 172 μW ($s_0=0.15$),

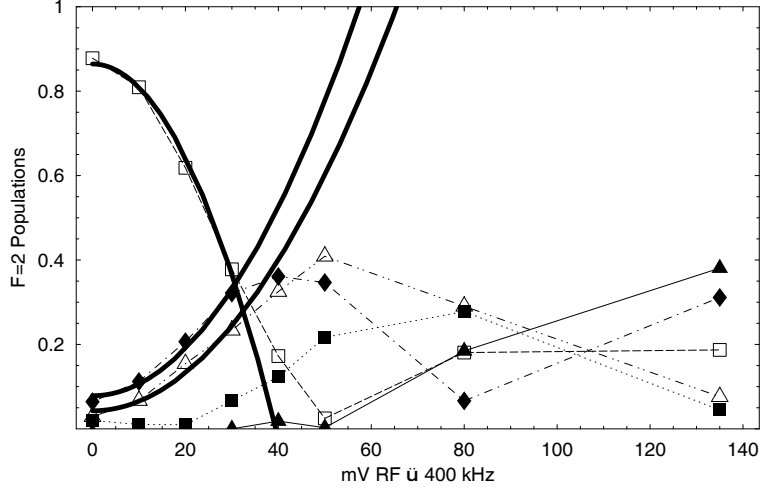


Figure 4-8: Calibration of Landau-Zener transfer between $F=2$ states from RF induced Zeeman sweep as a function of RF voltage (proportional to Λ) in lab units. Data is observed transfer from $|2, +1\rangle$ (Open Boxes) to $|2, +2\rangle$ (Open Triangles), $|2, 0\rangle$ (Diamonds), $|2, -1\rangle$ (Filled Boxes), and $|2, -2\rangle$ (Filled Triangles). Heavy lines are quadratic fits to the low Λ limit to the data. Atom number measurements were not normalized against an atom free measurement, resulting in the $\sim 10\%$ offsets in population.

μ_m		Input State		Output State
$+\mu_B$			7.9(0.7)%	$ 2, +2\rangle$
$+\frac{1}{2}\mu_B$	100%	$ 2, +1\rangle$	29.7(0.6)%	$ 2, +1\rangle$
0			20.1(1.2)%	$ 2, 0\rangle$
$-\frac{1}{2}\mu_B$			3.1(0.6)%	$ 2, -1\rangle$
$-\mu_B$			39.2(0.9)%	$2, -2\rangle$
$+\frac{1}{2}\mu_B$	100%	$ 1, -1\rangle$	3.0(0.6)%	$ 1, -1\rangle$
0			29.9(1.0)%	$ 1, 0\rangle$
$-\frac{1}{2}\mu_B$			67.1(1.6)%	$1, +1\rangle$

Table 4.2: Measured population ratios after state mapping RF pulse with $\Lambda/2\pi=8.25$ kHz (135 mV RF). States in bold are used for determination of the population in the input states.

were applied to the driven Rabi system, separated by a dark, free evolution time δt . Each scattering measurement laser pulse scattered ~ 29 photons per atom. The lifetime τ for a particular scattering measurement pulse rate $1/\delta t$ was determined by fitting the $|1, -1\rangle$ atom loss to an exponential decay curve over a range of times $> \sim 2\tau$. Fig. 4-9 shows a representative lifetime curve for the pulsed measurements.

The lifetimes for a variety of scattering measurement pulse rates $1/\delta t$ and Rabi frequen-

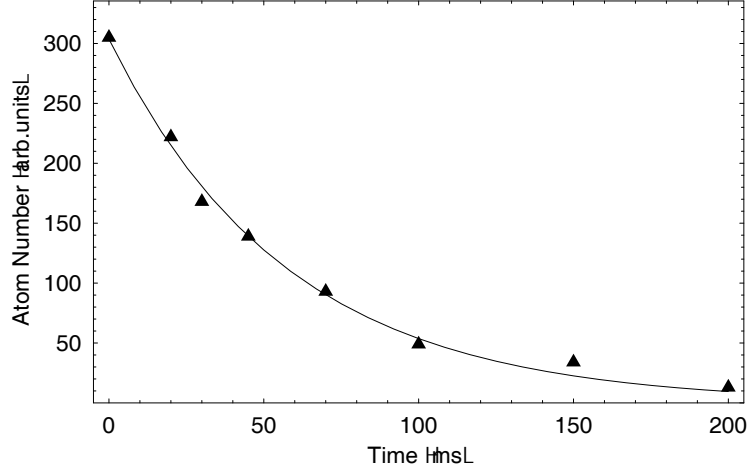


Figure 4-9: Observed decay of $|1, -1\rangle$ atoms with $10\mu\text{s}$ pulsed measurements separated by $500\mu\text{s}$ dark periods. Fit is to an exponential decay $\tau = 57.7(2.6)$. The $|1, -1\rangle$ atoms are driven with the two photon transition into the $|2, +1\rangle$ at a rate $\omega_R/2\pi = 54.6(0.5)$ Hz.

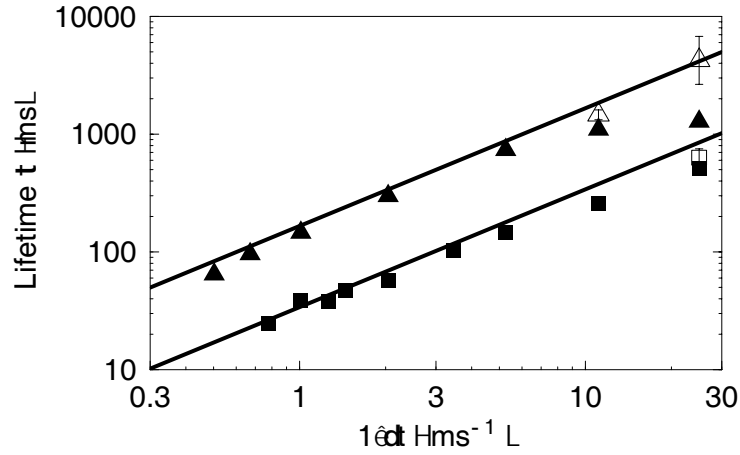


Figure 4-10: Lifetime τ of atoms in the $|1, -1\rangle$ state as a function of measurement rate $1/\delta t$ in a driven two level system. Boxes are for a driving rate $\omega_R/2\pi = 54.6(0.5)$ Hz and Triangles for $\omega_R/2\pi = 24.7(0.1)$ Hz. Filled symbols are observed lifetimes. Open symbols are lifetimes corrected for parasitic losses with Eq. 4.21 (Measured loss rate $\Gamma_m = 3.41(0.14)s^{-1}, 2.96(0.22)s^{-1}$). Solid lines indicate the expected quantum Zeno effect limited lifetime $\tau_{EP} = 1/4\delta t\omega_R^2$.

cies ω_R is depicted in Fig. 4-10. It shows the dramatic increase in the observed lifetimes (solid symbols) as the measurement frequency increases from $1/\delta t = 0.5ms^{-1}$ to $25ms^{-1}$. As expected for the strong measurement regime, the measured lifetimes were not found to be strongly sensitive to variations in optical power, pulse width (Fig. 4-19), or laser de-

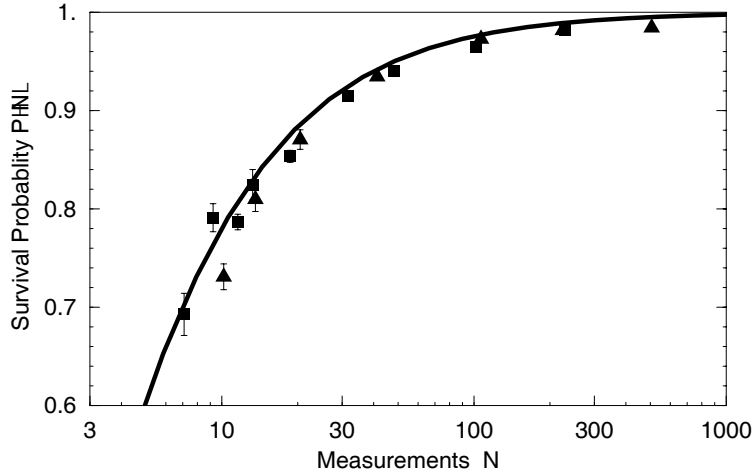


Figure 4-11: Survival probability of $|1, -1\rangle$ atoms (Boxes $\omega_R/2\pi = 54.6(0.5)$ Hz, Triangles $\omega_R/2\pi = 24.7(0.1)$ Hz) for $N = \pi/\omega_R\delta t$ measurements performed during half a Rabi period $t = \pi/\omega_R$. Survival probability is calculated from observed lifetimes $P = \exp(-\pi/\omega_R\tau_{obs})$ (Fig. 4-10). The solid line is the survival probability $P(N) = [\cos(\frac{\pi}{2N})]^{(2N)}$ for an ideal N measurement QZE.

tuning δ_L , but did exhibit a strong dependence on the Rabi frequency ($\omega_R/2\pi = 24.7(0.1)$ Hz upper line, $54.6(0.5)$ Hz lower line). The fastest measurement rates (Fig. 4-10, farthest right solid data points) showed the greatest deviations between the expected and observed lifetimes. This is a consequence of having more measurements which could induce greater parasitic loss and a longer time over which the parasitic loss effect could accumulate.

The longest QZE enhanced lifetime in Fig. 4-10 (upper left most filled data point) shows an increase of $\tau\omega_R = 198(16)$ in lifetime. This data point is near, but not demonstrably at the maximum lifetime possible for this Rabi frequency and pulse sequence. Other works [82, 84, 105] express the quantum Zeno effect in terms of the survival probability $P(N)$ per number of measurements N during a π pulse ($t = \pi/\omega_R$), a duration where absent measurements 100% of the atoms would be transferred into the other state. Fig. 4-11 translates our observed lifetimes into this general quantum Zeno basis. In these terms the greatest quantum Zeno effect is for $N=506(2)$ measurements with a survival probability $P=0.984(1)$.

To test the agreement between the predicted QZE and our observations we calculated a corrected lifetime τ_{EP} by subtracting out a separately calibrated scattering measurement parasitic loss rate Γ_m . The total observed loss rate $1/\tau$ is split into two segments: a bright parasitic loss driven fraction and a dark QZE loss driven fraction. For pulses 10μ in duration the parasitic measurement loss fraction is $f = 10\mu s / (10\mu s + \delta t)$ of the time. The dark QZE driven loss occurs for the remaining $1 - f$ of the time. For all experiments the bright fraction of the total time f was never greater than 20%.

$$\frac{1}{\tau} = \frac{1}{\tau_{EP}} (1 - f) + \Gamma_m f \quad (4.21)$$

Data points in Fig. 4-10 where this correction had a significant impact on the lifetime are indicated by open rather than filled symbols. Including the the loss correction adjustment, the combined pulsed regime data gives a QZE limited lifetime 0.836(0.014) that that of the expected value ($\frac{1}{4}\delta t\omega_R^2/\tau_{EP} = 1$).

Secondary collisions between recoiling post measurement atoms and the remaining condensate likely account for the gap between the observed and expected lifetimes. The effects from collisions are considered in detail in Sec. 4.3.6. Lower trap depths, lower densities, and stronger scattering measurement laser pulses could reduce these effects. Separate measurement of the parasitic loss rate Γ_m from the strong scattering measurement pulses showed no change in rate with the removal of the RF component of the driving two photon transition but was reduced by an order of magnitude without the microwave component. This suggests that the parasitic loss mechanism is dominated by a two photon scattering through the $|2, 0\rangle$ virtual state to the $5P_{3/2} |3, 0\rangle$ excited state.

4.2.5 Continuous Measurement Experiments

In another experiment, the same initial system was subjected to a weak continuous measurement instead of repeated strong measurements. The expected lifetime $\tau_{EC} = \gamma/\omega_R^2$ is a function of the scattering rate γ and the driving rate ω_R [111]. So showing a qualitative quantum Zeno effect in a driven system is straightforward. Turn up the laser power to increase the scattering measurement rate on one state and observe that the lifetime of the unmeasured state increases. Demonstrating a quantitative measurement of the continuous QZE is more challenging. Unlike the pulsed experiments, if the scattering measurement laser is detuned from the optical resonance several problems arise. The expected lifetime for continuous scattering measurement with a laser beam of saturation intensity s_0 and detuning $\delta_L - \delta_0$ from resonance is

$$\tau_{EC} = \frac{\gamma}{\omega_R^2} = \frac{\Gamma s_0}{2\omega_R^2} \left(\frac{1}{1 + 4 \left(\frac{\delta_L - \delta_0}{\Gamma} \right)^2} \right) \quad (4.22)$$

where δ_L is our independently controlled detuning, δ_0 an offset correction which is ideally 0, and Γ is the natural linewidth of the transition.

The first problem is that detuning of the laser from resonance will reduce the scattering rate. The second is that we need a good calibration of the saturation parameter s_0 at the atoms to determine the absolute scattering rate γ . In addition if the laser light is off resonance it will induce an AC Stark Shift δ_{RF} in the two photon resonance, reducing the effective Rabi frequency if the drive frequency is not adjusted. Fortunately the AC stark

shift is directly related to the scattering rate. The Stark shift in a multilevel atom [112] such as ^{87}Rb is

$$\delta_{RF} = s_0 C_{e,g}^2 \frac{\delta_L - \delta_0}{1 + (2(\delta_L - \delta_0)/\Gamma)^2} \quad (4.23)$$

where $C_{e,g}^2 = \frac{8}{15}$ is the Clebsch-Gordon coefficient for our transition. By measuring the AC stark shift δ_{RF} at different laser detunings δ_L and optical powers we can perform an in-situ calibration of the scattering rate to determine expected continuous QZE lifetimes without any free parameters.

We begin all of our continuous QZE measurements by first measuring the AC Stark Shift. The upper graph of Fig. 4-12 shows an RF tuning curve, where the RF has been adjusted to determine the detuning of maximum depletion δ_{RF} for a fixed hold time. In this figure the laser has been intentionally detuned off resonance to produce a larger AC Stark shift. The RF is on resonance when the number of surviving $|1, -1\rangle$ atoms is minimized, indicating a maximal transfer rate from $|1, -1\rangle$ to $|2, +1\rangle$. At this RF frequency a decay curve for the $|1, -1\rangle$ state is measured to determine the lifetime τ_{EC} . Simultaneous detection allows us to ensure that no appreciable number of $|2, +1\rangle$ atoms are present. The off resonance AC Stark shift (Fig. 4-13) is used to make a no free parameter prediction (grey band) of the expected CW Zeno lifetimes. Fig. 4-14 shows the dramatic increase in lifetime with increasing scattering measurement laser beam power along with the expected lifetimes from the AC Stark shift measurements. Optical power from the continuous scattering measurement also broadens the two photon transition, as shown in Fig. 4-15.

Fig. 4-16 shows the dependence of the AC stark shift δ_{RF} on the laser detuning δ_L . Fitting the measured AC Stark shifts to the dispersion relation for a multilevel atom (Eq. 4.23) we were able to extract in-situ values for the saturation parameter $s_0 = 1.112(5) \times 10^{-3}$ at $3.5 \mu\text{W}$ laser power and detuning offset $\delta_0 = 0.39(0.31)$ MHz. These values were in basic agreement with that expected from our external measurements of laser beam diameter, optical power, and locking spectroscopy signal. The predicted continuous measurement lifetimes are given by Eq. 4.22 which are depicted as gray bands in Fig. 4-14 and 4-17. Similar to the longest lifetime point in the pulsed data (upper right solid triangle, Fig. 4-10), the highest power point in Fig. 4-14 shows significant deviation from the lifetime expected from Eq. 4.22. The broadening of the resonance observed in Fig. 4-17 is explained by the presence of σ^+ and σ^- polarizations from gravitational sag in the trap. This effect is explained in Sec. 4.3.4.

From the AC Stark shift measured in Fig. 4-16 and Eq. 4.22 we calculate an expected lifetime of $\tau_{EC} = 250(8)$ ms that is in agreement $0.93(0.11)$ with the observed on resonance lifetime $\tau_{EC} = 233(26)$ ms in Fig. 4-17. The highest power point in Fig. 4-14 demonstrates a QZE enhancement of lifetime $\tau_{EC}\omega_R = 162(20)$. Fig. 4-14 shows increasing lifetime with increasing scattering measurement laser power, the signature of the continuous quantum

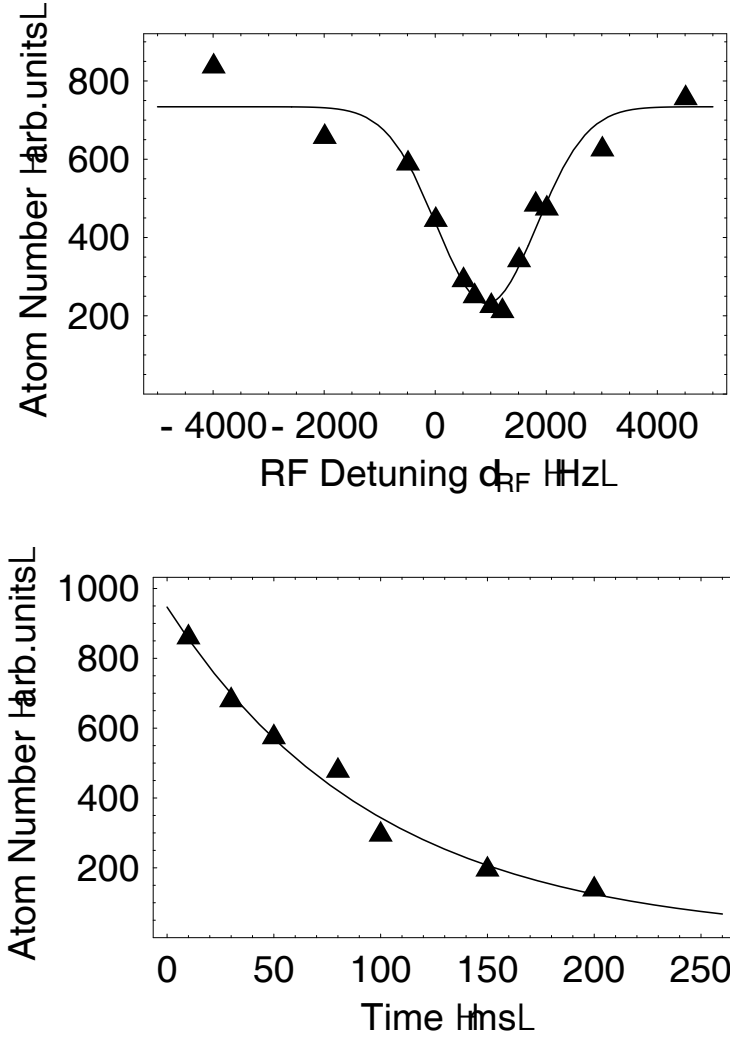


Figure 4-12: Continuous quantum Zeno effect with the scattering measurement laser detuned $\delta_L = +4.9$ MHz from the optical resonance. Upper: RF spectroscopy measurement of the AC Stark effect showing maximum loss of $|1, -1\rangle$ atoms when tuned $\delta_{RF} = +927(74)$ Hz to the shifted RF resonance (150 ms hold). Lower: Decay curve of the $|1, -1\rangle$ atoms at the shifted RF resonance. Observed lifetime is $\tau = 99(7)$. Data is for $3.5 \mu\text{W}$ laser power, $\omega_R/2\pi = 45.5(1.0)$ Hz.

Zeno effect. By matching the observed lifetimes for continuous and pulsed QZE measurements we find that $\gamma\delta t = 3.60(0.43)$, in agreement with the predicted ratio of 4 [111].

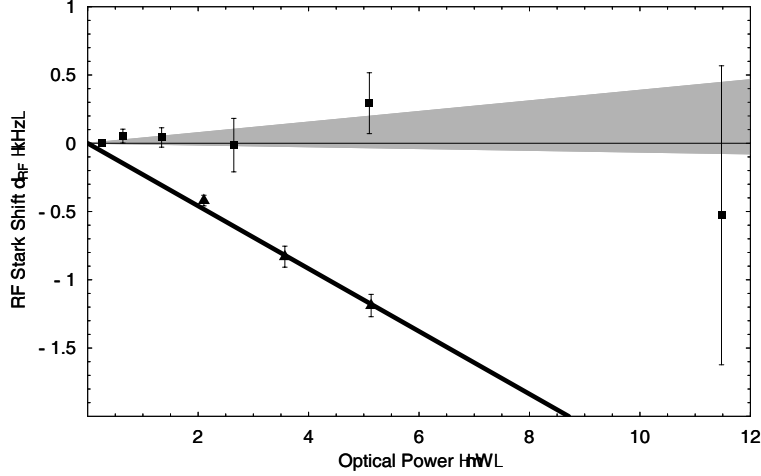


Figure 4-13: AC Stark shift of the two photon transition as a function of optical power for laser detunings both on and off $\delta_L = -5.4$ MHz resonance. Grey band shows the uncertainty in the linear fit for the on resonance case. The line is a linear fit of the off resonance AC Stark Shift and is used to calibrate the saturation parameter s_0 in Fig. 4-14.

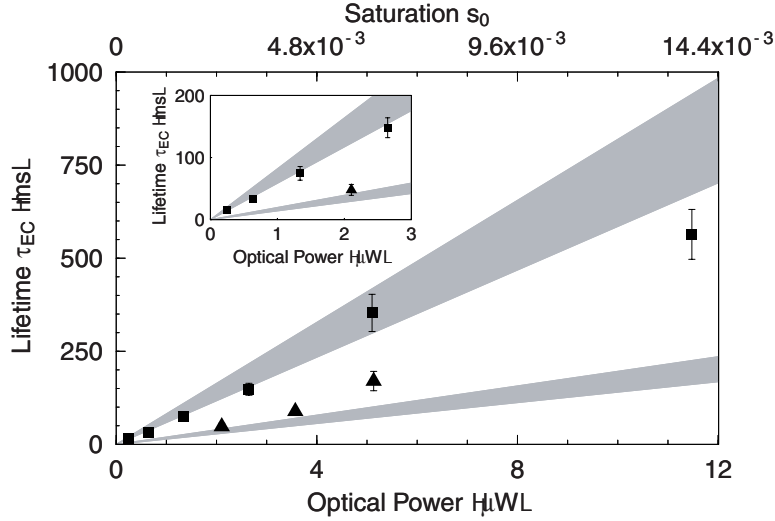


Figure 4-14: Continuous quantum Zeno effect lifetime dependence on optical power with $\omega_R/2\pi = 48.5(0.9)$ Hz for laser detunings both on (Boxes) and $\delta_L = -5.4$ MHz off (Triangles) resonance. Grey band indicates range of expected CW lifetimes from fit to separately measured off resonance AC Stark shift in Fig. 4-13. Inset highlights data at lower optical powers. The saturation parameter s_0 scale has an uncertainty of 17%.

4.3 Technical Limitations

4.3.1 Optical Opacity

Bose-Einstein condensates are typically thought of as being optically dense samples to resonant light. On the scattering measurement optical transition the optical density if

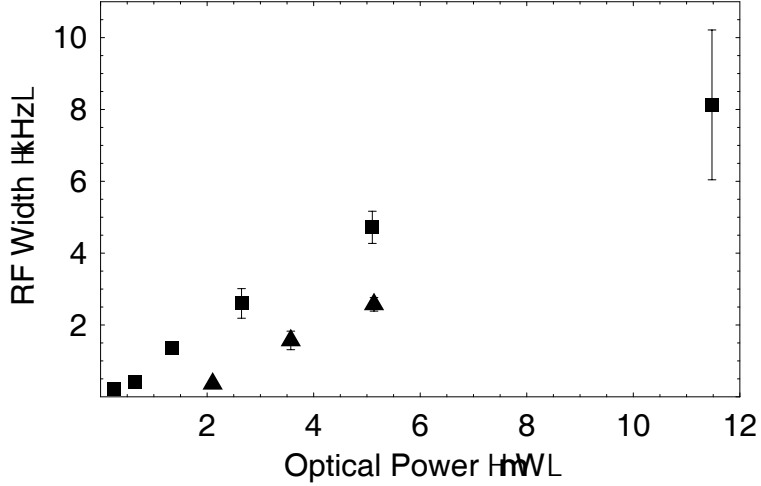


Figure 4-15: Optical power broadening of the two photon transition. Gaussian width of the RF transitions as a function of optical power for laser detunings both on (Boxes) and $\delta_L = -5.4$ MHz off (Triangles) resonance. $\omega_R/2\pi = 48.5(0.9)$ Hz.

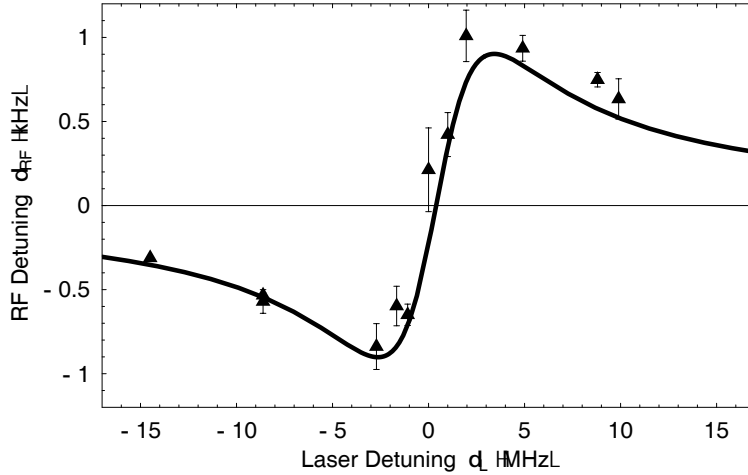


Figure 4-16: Observed AC Stark shift δ_L as a function of laser detuning δ_L . Data is for 3.5 μ W laser power, $\omega_R/2\pi = 45.5(1.0)$ Hz.

our condensate is totally in the $|2, +1\rangle$ state is ~ 25 . Atoms at the outer edge of the condensate would mask those in the bulk from the light. This optical density masking precludes successful observation of low measurement number N quantum Zeno effects [82, 84] in Bose-Einstein condensates. However when frequency measurements are made the population in the $|2, +1\rangle$ state is much smaller. For an optical density of less than 1, not more than 4% of the atoms can be in the $|2, +1\rangle$ state. Applying this limit to Eq. 4.4 gives an allowable time between measurements of less than $.1/\omega_R$. In terms of measurements per

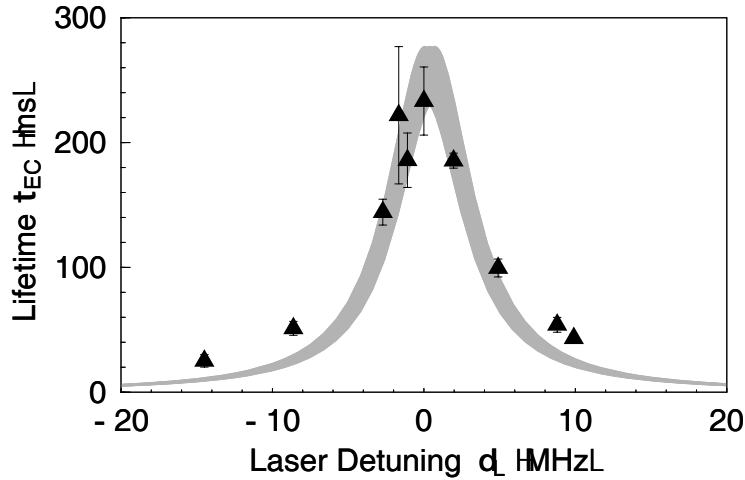


Figure 4-17: Continuous quantum Zeno lifetime as a function of the scattering measurement laser detuning δ_L . Grey band indicates range of predicted CW Zeno lifetimes Eq. 4.22 from separately measured AC Stark shift parameters. Data is for $3.5 \mu\text{W}$ laser power, $\omega_R/2\pi = 45.5(1.0)$ Hz.

” π ” time this is $N > \sim 31$.

In Fig.4-11 measurements down to $N=6$ were performed and found to be in agreement with the expected survival probability. This corresponds to a population of 6.9% or an optical density of 1.7 in the $|2, +1\rangle$ state. When an average of 29 photons per atom are incident on the condensate in a pulse only ~ 0.6 photons per pulse will make it to the back of the condensate. This number is a bit low but reasonable if we consider that photons which have already scattered one atom can scatter another. This will increase the total photon flux on the far side of the condensate.

Two processes which may affect the illumination of the condensate are optical pumping into the $F=1$ hyperfine ground states and the spontaneous light force pushing scattered atoms out of the way. Raman scattering to the $F=1$ ground state can only occur off resonantly through the $F'=2$ excited state level. The 267 MHz detuning from the $F'=3$ level suppresses this scattering process to $\sim 10^{-4}$ of the on resonance scattering. Hence Raman processes are unlikely to decrease the condensates optical opacity. If we consider the measured atoms to experience a constant acceleration from the spontaneous light force, they will move on average $0.87 \mu\text{m}$ during at $10\mu\text{s}$ pulse. This is small compared with the $8.6\mu\text{m}$ Thomas-Fermi diameter of the condensate in the direction of the laser beam.

4.3.2 RF Detuning

Ideally we would always be exactly on resonance with the two photon transition. As a practical matter we will always be detuned off resonance to some degree. It is therefore

important to characterize the consequences of detuning to determine at how far we can be detuned before our measurements will be adversely affected. Consider the situation of lossless oscillation between two states A and B, such as in Eq. 4.2, but detuned off resonance by δ_{RF} .

$$P_A(t) = \frac{\omega_R^2}{\omega_R'^2} \cos^2 \left(\frac{\omega_R' t}{2} \right) \quad (4.24)$$

$$P_B(t) = \frac{\omega_R^2}{\omega_R'^2} \sin^2 \left(\frac{\omega_R' t}{2} \right) \quad (4.25)$$

where $\omega_R'^2 = \omega_R^2 + \delta_{RF}^2$ is the effective Rabi frequency. For times $t \ll 1/\omega_R, 1/\delta_{RF}$ the approximate populations are the same as Eq. 4.4.

$$P_A(t) \approx 1 - (t\omega_R/2)^2 \quad (4.26)$$

$$P_B(t) \approx (t\omega_R/2)^2 \quad (4.27)$$

To see the effects of detuning at short times we must continue the Taylor expansion in time from second order to fourth order, expressing the result as a scaling of the second order approximation.

$$P_B(t) \approx \left(\frac{\omega_R t}{2} \right)^2 \left(1 - \frac{\delta_{RF}^2 t^2}{12} - \frac{\omega_R^2 t^2}{12} \right) \quad (4.28)$$

To consider the effects of detuning on the quadratic short approximation we can compare them with the reduction in population transfer from the fourth order ω_R term, which is always present. In the absence of detuning ($\delta_{RF} = 0$) the short time approximation is reasonable for surprisingly long times, overestimating the transfer from state A to state B by only 9% when $\omega_R t = 1$. Likewise for $\delta_{RF} = \omega_R$ the losses from the fourth order temporal terms are equal. Therefore detunings $\delta_{RF} \ll \omega_R$ should not be of significant concern.

A separate case to consider is when the detuning δ_{RF} is large relative to the Rabi frequency ω_R . This would be the case if we were pushed off resonance by an AC stark shift. In this case detuning will extend the observed lifetime τ_{obs} from the expected lifetime τ_{EP} by

$$\tau_{EP}/\tau_{obs} = 1 - \frac{1}{12} (\delta_{RF} t)^2 \quad (4.29)$$

Change in the lifetime limits $\delta_{RF} < \sim 0.77/t$ for pulsed measurements for variations similar to the $\pm 5\%$ reproducibility level of our machine. For measurement pulses with a period with $\delta_t = 1\text{ms}$, this is $\delta_{RF} < 770\text{Hz}$. From this it is concluded that the pulsed QZE experiments should be very robust against systematic errors in the RF detunings.

The effects of detuning on the continuous case is both more and less complicated. If the measurement probe laser is off resonance it will induce an AC Stark shift proportional to its intensity. As mentioned in the experimental section, we treat this systemically through a separately measurement of the shift.

4.3.3 Clock shift

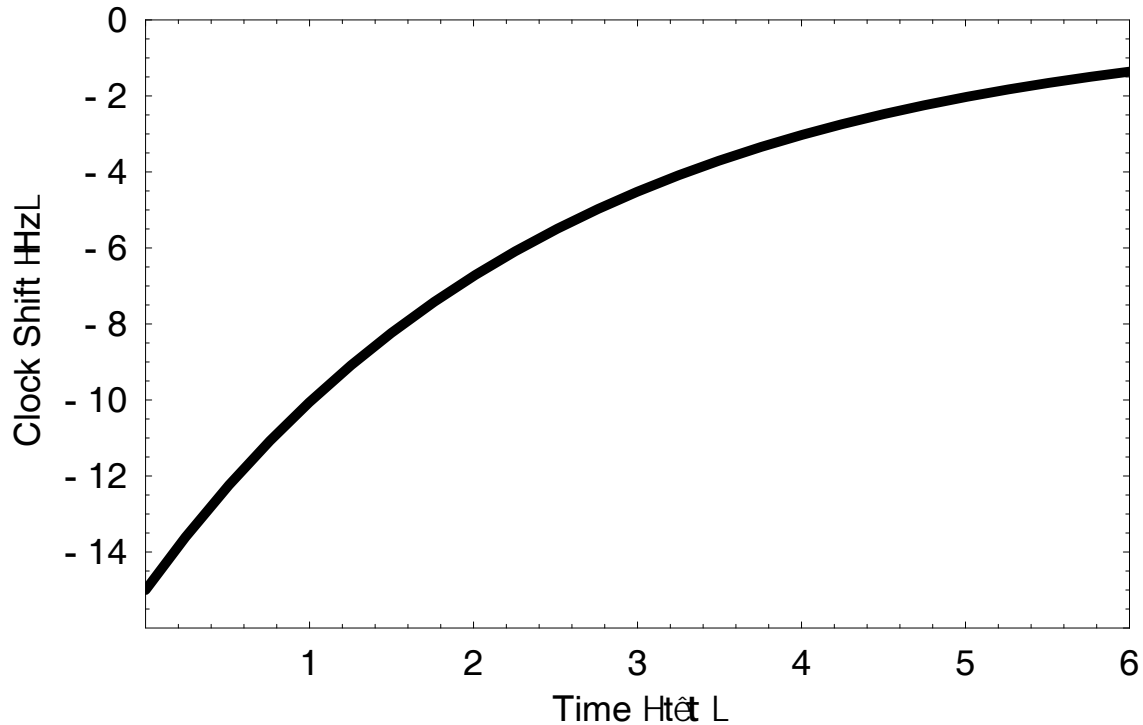


Figure 4-18: Expected change in the clock shift (Hz) for our Zeno experiment BEC, decaying with lifetime τ .

The $|2, +1\rangle$ and $|1, -1\rangle$ states have different scattering lengths. Hence condensates with identical densities have different mean field energies depending on which state they are in. This difference in energies results in a shift in the transition energy between the states which is dependent on the local density, often referred to as the cold collision shift or the clock shift. For small population transfers the clock shift

$$\delta\nu_{12} = -\frac{2\hbar\Delta a_{12}}{m}n \quad (4.30)$$

where Δa_{12} is the difference in scattering lengths between states 1 and 2. In our quantum Zeno experiments the BEC population is dropping in time as $|1, -1\rangle$ atoms that have transferred to $|2, +1\rangle$ are scattered away. This changes the density and hence the clock shift $\delta\nu(t)$ as a function of the condensate lifetime τ .

$$\delta\nu(t) = \delta\nu_0 \exp\left(-\frac{2t}{5\tau}\right) \quad (4.31)$$

Typically the lifetime measurements span a range of times $\sim 2\tau$, which corresponds to a 45% change in the clock shift. For a large BEC $N_c = 5 \times 10^6$ in a {63,63,6.3}Hz trap, the clock shift is $\delta\nu_0 = -97\text{Hz}$, and will change by ~ 45 Hz during a lifetime measurement. This is an amount comparable to the Rabi frequencies used in our experiments. If we instead reduce the atom number by 99% to $N_c = 5 \times 10^4$ the clock shift becomes -15.4 Hz and the change during a lifetime measurement reduces to 7 Hz, which is much smaller than the Rabi frequency.

For our data the most extreme scenarios are for the longest times between pulses. From Eq. 4.28 the fourth order Rabi frequency population correction to the $\delta t=1.2$ ms and $\omega_R/2\pi=54.6$ Hz point is 1.4% and the detuning correction is 0.02%. For the $\delta t=1.9$ ms and $\omega_R=24.7$ Hz point the fourth order population correction is 0.72% and the detuning correction is 0.06%. In neither case is their an appreciable effect.

4.3.4 Polarization

Ideally the electric field vector of the linearly polarized scattering measurement laser light is exactly aligned with the magnetic field vector of the condensate, driving only π optical transitions. Misalignment of the polarization with the magnetic field vector of the atoms in the condensate with the electric field vector of the light will shift intensity from the π transition onto the σ^+ and σ^- transitions. In the 3.0 magnetic bias field these transitions are split by 2.8 MHz, which is smaller than the natural linewidth of 6.06 MHz, but large enough to potentially introduce complications (Fig. 4-4) in the AC stark shift calibration.

We know from previous measurements that our condensate is level with respect to gravity to within less than a degree. Gravitational sag in the magnetic trap will rotate the magnetic field vector in the condensate from horizontal. Since our laser beam is oriented vertically this will mix in $\sigma^+ + \sigma^-$ polarizations in equal amount. With a magnetic bias field of 3.0 Gauss and a vertical trap frequency of 63 Hz Eq. 3.10 from Sec. 3.7.1 gives the angle between the long axis of the condensate and the magnetic field vector of 14° . A multilevel model accounting for all three polarizations showed that the change in the slope of the AC stark shift was less than 1% for this rotation angle. More importantly the linewidth of the transition increases from 6.06 MHz to 8.8 MHz. This explains the broader than expected linewidth observed in Fig. 4-17.

4.3.5 Superradiance

One concern in illuminating the condensate with near or on resonant laser light is the possibility of nonlinear processes such as superradiance [44, 45, 68] modifying the scattering rate or inducing additional losses. As a first precaution against nonlinear effects we worked

far below the saturation intensity. In previous works π polarized light at low intensities scatters photons from a condensate with the distribution expected from a single atom and does not undergo either Raman or Rayleigh superradiance [44, 45, 68]. If superradiant processes are occurring they will exhibit a nonlinear increase in atom losses with time and intensity. Since previous studies were done off resonance a check was done to ensure that superradiance was not occurring when we performed a scattering measurement. Fig. 4-19 shows how increasing the pulse width does not result in substantial additional losses as we would expect for superradiance.

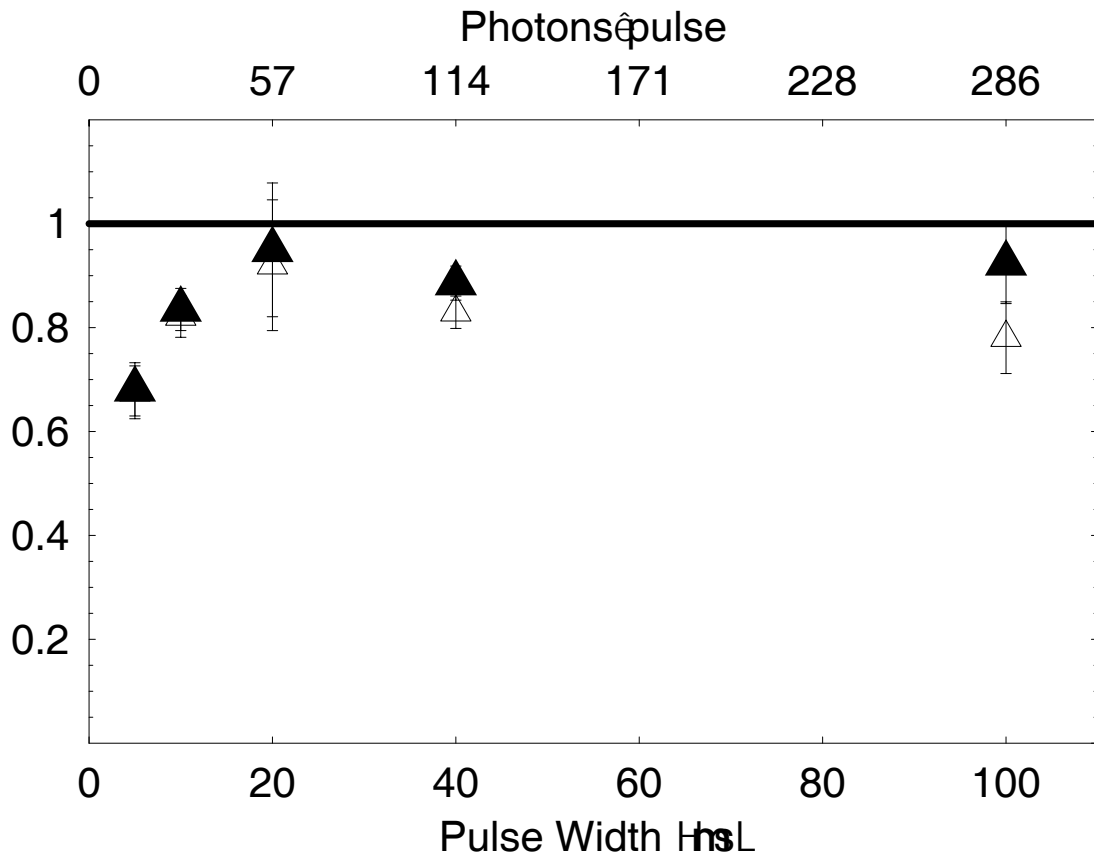


Figure 4-19: Expected pulsed quantum Zeno effect ($\frac{1}{4}\delta t\omega_R^2/\tau_{EP} = 1$) as a function of scattering measurement laser pulse width. Open triangles are corrected for parasitic measurement losses.

4.3.6 Collisions

Collisions between the recoiling atoms which have been measured and the remaining condensate can cause additional losses. To estimate the effects of collisions the scattering cross section and the duration that scattered atoms remain in the trap must be considered. When

the measured atom has absorbed a photon it is in the $5P_{3/2}$ excited state and has a much larger scattering cross section due to the strong allowed dipole interaction with the surrounding $5S_{1/2}$ state atoms. After the atom has relaxed back to the $5S_{1/2}$ ground state by spontaneously emitted a photon it has a much smaller scattering cross section due to the weak induced dipole interaction with the surrounding $5S_{1/2}$ state atoms.

Both the absorption and emission of a 780 nm photon with a ^{87}Rb atom will impart a recoil velocity of 6 mm/s, equivalent to a temperature of $T_r=376$ nK where $\frac{1}{2}k_B T_r = \frac{1}{2}mv_r^2$. While the absorbed photon is always in the direction of the probe laser beam, the spontaneously emitted photon will radiate in a random direction and do not contribute to the average momentum. While this recoil energy is much greater than the chemical potential of the BEC ($\mu=15\text{nK}$) it is much less than the trap depth of $5\mu\text{K}$. To escape from a trap of energy depth U_{trap} requires an average kinetic energy $\frac{1}{2}m(N_{sc}v_r)^2$ from N_{sc} scatterings. Solving for N_{sc} as a function of recoil temperature and trap depth gives

$$N_{sc} = \sqrt{\frac{2U_{trap}}{k_B T_r}} \quad (4.32)$$

For a $5\mu\text{K}$ deep trap this is an average of ~ 5.2 photon scatterings before the atom has sufficient momentum to be ejected from the trap. This is much smaller than the average of 29 photon scatterings which the condensate normally undergoes per discrete measurement pulse. Some deviation may be expected in the infrequent pulse regime because as calculated in Sec. 4.3.1 the optical power can be significantly attenuated when it reaches the far side of the condensate.

Collisional losses can occur when the atoms are escaping from the condensate or if they are retained by the trap and recollide with condensate. In the case of the initially escaping $5S_{1/2}$ state scattered atoms the small number of atoms in the condensate gives it a low collisional opacity of $\sim 5\%$, putting this loss enhancement on par with our shot to shot noise. However this calculation does not account for the greatly increase scattering cross section during the 25 ns a measured atom is in the $5P_{3/2}$ per photon scattering. The potential for the $5S_{1/2} + 5P_{3/2}$ interaction goes as $U = -C_3/r^3$ and the scattering cross section calculated from a semi classical approximation is $\sigma_{SP} = 2\pi^2 \frac{C_3}{\hbar v}$ for an atom with velocity v (p. 525 [113]). The coefficient of this interaction has been calculated to be $C_3 = 10.1e_0^2 a_0^2$ [114]. For an rubidium atom traveling at the recoil velocity $v = v_r \approx 6\text{mm/s}$ the excited state scattering cross section is $\sigma_{SP} = 4.3 \times 10^{-7}\text{cm}^2$, nearly five orders of magnitude larger then the s-wave ($5S_{1/2} + S_{1/2}$) scattering cross section of $7.3 \times 10^{-12}\text{cm}^2$.

The effect of this significantly large scattering cross section is reduced by the low probability of finding the atom in the excited state. For the pulsed experiment with a saturation parameter of $s_0 = 0.15$ this amounts to a factor of 15 reduction and for the continuous experiments with a saturation parameter of $s_0 = 0.001$ a factor of 2000. Both of these would still suggest the overwhelming probability that a measured atom collides with at least one additional atom for each photon it scatters. This does not agree with our observed loss

rates, which show only a 17% increase over the expected loss rate. A possible explanation for the pulsed data is that because we are on resonance the Condon radius at which the rubidium molecule would form is much larger than the size of the condensate, but that would not account for the invariance of the pulsed loss rate to changes in laser detuning.

4.4 Conclusions

We have extended previous work in pulsed QZE measurements [82, 84, 85] by exploiting advantages inherent to trapped ultracold atoms. In ion experiments optical pumping between states during the pulsed laser scattering measurements changed the observed population [82, 84], requiring significant corrections for the $N=32$ and $N=64$ pulse measurements (Table I, [82]). With corrections on $N=64$ data the greatest survival probability observed was $P(64) = 0.943(20)$ or $\tau_{EP}\omega_R = 54(30)$. Unlike scattering photons off tightly trapped ions, the scattering of a single photon off a weakly trapped ultra-cold atom induces a dramatic and easily distinguishable change in momentum. Furthermore, repeated scatterings increase this momentum and enhance rather than degrade the contrast with unmeasured atoms. QZE experiments of an unstable system involving tunneling measurements of cold neutral atoms in an accelerating lattice [85] observed an increase in survival probability from $P=0.6$ to $P=0.8$ with $N=9$ measurements.

Previous demonstrations of the continuous QZE [86–89] observed qualitative, but not quantitatively characterized suppression effects with increasing laser intensity. In a trapped ion system evolving with free Larmor precession in a magnetic field an $\sim 80\%$ reduction in fluorescence with increasing laser intensity (near and above saturation) was observed [87]. A less comparable continuous QZE system is that observed from molecular collisions in nuclear spin isomer polarized $^{13}\text{CH}_3\text{F}$ gas, where a 60% drop in the conversion rate of gas was observed when the pressure was increased by 12 times [86].

The large hyperfine splitting in ^{87}Rb is favorable for QZE type experiments because it reduces the chance of off resonant scattering of the measurement laser by atoms in the $|1, -1\rangle$ state to 2.8×10^{-7} of that for $|2, +1\rangle$ atoms. Substituting a single photon Rabi oscillation on the $F=1, m_F=0 \leftrightarrow F=2, m_F=0$ clock transition [107] in a low density sample could reduce the systematic limitations observed in this paper relating to the observed parasitic measurement related losses and probable collisional losses.

Complications from an optically dense sample were avoided by working in the frequent measurement regime to prevent appreciable buildup of atoms in the measured state. The QZE is closely related to the phenomena of interaction free measurements [99, 100], where information about the state of a system can be determined from the absence rather than presence of a scattering event.

In conclusion we have used a new system to perform quantum Zeno effect measurements deep in the limit of strong suppression. We have measured and quantified the suppression

of evolution due to both the continuous weak measurement and frequent pulsed strong measurement cases. Our observed quantum Zeno suppressions are larger than both previous pulsed [82] and continuous [87] results, and is also greater than that expected from recently proposed experiments [101, 104, 105, 115]. The lifetime of the initial state is equal when $\gamma\delta t = 3.60(0.43)$, in agreement with the predicted value of 4 [111]. Initial state lifetimes were increased by $198(16) 1/\omega_R$ in the pulse regime and $172(20) 1/\omega_R$ in the continuous regime.

Appendix A

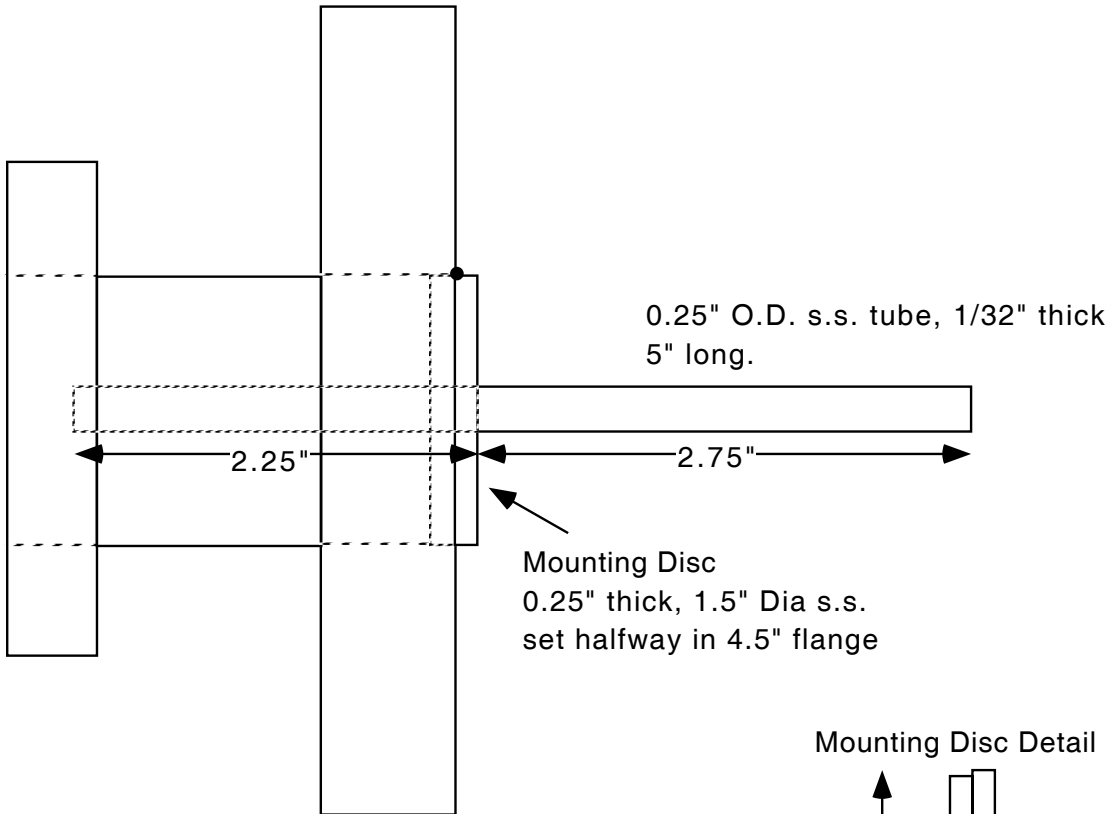
Rubidium Oven Plans

This appendix includes the machine drawings for the BEC IV Rubidium oven. Plans should be used for reference purposes only. Piece #4 was fabricated but not installed. A separate aluminum mount was fabricated and iridium soldered to the cold finger to compensate for a mislabeling of the cold finger length.

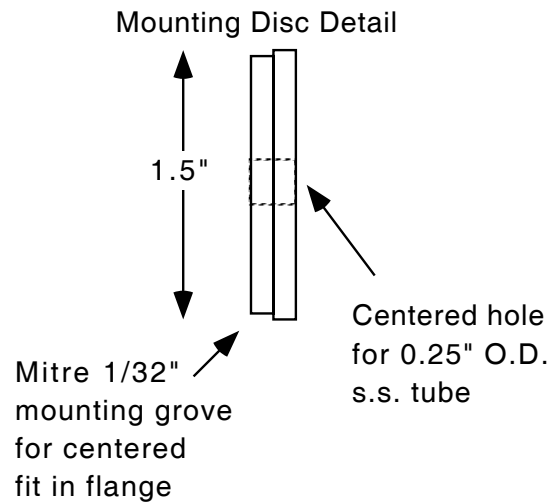
Piece 1: Differential Pumping Tube:
Work on 4.5" Reducing Flange.

Erik Streed
November 29 2000
streed@mit.edu
Ph. 617-452-2501
Rm. 36-272A

All parts 300 series (non magnetic) stainless steel.
Attach mounting disc as best seen fit. Must meet Ultra High Vacuum rating



4.5" to 2.75" s.s. Reducing Flange (provided)
Body tube is 1.5" O.D. 1/32" thick s.s.



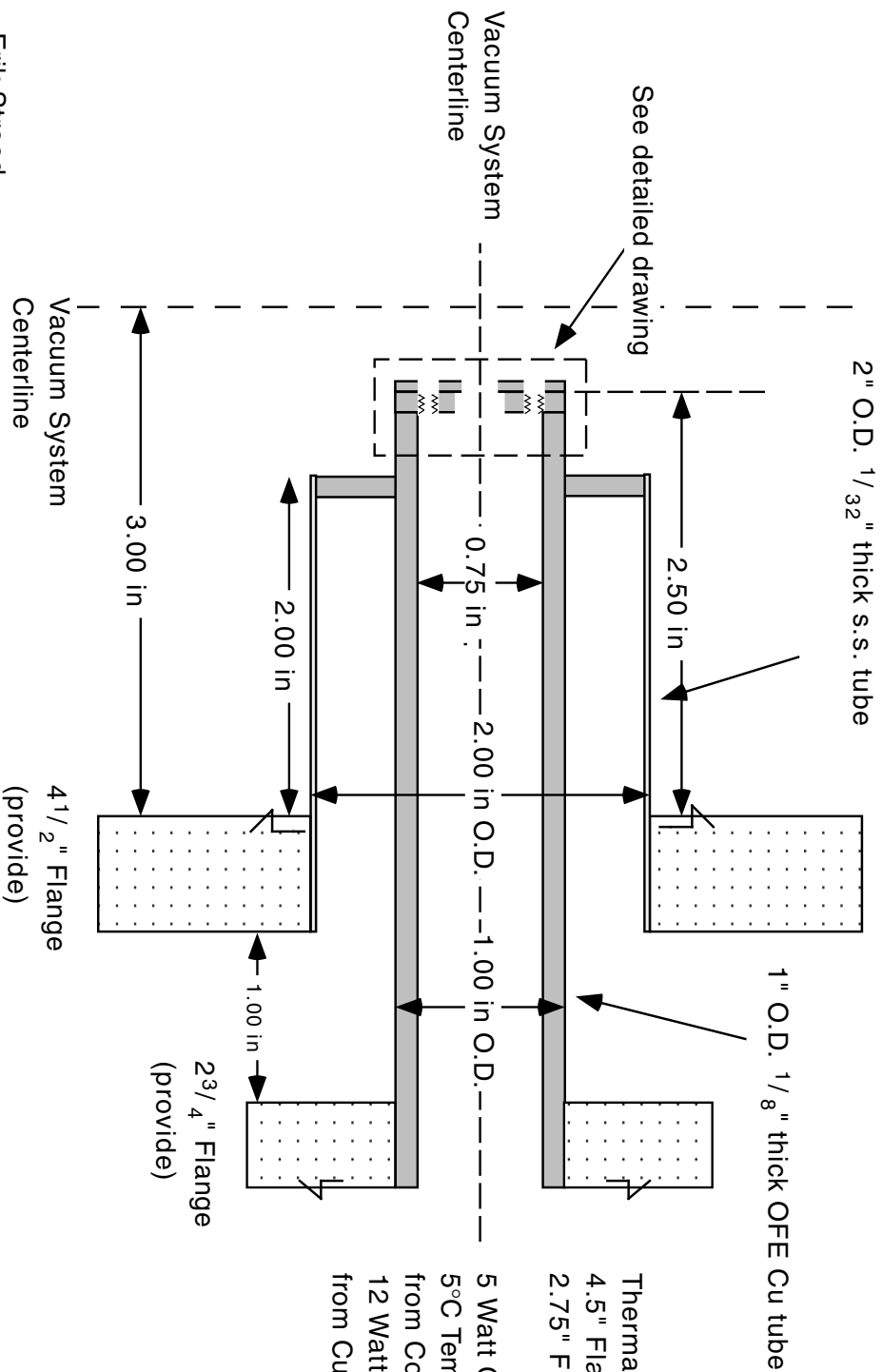
Drawing is to scale: 1"=1"

Piece 2: Rb Oven Nozzle

Work on 4.5" & 2.75" flange.

Please use vacuum grade, oxygen free Copper.

Plate Copper parts with 1 mil Nickel



See detailed drawing

Vacuum System Centerline

Vacuum System Centerline

Erik Streed

December 4, 2000

streed@mit.edu

Ph. 617-452-2501

Rm. 36-272A

Make all connections with methods rated for Ultra High Vacuum.

Thermal Info For

4.5" Flange Temp = 20 °C

2.75" Flange Temp = 150 °C

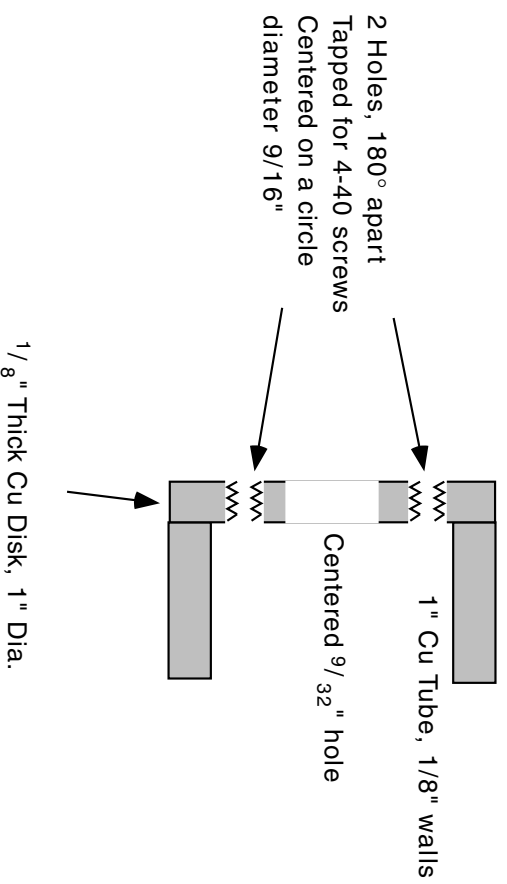
5 Watt Conduction loss

5°C Temp Gradient on Cu tube from Conduction loss

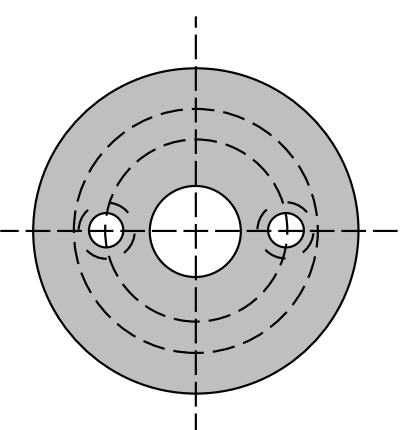
12 Watt B.B. Radition Heating from Cu To S.S. Tube.

Piece 2: Rb Oven Nozzle Detail
All parts OFE Copper
Please plate with 1 mil Nickel.

Side View



Front View



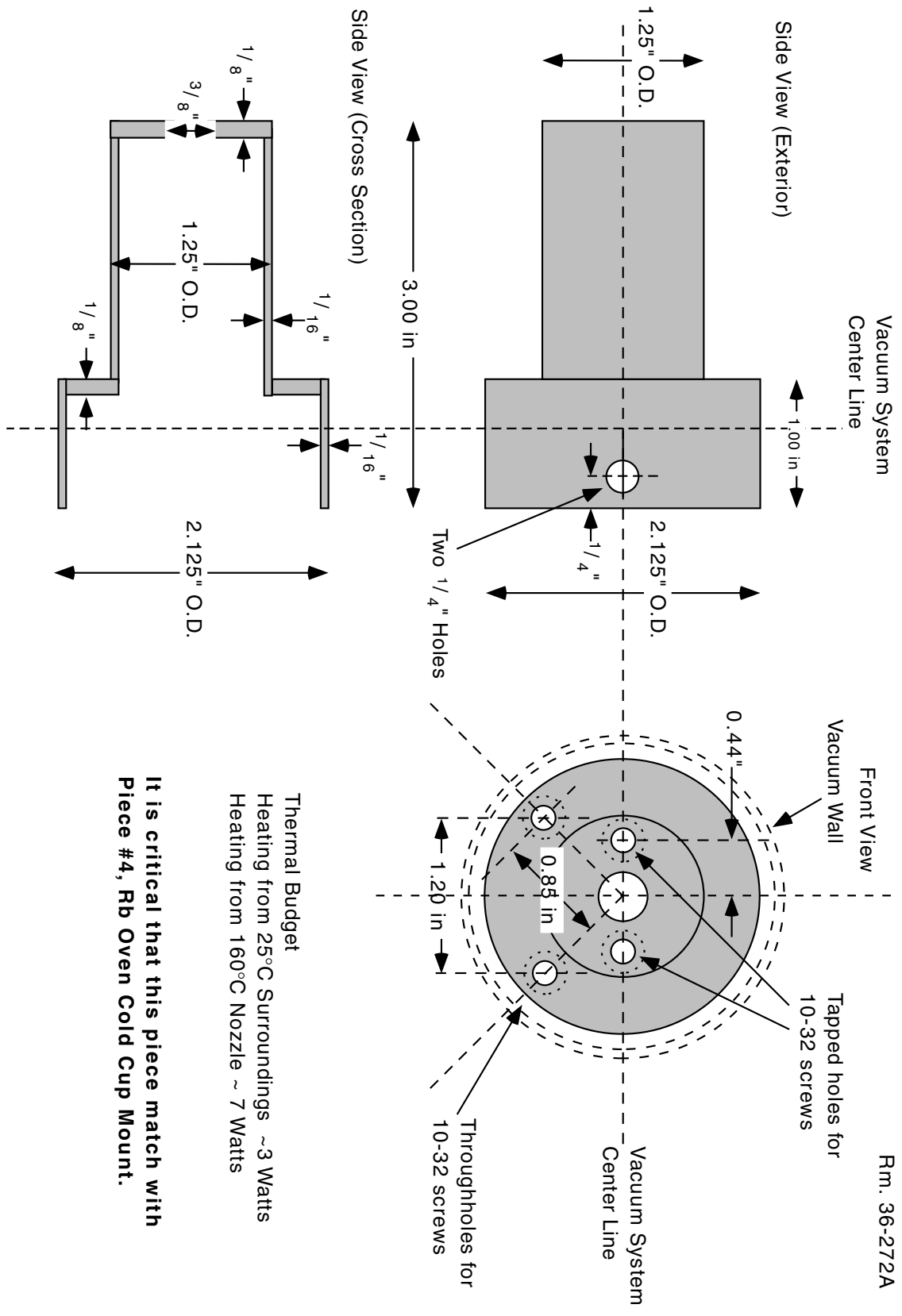
Attach Cu Disk to Cu Tube with methods rated for Ultra High Vacuum..

Erik Streed
December 4, 2000
streed@mit.edu
Ph. 617-452-2501
Rm. 36-272A

Piece 3: Rb Oven Cold Cup.
 Please plate piece with 1 mil. Nickel

OFE Copper

Erik Streed
 Dec 4, 2000
 streed@mit.edu
 Ph. 617-452-2501
 Rm. 36-272A



Thermal Budget:
 Heating from 25°C Surroundings ~ 3 Watts
 Heating from 160°C Nozzle ~ 7 Watts

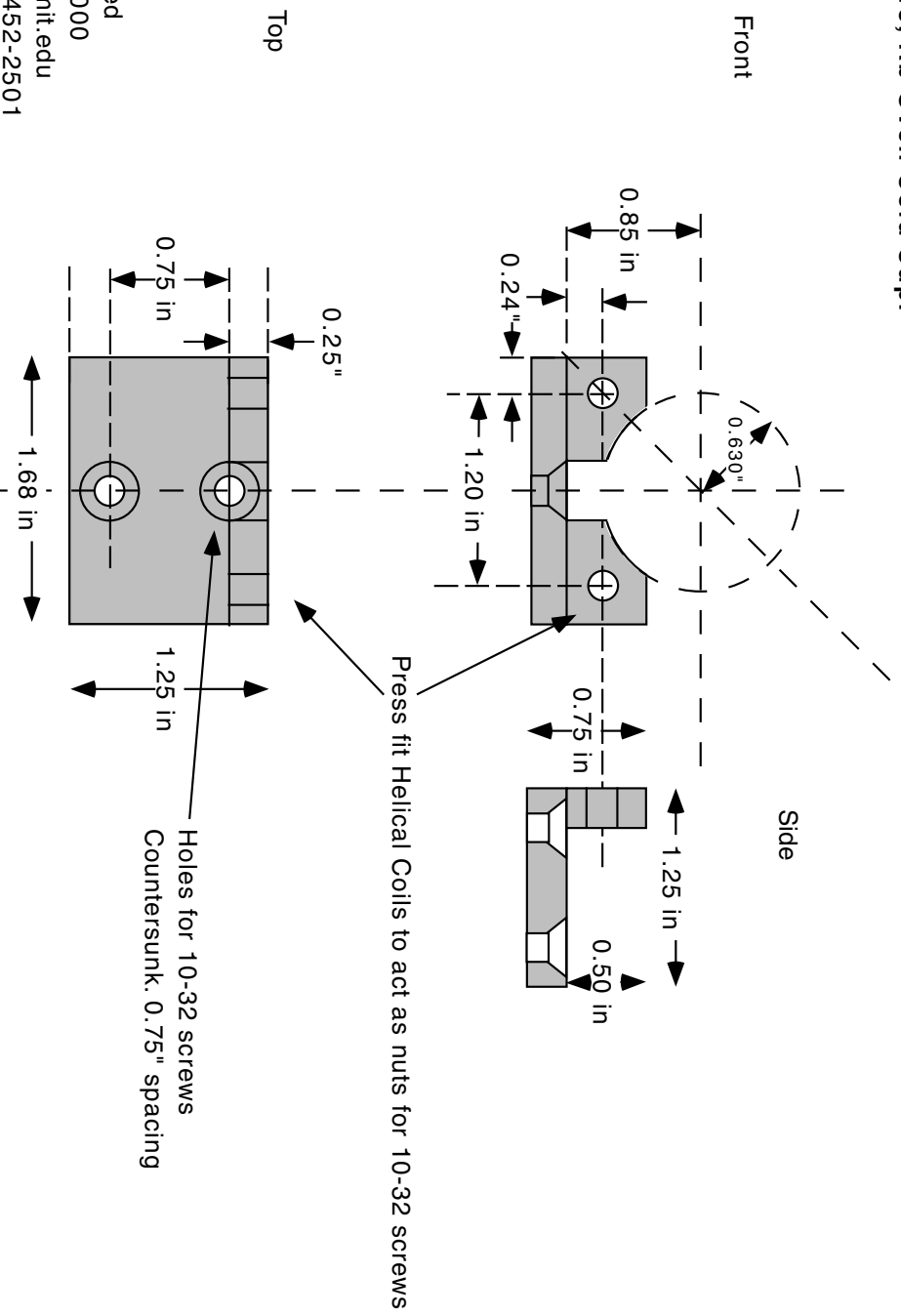
It is critical that this piece match with Piece #4, Rb Oven Cold Cup Mount.

Piece 4: Rb Oven Cold Cup Mount

Please plate Cu parts with 1 mil. Nickel.

 OFE Copper

It is critical that this piece match with Piece #3, Rb Oven Cold Cup.



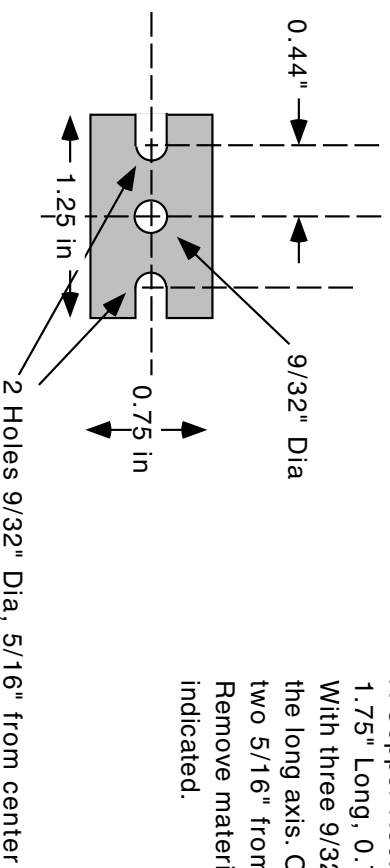
Erik Streed
Dec 4, 2000
street@mit.edu
Ph. 617-452-2501
Rm. 36-272A

Piece 5: Rb Oven Cold Cup Faceplate



OFE Copper

Please plate with 1 mil Nickel.



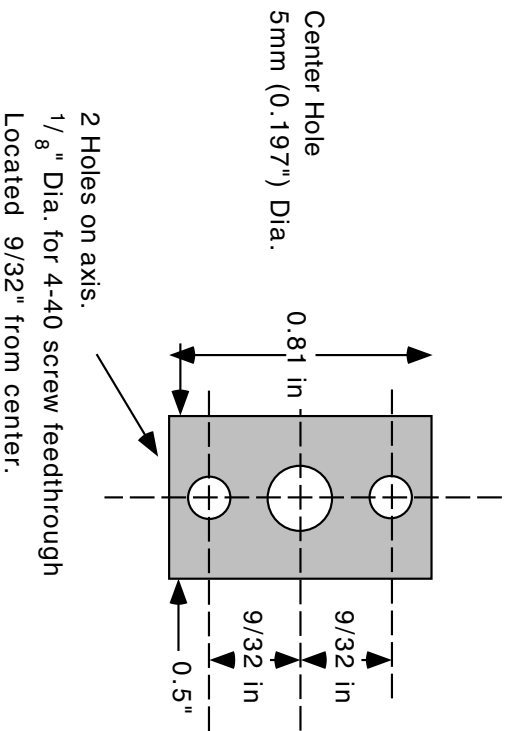
A Copper Rectangle 1/8" Thick,
1.75" Long, 0.75" High.
With three 9/32" Diameter holes along
the long axis. One centered and
two 5/16" from center.
Remove material from outer holes to edge as
indicated.

Component to fit to Piece 3. Rb Oven Cold Cup
with 2 10-32 screws.

Erik Streed
Nov. 6, 2000
streed@mit.edu
Ph. 617-452-2501
Rm. 36-272A

Piece 6: Rb Oven Nozzle Faceplate.
OFE Copper
Please plate with 1 mil Nickel.

Faceplate is a copper rectangle 0.81" x 0.5" x 1/16"
Three holes.
First is 5mm, centered.
Other two are on long axis,
9/32" from center, 1/8" Dia.



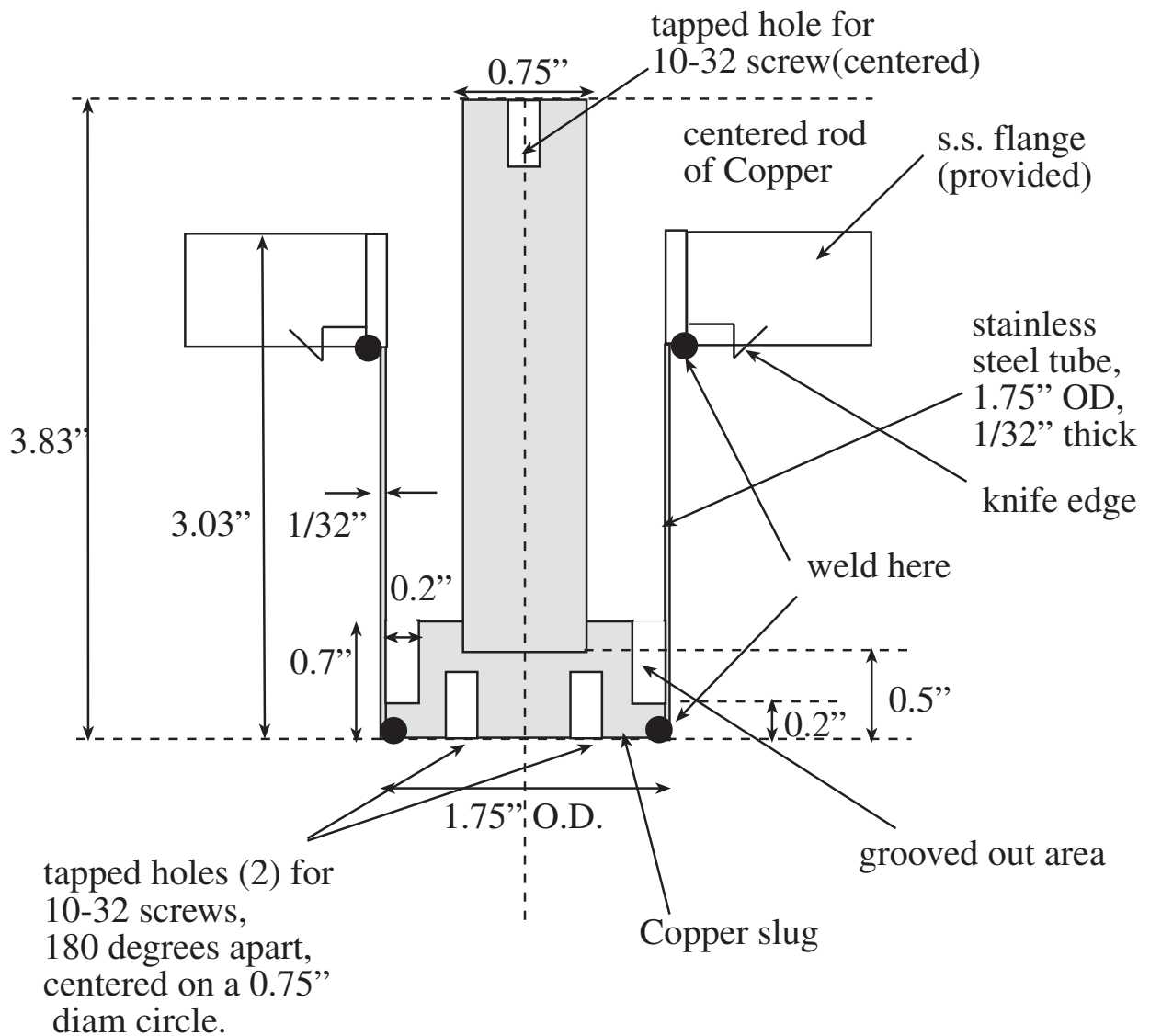
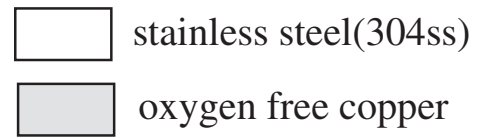
Component to fit adjustably to Piece 2. Rb Oven Nozzle
with 2 4-40 screws.

Erik Streed
November 29, 2000
streed@mit.edu
Ph. 617-452-2501
Rm. 36-272A

Erik Streed
 452-2501
 streed@mit.edu

Work on 4.5" conflange standard 5 mil tolerance required

Please plate Copper parts with 1 mil Nickel.



Appendix B

Publication: Large Atom Number BEC Machines

This appendix contains the Review of Scientific Instruments (RSI) manuscript RSI MS# A050544R “Large Atom Number BEC Machines” [48], describing the construction and characterization of the 3rd and 4th Bose Einstein Condensate machines built at MIT. This manuscript was accepted for publication by RSI on December 13, 2005.

Large atom number Bose-Einstein Condensate machines

Erik W Streed¹, Ananth P Chikkatur², Todd L Gustavson³, Micah Boyd¹, Yoshio Torii⁴, Dominik Schneble⁵, Gretchen K Campbell¹, David E Pritchard¹, Wolfgang Ketterle¹

¹ MIT-Harvard Center for Ultracold Atoms, Research Laboratory of Electronics and Department of Physics, Massachusetts Institute of Technology, Cambridge, MA 02139, USA

² Belfer Center for Science and International Affairs, Littauer P-14, 79 JFK St., Harvard University, Cambridge, MA 02138 USA

³ Hansen Experimental Physics Laboratory End Station 3, Rm. M302, Department of Physics, Stanford University, Stanford, California, 94305 USA

⁴ Institute of Physics, University of Tokyo, 3-8-1, Meguro-ku, Komaba, Tokyo 153-8902, Japan

⁵ Physics A-106, Department of Physics and Astronomy, SUNY Stony Brook, Stony Brook, New York 11794, USA

(Dated: November 18, 2005)

We describe experimental setups for producing large Bose-Einstein condensates of ²³Na and ⁸⁷Rb. In both, a high flux thermal atomic beam is decelerated by a Zeeman slower and is then captured and cooled in a magneto-optical trap. The atoms are then transferred into a cloverleaf style Ioffe-Pritchard magnetic trap and cooled to quantum degeneracy with radio frequency induced forced evaporation. Typical condensates contain 20 million atoms. We discuss the similarities and differences between the techniques used for producing large ⁸⁷Rb and ²³Na condensates in the context of nearly identical setups.

PACS numbers: 03.75.Hh, 39.10.+j, 39.25.+k, 07.30.-t

I. INTRODUCTION

It has been a decade since Bose Einstein condensation (BEC) in atomic vapors was first observed [1, 2]. The transition from a classical thermal gas to a quantum degenerate Bose-Einstein condensate occurs when the phase space density, $\rho = n\lambda_{dB}^3$ is increased to ~ 1 , where n is the number density and λ_{dB} is the thermal de Broglie wavelength of the atoms. So in principle, getting a BEC is easy: you simply cool down the gas until the critical phase space density is reached. In practice, the procedure is more complicated. A variety of different techniques are used to increase the phase space density in several stages (Table I). Furthermore, each atom has different properties and requires modifications to the cooling techniques. Major work by many groups around the world has now extended these cooling techniques to an impressive number of atomic species: ⁸⁷Rb [3], ²³Na [4], ⁷Li [5, 6], ¹H [7], ⁸⁵Rb [8], ⁴He* [9, 10], ⁴¹K [11], ¹³³Cs [12], ¹⁷⁴Yb [13], and ⁵²Cr [14]. Still, ²³Na and ⁸⁷Rb are the two atoms with the most favorable properties for laser and evaporative cooling and are used most frequently.

A distinguishing characteristic of most experiments is the method in which atoms are laser cooled and then loaded into a magnetic or optical trap for evaporative cooling. Our approach at MIT employs atomic ovens and Zeeman slowing. Other approaches use variations of a vapor cell magneto-optical trap (MOT), in a double MOT configuration, surface MOT [15], or as a source of low velocity atoms [16, 17]. An important figure of merit of a BEC experiment is the number of atoms in the condensate. Large atom number allows better signal-to-noise ratios, greater tolerance against misalignments, and greater robustness in day-to-day operation. Since 1996, the MIT sodium BEC setups have featured the largest alkali condensates. Our three setups routinely produce condensates with atom numbers between 20 and 100 million.

Stage	n (/cm ³)	Temperature	Velocity ^a	ρ
Oven	10^{13}	383K	334 m/s	10^{-14}
Thermal Beam	10^7	n/a	334 m/s	10^{-20}
Slowed Beam	10^7	n/a	43 m/s	10^{-18}
Loading MOT ^b	10^{10}	150 μ K	210 mm/s	10^{-7}
Compressed MOT ^b	10^{11}	300 μ K	300 mm/s	4×10^{-7}
Molasses ^b	10^{11}	10 μ K	54 mm/s	6×10^{-5}
Magnetic trap	10^{11}	500 μ K	380 mm/s	2×10^{-7}
BEC Transition	3×10^{13}	500 nK	12 mm/s	2.61
Pure BEC	10^{14}	(250 nK ^c)	8.5 mm/s	(100)

TABLE I: Typical phase space densities (ρ) during BEC production. Numbers given are for the ⁸⁷Rb apparatus.

^amost probable

^bTypical values, not measured separately

^cChemical potential

Since the diode lasers used to cool rubidium are less expensive than the dye lasers needed for sodium, most new groups have chosen to work with rubidium. The majority of rubidium experiments use vapor cell MOTs, however the typical sizes of the condensates created with vapor cells MOTs are smaller than those realized with a Zeeman slower. The construction of vapor cell MOT rubidium condensate machines is extensively detailed in the complementary work of Ref. [18].

When the Center for Ultracold Atoms was created at MIT and Harvard, a major goal for the Center was to create ⁸⁷Rb condensates with large atom number using the techniques developed for ²³Na condensates. The successful accomplishment of that goal is described in this paper. Furthermore, we are able to discuss similarities and differences between the cooling techniques used for ⁸⁷Rb and ²³Na in the context of nearly identical systems. Our conclusion is that Zeeman slow-

ing of an atomic beam works as well for ^{87}Rb as for ^{23}Na . The added length and therefore overall size of the vacuum apparatus may seem daunting, however in our experience, the Zeeman slowing has proven to be a simple and reliable way to generate an intense slow beam. We present the technical details of how to build a large atom number Bose-Einstein condensate experiment with an intense Zeeman slowed source for either atomic species.

These most recent, third-generation, sodium and rubidium experiments at MIT were both designed with an additional vacuum chamber (“science chamber”) into which cold atoms can be moved using optical tweezers. The multi-chamber design allows us to rapidly reconfigure the experimental setup in the science chambers while keeping the BEC production chamber under vacuum. This has allowed us to perform very different experiments in rapid succession [19–30].

II. SYSTEM OVERVIEW

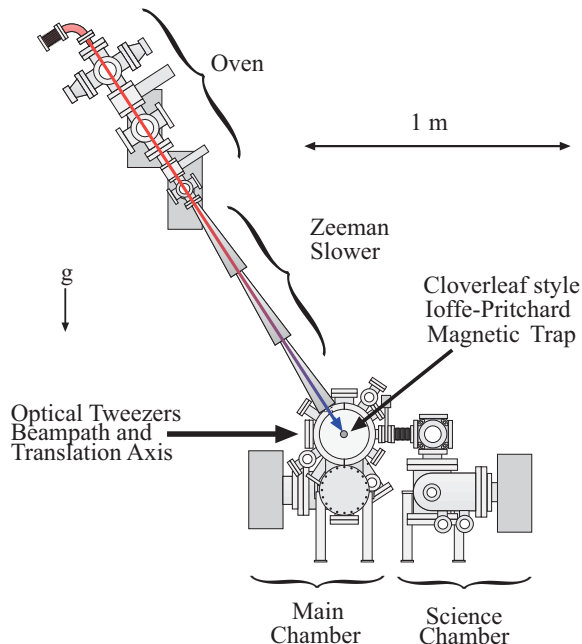


FIG. 1: Vacuum system diagram and major subsystems. ^{87}Rb apparatus shown.

Fig. 1 illustrates the layout of our system. A thermal atomic beam emanates from the oven and is decelerated with the Zeeman slower. In the main chamber, the slowed atoms are captured and cooled with a six-beam magneto-optical trap (MOT) [31]. Before loading the Ioffe-Pritchard magnetic trap, the atoms are optically pumped into the $F=1$ hyperfine ground state. Atoms in the $F=1$, $m_F=-1$ state are weak magnetic field

seeking and are retained by their attraction to the field minimum in the center of the magnetic trap.

The trapped atoms are evaporatively cooled by removing hotter atoms through radio frequency (RF) induced transitions to untrapped states. Reducing the RF frequency lowers the effective depth of the magnetic trap, allowing us to progressively cool to higher densities and lower temperatures until the atoms reach BEC. Magnetically trapped atoms in the $F=2$, $m_F=+2$ state have also been evaporated to BEC.

Ultracold atoms can be transported from the main chamber into the science chamber by loading the atoms into the focus of an optical tweezer and then translating the focus. In this manner we have transported ^{23}Na BECs [19]. Vibrational heating during transport cited in [19] was reduced by the use of Aerotech ABL2000 series air bearing translation stages. Technical problems related to the greater mass and higher three body recombination rate in ^{87}Rb were overcome by transporting ultracold atoms just above the transition temperature T_c , and then evaporating to BEC at the destination. The oven and Zeeman slower are tilted by 57° from horizontal to allow a horizontal orientation for the weak trapping axes of both the optical tweezers and magnetic trap.

Trapping ultracold atoms requires that they be isolated from the surrounding environment. The laser and magnetic trapping techniques confine the atoms in the center of the chamber, out of contact with the room temperature chamber walls. The atoms are still exposed to thermal black body radiation, but are transparent to most of the spectrum. The transitions to which the black body radiation can couple are the optical transitions used for laser cooling and the microwave hyperfine transitions. For optical transitions, which have energies much greater than $k_B T$, the excitation rate is $\frac{3}{\tau_{opt}} \exp(-\hbar\omega_{opt}/k_B T)$, where ω_{opt} is the frequency of the transition and τ_{opt} is the lifetime of the excited state. For rubidium in a 25°C chamber this gives a characteristic excitation lifetime of $\sim 10^{11}$ years. Raising the chamber temperature to 680°C increases the optical excitation rate into the experimentally relevant domain of once per minute. The hyperfine transitions are significantly lower in energy compared to $k_B T$ and have an excitation rate of $\frac{3}{\tau_{hfs}} \frac{k_B T}{\hbar\omega_{hfs}}$, which is once per year at 25°C in ^{87}Rb . Neither of these excitation rates are limitations on current experiments.

Collisions with background gas molecules result in loss from the trap, necessitating low vacuum pressure for long atom cloud lifetime. We can magnetically trap ultracold atomic clouds with lifetimes of several minutes in the $< 10^{-11}$ torr ultrahigh vacuum (UHV) environment of the main production chamber. To achieve this vacuum performance we have followed the general guidelines set out in Ref. [32] for constructing vacuum systems. The main chamber body was constructed of nonmagnetic 304 stainless steel and then electropolished to reduce the surface roughness. The only component placed inside the chamber was the RF evaporation antenna coil (Fig. 2).

The cloverleaf-style Ioffe-Pritchard magnetic trap coils fit inside two re-entrant bucket windows [33], allowing them to be outside the chamber with an inter coil spacing of 25 mm (Fig. 2). The Zeeman slower tube is mounted between the

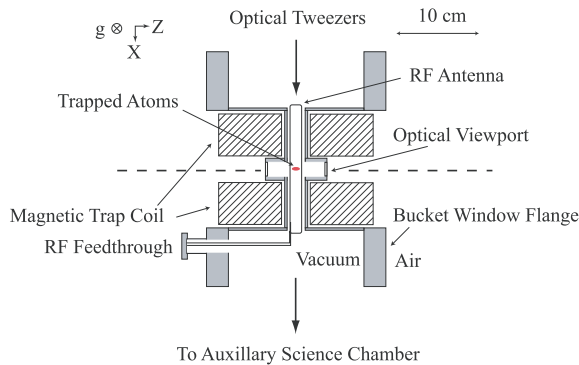


FIG. 2: Main chamber cross section showing re-entrant bucket windows, magnetic trap coils, and RF antenna. View from above.

main chamber and the oven chamber. The Zeeman slower coils surrounding the Zeeman slower tube are also outside of the vacuum system, but cannot be removed without breaking vacuum.

After assembling the chamber, we pumped out the system and reached UHV conditions by heating the system to accelerate outgassing. We heated the main chamber to 230°C and the Zeeman slower to 170°C (limited by the coil epoxy). Using a residual gas analyzer to monitor the main chamber, we “baked” until the partial pressure of hydrogen was reduced to less than 10^{-7} torr and was at least ten times greater than the partial pressure of other gases. A typical bakeout lasted between 3 and 9 days, with temperature changes limited to less than 25°C/hour. While we acknowledge the merit of using dry pumps as recommended in Ref. [18], we use oil sealed rotary vane roughing pumps to back our turbo pumps. The vacuum in the main chamber is preserved after bakeout with a 75 L/s ion pump and a titanium sublimation pump. Refer to Sec. 3.4 of Ref. [34] for more details of our bakeout procedures.

III. OVEN

We generate large fluxes of thermal atoms for Zeeman slowing from effusive atomic beam ovens. An effusive beam is created by atoms escaping through a small hole in a heated chamber [35]. The higher vapor pressure of rubidium requires a more complicated design, but lower operating temperature (110-150°C Rb, 260-350°C Na.) At room temperature, the vapor pressure of sodium ($\approx 3 \times 10^{-11}$ torr [36]) is compatible with our UHV main chamber environment, while that of rubidium ($\approx 4 \times 10^{-7}$ torr [37]) is not. This dictated that the design of the rubidium oven prevent the contamination of the main chamber with rubidium. Because of its greater complexity, further discussion will focus on the rubidium oven (Fig. 3). We expect that the rubidium oven design would also work for sodium, but instead we used a simpler design for sodium as described in Ref. [34].

A combination of active pumping and passive geometrical techniques were used to reduce extraneous rubidium transfer

to the main chamber. A cold cup (I) is used to reduce rubidium vapor in the oven chamber by almost completely surrounding the oven aperture (J) with a cold surface at -25°C. After bake-out, the combination of cold cup and oven chamber ion pump has achieved pressures as low as $\sim 10^{-9}$ torr, although we have successfully made BECs with pressures of up to $\sim 10^{-6}$ torr in this region. The combination of a differential pumping tube, an ion pump, and the Zeeman slower tube provides a pressure differential of over 3 orders of magnitude between the oven and main chamber. This is sufficient to isolate the UHV environment from an oven pressure dominated by rubidium vapor at room temperature. When the oven is opened to replace rubidium and clean the cold cup, the main chamber vacuum is isolated with a pneumatic gate valve. A second gate valve can be used in case of failure of the first. While not used in our system, designers may want to consider gate valves with an embedded window available from VAT to allow optical access along the Zeeman slower or tweezer beam lines during servicing.

The oven is loaded with a sealed glass ampoule containing 5 g of rubidium in an argon atmosphere. To add rubidium, the ampoule is cleaned, placed in the oven, and baked out under vacuum while still sealed. We then break the ampoule under vacuum and heat the oven to 110°C to produce the atomic beam. During operation, the machine is run as a sealed system, without the turbo-mechanical pump, to prevent accidental loss of the main chamber vacuum. Oven temperatures from 150°C down to 110°C produce similar sized ^{87}Rb BECs. Reducing the oven temperature increases the time between rubidium changes to greater than 1000 hrs of operating time. This long operating cycle precluded the need for more complex recycling oven designs [38].

IV. ZEEMAN SLOWER

The atomic beams are slowed from thermal velocities by nearly an order of magnitude by scattering photons from a resonant, counter-propagating laser beam. When a photon with momentum $\hbar k$ ($k = 2\pi/\lambda$) is absorbed or emitted by an atom with mass m , the atom will recoil with a velocity change of $v_r = \hbar k/m$ to conserve momentum. Atoms can resonantly scatter photons up to a maximum rate of $\Gamma/2$, where $1/\Gamma = \tau$ is the excited-state lifetime. This results in a maximum acceleration $a_{max} = \frac{\hbar k \Gamma}{2m}$ ($1.1 \times 10^5 \text{ m/s}^2$ Rb, $9.3 \times 10^5 \text{ m/s}^2$ Na). As the atoms decelerate, the reduced Doppler shift is compensated by tuning the Zeeman shift with a magnetic field [39] to keep the optical transition on resonance. We designed our slowers to decelerate the atoms at a reduced rate $f a_{max}$ where $f \sim 50\%$ is a safety factor to allow for magnetic field imperfections and finite laser intensity.

Our slowers are designed along the lines of Ref. [40], with an increasing magnetic field and σ^- polarized light scattering off the $F=2, m_F=-2 \rightarrow F'=3, m_{F'}=-3$ cycling transition. Before the slowing begins, the atoms are optically pumped into the $F=2, m_F=-2$ state. The large magnetic field at the end of the slower corresponds to a large detuning from the low velocity, low magnetic field resonance frequency. This large detun-

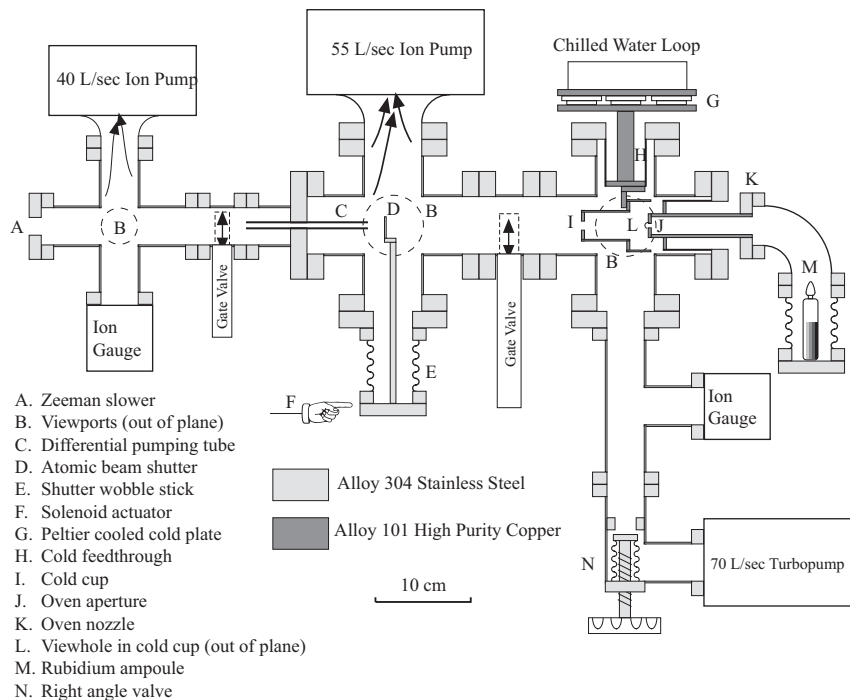


FIG. 3: Effusive rubidium beam oven. Rubidium metal (M) is heated to between 110°C and 150°C , creating a $p_{\text{Rb}} \sim 0.5$ millitorr vapor which escapes through a 5 mm diameter hole (J). A 7.1mm diameter hole in the cold cup (I), 70 mm from the nozzle, allows 0.3% of the emitted flux to pass through, forming an atomic beam with a flux of $\sim 10^{11}$ atoms/s. The remainder is mostly (99.3%) captured on the -30°C , $p_{\text{Rb}} \approx 2.5 \times 10^{-10}$ torr, surface of the Peltier cooled cold cup. We chop this beam with a paddle (D) into a flexible bellows (E). The differential pumping tube (C) and Zeeman slower tube (A) consecutively provide 170x and 620x of pressure reduction between the oven and main chambers.

ing allows the slowing light to pass through the MOT without distorting it due to radiation pressure. Within the slower coils, the quantization axis is well-defined by the longitudinal magnetic field and optical pumping out of the cycling transition is strongly suppressed by the combination of light polarization and Zeeman splitting.

We slow ^{87}Rb atoms from an initial velocity of ~ 350 m/s with a tailored 271 G change in the magnetic field (Fig. 4). An additional uniform ~ 200 G bias field was applied along the length of the slower to ensure that neighboring hyperfine levels were not near resonance in either the slower or the MOT. The slower cycling transition light is detuned -687 MHz from the $F=2 \rightarrow F'=3$ transition. The slowing laser intensity is $I/I_{\text{sat}} \approx 8$, giving a maximum theoretical deceleration of 89% of a_{max} . To maximize the number of atoms in the slowed $F=2, m_F=-2$ state “Slower repumping” light copropagates with the cycling transition light and is detuned -420 MHz from the $F=1 \rightarrow F'=1$ transition to match the Doppler shift of the unslowed thermal atoms from the oven. A flux of $\sim 10^{11}$ ^{87}Rb atoms/s with a peak velocity of 43 m/s was measured from our slower with an oven temperature of 150°C . This is significantly greater flux than the 8×10^8 Rb/sec vapor cell loading rate quoted by [18]. Higher flux (3.2×10^{12} Rb/s) can be achieved with additional complexity, as demonstrated in [41].

The higher temperature of the sodium oven, along with the atoms’ lower mass, results in a greater initial velocity of

800 – 950 m/s. This requires a slower with a much larger magnetic field change of 1150 Gauss. To reduce the maximum magnitude of the magnetic fields we use the “spin flip” variant of the increasing field design by shifting the zero crossing of the magnetic field from the beginning of the slower to the middle. The first segment then becomes a decreasing field slower, with current flowing in the opposite direction of the second, increasing field segment. In the low magnetic field region between the two segments the slowing light flips from cycling on the $F=2, m_F=+2$ ($m_I=+3/2, m_J=+1/2$ at high field) $\rightarrow F'=3, m_{F'}=+3$ ($m_I=+3/2, m_J=+3/2$) transition with σ^+ polarization to the $F=2, m_F=-2$ ($m_I=-3/2, m_J=-1/2$) $\rightarrow F'=3, m_{F'}=-3$ ($m_I=-3/2, m_J=-3/2$) transition with σ^- polarization. Similar to the rubidium slower, optical repumping light, resonant with the $F=1 \rightarrow F'=2$ transition, is introduced to prepare atoms in the $F=2, m_F=+2$ state before slowing. In addition the repumping light protects against optical pumping into the $F=1$ manifold which may occur in the low magnetic field region between the coils because of the small excited state hyperfine splitting (Fig.6). Experimentally, the absence of repumping light significantly degrades slower performance (Fig 1-13, [34]).

The sodium slowing beam is detuned 1.0 GHz below the $F=2 \rightarrow F'=3$ transition and has an intensity of $I/I_{\text{sat}} \approx 4$, giving a laser power limited maximum deceleration of 80% of a_{max} . Unlike the rubidium slower, light for optical pumping

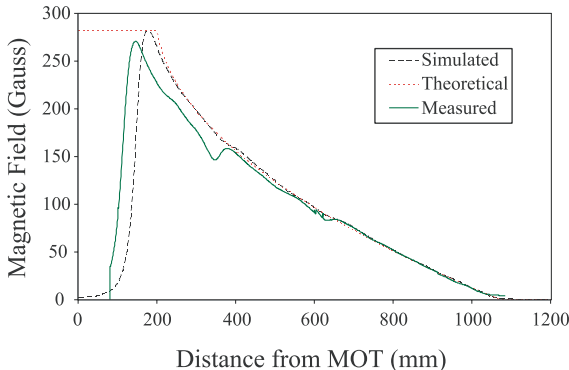


FIG. 4: Magnetic field profile of the rubidium Zeeman slower, not including uniform bias field. The theoretical line shows the desired magnetic field profile for atoms decelerated from 330 m/s to 20 m/s at 60% of the maximum intensity limited deceleration ($f=53\%$ of a_{max} .) The simulated line depicts the expected field from slower coils with the winding pattern in Fig. 11 of Appendix B. The prominent bumps shown above in the measured field were subsequently smoothed with additional current carrying loops.

is generated by adding 1.75 GHz sidebands to the slowing light using an electro-optical modulator. The sodium slower coils were broken up such that the first segment had an initial field of 440 G and a length of 52 cm and the second segment had a final field of 710 G and a length of 43 cm. The sodium slower was tested as depicted in Fig. 5, with a measured flux of 3×10^{11} ^{23}Na atoms/s with a peak velocity of 100 m/s.

V. LASERS

Resonant laser light is used to slow, cool, trap, and detect the atoms. All laser light is prepared on a separate optics table and delivered to the apparatus (Fig. 1) through single-mode optical fibers. Because stray resonant light can heat the atoms during evaporation, black cloth separates the two tables. All frequency shifting and attenuation of the light is done with acousto-optic modulators. Mechanical shutters are also placed in front of each fiber coupler to block any light which might leak through the modulators and disturb the atoms. Atomic energy levels and laser frequencies used are indicated in Fig. 6.

We use different techniques for generating laser light at the resonant wavelengths of ^{87}Rb (780 nm) and ^{23}Na (589 nm). For ^{87}Rb we use a Toptica DL100 external cavity diode laser and TA100 semiconductor tapered amplifier to create 350 mW and 35 mW of light resonant with the ^{87}Rb $F=2 \rightarrow F'=3$ and $F=1 \rightarrow F'=1$ transitions at 780 nm. The lasers are stabilized with a polarization sensitive saturated absorption spectroscopy lock [42, 43]. This modulation-free technique optically creates a derivative signal of the absorption spectra that is locked with a proportional+integral gain servo loop.

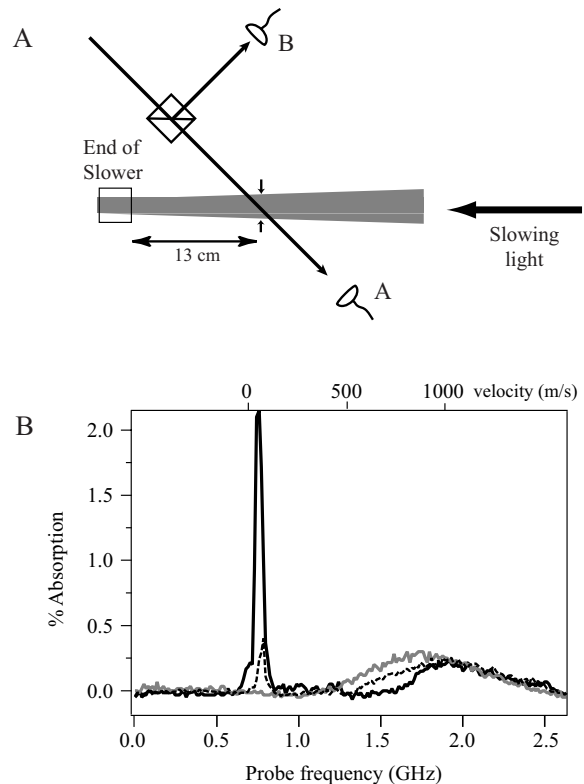


FIG. 5: Sodium slower performance. A. Schematic of the differential absorption measurement of the slowed atomic beam. The slowed atomic beam is shown in gray. The photodiode signals A & B are subtracted and amplified. B. Typical absorption signal for ^{23}Na beam at 45° probe angle. The black solid line is the slowed beam with both slower solenoids fully energized. The dashed line is with only the increasing field slower solenoid, and the gray line is the raw atomic beam without any slowing. The top scale converts the probe frequency into a velocity scale relative to the $F = 2$ cycling transition.

The locking signal fluctuation indicates a frequency jitter of $< 1\text{MHz}$ over several seconds, which is much less than the 6.1 MHz natural linewidth of ^{87}Rb . The large frequency shifts used for the slower cycling and repumping light reduced the available power to a few mW. Each of these beams is amplified to 35-40 mW by injection locking [44] a free running Sanyo DL7140-201 laser diode before combining the beams on a non polarizing beamsplitter and coupling into a fiber.

The ^{87}Rb MOT uses a total of 60 mW of light near the $F=2 \rightarrow F'=3$ cycling transition for trapping/cooling. The $F=2 \rightarrow F'=3$ transition in the MOT is only approximately a closed cycle and atoms are often optically pumped into the $F=1$ ground state. To repump these atoms back into the $F=2$ state we use 10 mW of light on the $F=1 \rightarrow F'=1$ transition. In addition, to transfer atoms from the $F=2$ to $F=1$ manifold, such as prior to loading them into the magnetic trap, we introduce a few mW of “depumping” light resonant with the $F=2 \rightarrow F'=2$ transition. Zeeman slowing uses 18 mW of slower cycling light and 6 mW of slower repumping light. All powers

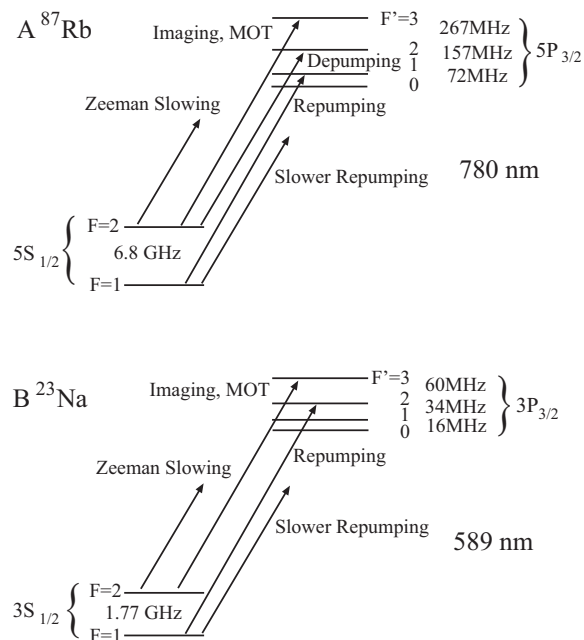


FIG. 6: Simplified level structure of ^{87}Rb (A) and ^{23}Na (B) with relevant transitions, hyperfine splittings, and laser frequencies.

are quoted after fiber coupling, measured as delivered to the apparatus table.

For ^{23}Na we use a Coherent 899 dye laser pumped by a Spectra Physics Millennia laser (532 nm, 8.5 W). Typically 1.2 W of 589 nm light is generated by the dye laser. The laser frequency was referenced to an external saturation-absorption lock-in scheme and locked to a Fabry-Perot cavity. Stable operation was improved by using a precision dye nozzle (Radiant Dyes, Germany), high pressure dye circulator at 12 bar, and stabilized temperatures for the room and dye.

For more detailed information on the generation of the laser light for sodium MOTs, see Sec. 3.4 of Ref. [45]. Typical delivered laser powers are 80 mW for the MOT light, 20 mW for the repumping light, 40 mW for the slowing light and less than one mW for the imaging beam. Electro-optic modulators allow the addition of high frequency sidebands (~ 1.8 GHz) on the slowing and MOT light for repumping without the use of an additional laser beam. Recent advances in single frequency high power fiber and diode pumped solid state lasers [46] have made nonlinear techniques such as sum frequency generation [47, 48] and frequency doubling [49] interesting alternatives as resonant light sources.

VI. MAGNETO OPTICAL TRAP

The MOT [31] is the workhorse of atomic physics for creating large samples of ultracold atoms. We use a six-beam configuration, which doubles as an optical molasses when the

magnetic gradient field is off. Similar to Ref. [18] the ^{87}Rb apparatus uses a bright MOT. The ^{87}Rb MOT equilibrates to around 4×10^{10} atoms after ~ 2 s of loading, operating in a magnetic field gradient of 16.5 G/cm with cycling beams detuned -18 MHz from the $F=2 \rightarrow F'=3$ transition and a peak intensity 5.3 mW/cm 2 . To increase the efficiency of the transfer into the magnetic trap, we briefly compress the ^{87}Rb MOT and then switch off the magnetic field gradient to cool the atoms with optical molasses. The ^{87}Rb MOT is compressed by linearly ramping the gradient to 71 G/cm in 200 ms and simultaneously sweeping the detuning to -45 MHz in 400 ms. We use 5ms of “gray” molasses, where the repumper power is dropped by 95%, the optical trapping power is ramped down to 50%, and the detuning is swept from -18MHz to -26MHz. The molasses phase requires the cancellation of imbalances in intensity between beams and also of residual magnetic fields [50]. After the molasses phase, 0.5-1 ms of “depumping” light is applied to put all the ^{87}Rb atoms into the $F=1$ level before loading into the magnetic trap. Exact MOT and molasses parameters were found through empirical optimization, and all listed numbers should be considered as rough guides.

The ^{23}Na apparatus uses a dark-spot MOT [51], with a detuning of -15MHz, peak beam intensity of 8.8 mW/cm 2 and a magnetic field gradient of 11G/cm. A 4 mm diameter opaque circle blocks light in the middle of a single repumper beam, creating a region at the center of the MOT where trapped atoms are optically pumped into the $F=1$ state. The ^{23}Na MOT equilibrates after a few seconds of loading. The effectiveness of the dark-spot in ^{23}Na has precluded the need for the compression and molasses phases as in ^{87}Rb . Typically 99% of the atoms are in the $F=1$ (dark) hyperfine state [51].

VII. MAGNETIC TRAP

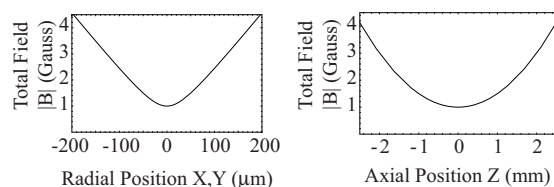


FIG. 7: Profile of the Ioffe-Pritchard trap magnetic field magnitude. The trap parameters are $B'=223$ G/cm, $B''=100$ G/cm 2 , and $B_0=1$ G.

Atoms in weak magnetic field seeking states can be trapped in a magnetic field minimum. Our magnetic trap is a high current Ioffe-Pritchard (IP) trap with a cloverleaf style winding that can hold $F=1$, $m_F = -1$ or $F=2$, $m_F = +2$ ground state atoms of ^{87}Rb and ^{23}Na with long lifetimes. An IP trap has an anisotropic, “cigar”-shaped, 3D harmonic shape for energies which are small compared to the trap minimum $g_F m_F \mu_B B_0$ and a 2D linear/1D harmonic shape at higher energies (See Fig. 7 and Appendix C). This linear regime at higher energies (higher cloud temperatures) is more efficient for evaporatively

cooling hot atoms [52], while the finite bias field at the minimum prevents Majorana spin flip loss of colder atoms. The similar magnetic moment of ^{87}Rb and ^{23}Na allows us to use of the same magnetic trap design, with ^{23}Na realizing double the trap frequencies of ^{87}Rb due to its lower mass.

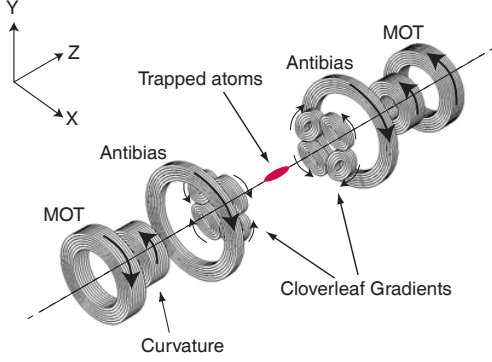


FIG. 8: Exploded view of the cloverleaf style Ioffe-Pritchard trap coils. Arrows indicate the direction of current flow. MOT coils are not on during magnetic trapping. Performance and design details are listed in Table III of Appendix C

Fig. 8 shows an expanded view of the magnetic trap coils. The two sets of four cloverleaf coils create radial gradients B' along \hat{x} and \hat{y} , while the curvature coils produce a parabolic field curvature B'' in the \hat{z} direction. The curvature coils also produce a substantial bias field (Table III, Appendix C) along \hat{z} , which is balanced by a roughly homogeneous field from the antibias coils, resulting in a low residual bias field B_0 of ~ 1 G at the center of the trap. The subtraction of the large magnetic fields from the curvature and antibias coils can make the residual bias field B_0 susceptible to jitter from current noise. To prevent this we drive current through both coils in series from the same power supply (Appendix C, Fig. 12), reducing the effect of current noise in the residual bias field B_0 by ≈ 30 . When assembled the antibias coils enclose the cloverleaf coils and the MOT coils surround the curvature coils.

To preserve phase space density during the transfer of atoms into the magnetic trap, additional current is applied to the curvature coils, increasing the residual bias field and decreasing the radial confinement to make a roughly spherical magnetic trap that more closely mode matches the spherical MOT. After loading the atoms in the trap, the additional curvature coil current is reduced over one second to adiabatically change the trap geometry to the tightly confining cigar shape, favorable for evaporative cooling. Sec. 2.3.2 of Ref. [53] has an extensive discussion of mode matching magnetic traps to MOTs. The adiabatic compression technique is reviewed in Ref. [52].

VIII. CONTROL AND IMAGING

Two computers run the apparatus; one controls the various parts of experiment and the other processes images from a camera which images the atoms. The control computer has custom built National Instruments (NI) LabWindows based software to drive analog (2 NI Model PCI 6713, 8 channels of 12 bit analog, 1MS/s update) and digital output (2 NI Model PCI-6533, 32 channels of binary TTL, 13.3 MS/s update) boards. The control computer also controls an Agilent 33250A 80MHz function generator through a GPIB interface, and triggers a Princeton Instruments NTE/CCD-1024-EB camera through a ST-133 controller to capture the absorption images.

BECs are typically imaged 10-40 ms after release from the trap. Ref. [53, 54] provides details for analyzing condensates after free expansion. Atoms are first optically pumped into the $F=2$ state in $200\mu\text{s}$ and then an absorption image is taken using resonant $F=2 \rightarrow F'=3$ light. Detuning off resonance causes dispersion (lensing) as the light passes through the cloud of atoms and can distort the image. The intensity of the imaging probe is kept lower than the saturation intensity to prevent bleaching of the transition, which would lead to errors in atom number counting. Typical exposure times are between $50\text{-}200\mu\text{s}$. Sec. 3 of Ref. [53] discusses other imaging techniques that can also be used to probe BECs. Our control and imaging techniques work equally well for ^{23}Na and ^{87}Rb .

IX. EVAPORATION

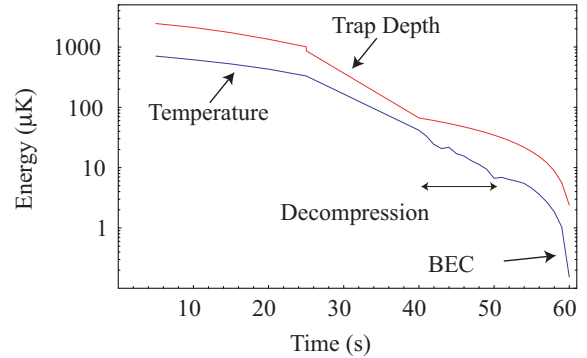


FIG. 9: Typical temperature and trap depth during evaporation to BEC in ^{87}Rb . The trap is decompressed between $t=40\text{-}50$ s by changing the trap parameters $B' = 223 \rightarrow 54$ G/cm, $B'' = 99 \rightarrow 25$ G/cm², and $B_0 = 1.4 \rightarrow 0.87$ G. Temperature was determined by fitting after ballistic expansion.

Evaporative cooling works by selectively removing hot atoms from the trapped cloud, while the remaining atoms rethermalize to a lower temperature. The efficiency of cooling depends on η , the ratio of trap depth or energy of the escaping atoms to the temperature $k_B T$, and is reduced by the rate of heating. The speed of evaporation depends on how quickly

the atoms rethermalize. In a magnetic trap evaporation is implemented through RF induced transitions between trapped and untrapped states. A given RF frequency corresponds to a shell of constant $\mu_m |\mathbf{B}|$ where the transitions occur. Atoms that pass through this shell enter untrapped states and are lost; thus RF provides a flexible mechanism to control the magnetic trap depth. Our RF antenna consists of two rectangular loops of wire, 10 cm x 2 cm, positioned 3 cm above and below the condensate as depicted in Fig. 2. Evaporation works equivalently well for ^{23}Na and ^{87}Rb , with ^{23}Na 's lower mass resulting in higher trap frequencies, which roughly compensates for its smaller elastic cross section (Table II).

To evaporate thermal atoms to a BEC, we sweep the RF frequency over several seconds using an Agilent 33250A synthesizer amplified with a 5 W RF amplifier (Mini-Circuits ZHL-5W-1). Typical evaporation curves for ^{87}Rb would ramp from 60 MHz down to ~ 0.8 MHz in 15 to 40 seconds, with similar parameters for ^{23}Na . Forced RF evaporative cooling is very efficient, increasing phase space density by $> 10^6$ (Table I). Fig. 9 shows the drop in temperature as the trap depth (calculated from the RF frequency) is lowered during evaporation of ^{87}Rb . Evaporation curves are frequently adjusted in the interest of tuning evaporation speed, atom number, density, and/or reproducibility. For instance, the atom number can be increased by decompressing the magnetic trap near the end of the evaporation. This reduces the effects of three body recombination heating by lowering the final condensate density. Such decompression techniques have allowed us to create nearly pure condensates with $N_c \approx 20 \times 10^6$ in both ^{87}Rb and ^{23}Na with lifetimes in excess of 5 seconds.

Decompressing the trap shifts its center due to gravitational sag and imperfections in the balance of magnetic fields between the coils. Such movements can excite oscillations in the cloud, which results in the condensation of BECs which are not at rest. Even in the absence of excitations, the magnetic field gradients must exert a force on the atoms which is greater than gravity for them to remain trapped. This limits the extent to which magnetic traps can be decompressed. Specially designed gravito-magnetic traps have been decompressed down to 1 Hz [22] to investigate very cold, dilute BECs.

X. DEEP TRAP LIMITATIONS

A major difference we have observed between ^{87}Rb and ^{23}Na condensates is the unexpectedly high decay rate of ^{87}Rb condensates in tightly confining deep traps, such as those used for transport in an optical tweezer [19]. At typical densities of condensates, the lifetime and heating are usually dominated by three-body recombination decay. However, the factor of four difference in the three-body rate coefficients (Table II) was insufficient to explain this major discrepancy in behavior. Three body recombination results in a diatomic molecule and an atom which fly apart with a total kinetic energy equal to the binding energy of the diatomic molecule in the highest vibrational state. This binding energy can be estimated from the scattering length as $E_0 \sim \hbar^2/ma^2$ [55] ($\sim 200\mu\text{K}$ in ^{87}Rb , ~ 2.7 mK in ^{23}Na).

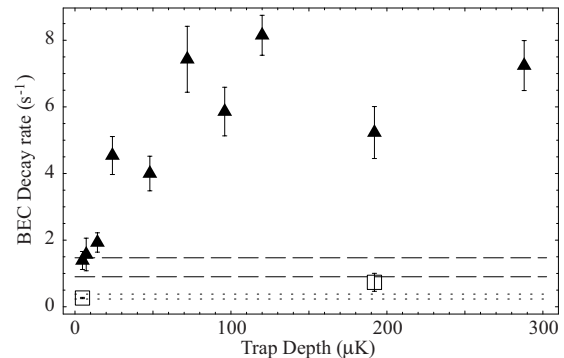


FIG. 10: Initial loss rates for ^{87}Rb BEC in deep traps. Trap depth dependence of the loss for large and small ^{87}Rb BECs in a 220 Hz x 220 Hz x 9 Hz magnetic trap. The trap depth was controlled by RF truncation. Condensates were nearly pure ($N_c/N > 90\%$) and consisted of $F=1$, $m_F=-1$ atoms. Solid triangles are data for a large condensate, $N_c = 2.7 \times 10^6$ atoms, peak density $n_p = 6.1 \times 10^{14}/\text{cm}^3$, expected three body decay time $\tau_3 = 0.85 \pm 0.22$ s (dashed horizontal lines) [58], and calculated collisional opacity of 0.88 [56]. Open squares are data for a small condensate, $N_c = 5 \times 10^5$ atoms, peak density $n_p = 3.1 \times 10^{14}/\text{cm}^3$, expected three body decay time $\tau_3 = 3.3 \pm 0.8$ s (dotted horizontal lines), and a calculated collisional opacity of 0.32. The error bars represent the statistical uncertainty in the decay curves. Additional scatter in the data is due to fluctuations in the atom number.

We investigated this issue in a magnetic trap instead of an optical trap. While it is easier experimentally to create tight trapping and hence high densities in an optical trap, both the trap frequencies and trap depth are functions of the optical power. This makes it difficult to separate density dependent effects, which are strongly affected by the trap frequency, from trap depth effects. In contrast, in a magnetic trap the trap depth can be controlled independently of the trap frequencies by adjusting the RF frequency which flips atoms to untrapped states.

There are two possible processes, both involving secondary collisions, which can greatly enhance the heating and losses due to the primary three-body collisions. The first process is collisional avalanches, similar to a chain reaction, where the energetic products of three-body recombination collide with additional atoms while leaving the condensate. This process depends on the collisional opacity $\sim n\sigma l$, where $\sigma = 8\pi a^2$ is the atom atom scattering cross section, and should increase dramatically when the condensate exceeds the critical opacity of 0.693 [56]. This process occurs entirely within the condensate volume and hence is independent of trap depth.

The second process can already occur at lower collisional opacities and relies on the retention of primary or secondary collision products by the trap in the so-called Oort cloud [53, 57]. The retention of these atoms in the trap can cause heating and loss in the condensate as they oscillate through the condensate volume. The retention of collision products in the Oort cloud should depend on whether the trap depth is larger or smaller than their energies.

Fig. 10 shows the initial loss rates measured for a large and a small BEC as a function of the magnetic trap depth. At low trap depths ($5 \mu\text{K}$) both the large and small condensate decay rates are in agreement with established three body recombination rates [58]. Therefore, the avalanche effect does not significantly contribute to the observed decay rate, although the calculated collisional opacity for the larger condensate was 0.88 and may not be far away from the onset of avalanches. In Ref [56] evidence for avalanches was observed at a collisional opacity of 1.4.

At high trap depths, the decay rate strongly increases for larger condensates and shortens the lifetime to less than 500 ms. In contrast, at low trap depths the large condensate had a lifetime of greater than 20 seconds, in agreement with the expected losses from three body decay. For trap depths greater than $\sim 50 \mu\text{K}$ the large ^{87}Rb condensate decay rate saturates, suggesting a maximum Oort energy.

We speculate that this enhancement of three-body related losses was not observed in ^{23}Na for several reasons. The primary decay products are mono-energetic and will escape unless the trap depth is greater than their kinetic energy (min $\sim 70 \mu\text{K}$ for ^{87}Rb , $\sim 900 \mu\text{K}$ for ^{23}Na). On their way out of the condensate volume, some of the primary three body decay products will collide with additional condensate atoms. In ^{23}Na the elastic scattering cross section σ is 3.6 times smaller than for ^{87}Rb , making these secondary collisions less likely. The products of such secondary collisions have a range of energies. In ^{23}Na these secondary products will typically have much higher energies, reducing their chance of remaining in the trap. In addition, the retained Oort particles need to collide with the condensate to cause additional loss. These subsequent collisions can further populate the Oort cloud.

For traps whose depths are in the intermediate region, below the minimum energy of the primary three body recombination products, the combination of greater primary three body decay rate, greater collision opacity, and greater fraction of secondary products retained by the Oort cloud lead to an estimated loss rate several orders of magnitude higher for ^{87}Rb than ^{23}Na in condensates of similar size and density.

The restricted optical access (Fig. 2) of our experiments limits the longitudinal (tweezer axis) trap frequency per unit trap depth. This requires optical trap depths for transporting condensates in our systems that are a significant fraction of the primary ^{87}Rb decay product energy, but a small fraction of that for ^{23}Na . Therefore ^{23}Na condensates can be easily transported using optical tweezers. For ^{87}Rb the preferred method is to transport a cloud at temperatures just above condensation, where the density is lower, and evaporate to BEC after transport.

XI. DISCUSSION

We have constructed ^{87}Rb and ^{23}Na Bose-Einstein condensate machines with nearly identical designs. In this section we highlight differences in their performance and operation. Key properties of the two species are highlighted in Table II. The four principal differences are their vapor pressure, resonant

	^{87}Rb	^{23}Na
D ₂ line λ (nm)	780	589
D ₂ linewidth $\Gamma/2\pi$ (MHz)	6.1	9.8
Gravity mg/k_B (nK/ μm)	102	27
Gravity $mg/g_F m_F \mu_B$ (G/cm)	30	8.1
Three body constant K_3 (cm^6/s)	8×10^{-30} [58]	2×10^{-30} [60]
Scattering length a (nm)	5.3 [59]	2.8 [68]
Recoil velocity v_r (mm/s)	5.9	29

TABLE II: Select properties ^{87}Rb and ^{23}Na $F=1$, $m_F = -1$ ground states. Unless noted, quantities are derived from Ref. [69] and [36].

wavelength, recoil velocity, and collisional properties.

The high vapor pressure of rubidium allows oven operation at lower temperatures, but requires a more elaborate oven geometry to avoid deposition of rubidium on surfaces of the main UHV chamber. The lower vapor pressure of sodium requires a higher oven operating temperature to produce comparable flux. In a Zeeman slower the stopping length L for the most probable velocity in a thermal beam is $L = \frac{3k_B T}{\hbar k \Gamma}$, assuming the maximum spontaneous light force. Resonant sodium light, with a shorter wavelength and larger natural linewidth, exerts a greater spontaneous light force than in rubidium. In our systems the gain from the greater light force in sodium is balanced out by the higher operating temperatures required of the sodium oven to produce comparable flux, resulting in both the rubidium and sodium slower being about 1 m in length.

The spontaneous emission of slowing photons adds a random, diffuse velocity to the atoms as they are slowed. Due to the higher recoil velocity and greater deceleration, the slow ^{23}Na beam has a larger divergence than the ^{87}Rb beam. By keeping the distance between the end of the ^{23}Na slower and the MOT to a minimum, we maximize transfer of atoms from the slower to the MOT. Our setup for ^{87}Rb was almost identical, but we expect that the requirement of keeping the slower and the MOT close could be relaxed. Although we have not tried it, we expect that our ^{87}Rb experiment would work for ^{23}Na with increased slower coil current but without changes to the oven, vacuum or magnet designs.

On the laser side, a major difference is the availability of low cost high power laser diodes in the near infrared region around 780 nm. In our experience a well run dye laser system can provide similar performance to a diode laser system with several master and slave lasers. However, occasionally dye lasers require major maintenance in terms of dye changes or full optical realignment. An advantage in sodium is the visibility of the laser light and the atomic fluorescence. The near infrared 780 nm light is only modestly visible, whereas the sodium line at 589 nm is near the peak of human eye sensitivity and allows fine alignments of the laser beams and the magneto-optical trap without cameras, IR cards, or IR viewers.

^{87}Rb has favorable properties for laser cooling and atom interferometry because of its greater mass, lower recoil ve-

locity, and larger excited state hyperfine structure. While greater mass and longer resonant wavelength give ^{133}Cs an even lower recoil velocity, its complicated collisional behavior at low magnetic fields makes it difficult to cool to BEC [12]. The lowest molasses temperature in rubidium is a factor of ten lower than for sodium. However, in BEC experiments the laser cooling is optimized for large atom numbers and high initial elastic collision rates in the magnetic trap, and not for the lowest temperature. For laser cooling sodium at high atom numbers, the Dark SPOT technique [51] is crucial to avoid re-scattering of light in the MOT, whereas it is not necessary in rubidium experiments. At the end of the day, although with somewhat different techniques, laser cooling works equally well for both atoms.

Both atomic species have favorable collisional properties for evaporative cooling. The elastic scattering cross section of ^{87}Rb atoms at low temperature is four times higher than in ^{23}Na . However, elastic collision rates after laser cooling are comparable since ^{23}Na atoms have a higher velocity for a given temperature. An advantage of ^{87}Rb is that the two ground electronic state hyperfine levels have similar scattering lengths, which can be advantageous for studies on spinor condensates and atomic clock transitions. Also, spin relaxation between the two hyperfine levels is almost completely suppressed. Mixtures of $F=1$ and $F=2$ ^{87}Rb atoms can be kept for seconds [59], whereas in ^{23}Na they decay in ms [60]. Both atoms have several Feshbach resonances below 1100 G [61–63], but ^{87}Rb has the disadvantage that the widest known resonance is only 200 mG wide compared to 1 G for ^{23}Na and thus requires more stable magnetic fields. Another limitation is the higher rate of three-body collisions for ^{87}Rb atoms. As we discussed in Sec. X, this imposes limitations on trapping and manipulating dense ^{87}Rb condensates.

XII. CONCLUSIONS

In this paper, we have presented details for designing BEC machines with high performance and flexibility, and we hope that this description is useful for designing new experiments. Given the recent developments in the field, there is more than enough room for new experiments to join in the exploration of atom optics and many-body physics with quantum-degenerate atomic gases.

Funding for the ^{87}Rb machine was provided by the NSF MIT-Harvard Center for Ultracold Atoms. Funding for the ^{23}Na machine came from NSF, the ARO MURI program, NASA, and the ONR.

We thank S. Gupta, A. Görlitz, and A. E. Leanhardt for their contributions to the construction of the ^{23}Na machine; J. C. Mun and P. Medley for ongoing contributions to the ^{87}Rb machine; and MIT UROP students P. Gorelik and X. Sun for various contributions to the ^{87}Rb machine. The authors would also like to thank M. Saba and D. Kielpinski for critical reading of this manuscript.

APPENDIX A: OVEN

To sustain a high flux atomic beam, the background vacuum pressure must be low enough that the mean free path between collisions is much greater than the length of the beam. To generate an effusive beam with a thermal distribution of velocities, the size of the hole through which the atoms escape must be smaller than the mean free path inside the oven. We observed in sodium that at higher pressures (e.g. temperatures) the flux of slowable atoms does not increase and the velocity distribution narrows. This phenomena is well understood [35], and limits the flux of slow atoms from a single aperture oven.

During servicing, a clean ampoule is essential for rapid recovery of good vacuum pressure. The ampoule is cleaned by submerging it in a 50/50 mixture by volume of acetone and isopropanol for 20 minutes, air drying it. This removes most of the water from the glass surface, which would otherwise require more time to pump away. In the rubidium experiment the cleaned ampoule is placed in the oven while still sealed and baked for 24 hours under vacuum at 150–180°C to remove the remaining contaminants before it is broken.

To prevent accumulation of metal at the aperture (Fig. 3, J), the oven nozzle temperature (Fig. 3, K) is kept higher ($\sim 10^\circ\text{C}$ in rubidium and $\sim 90^\circ\text{C}$ in sodium) than the rest of the oven. The velocity distribution of the beam is determined by the nozzle temperature (Fig. 3, K). On the other hand, the vapor pressure in the oven, which controls the beam flux, is dominated by the coldest spot in the elbow and bellows. The factor of two discrepancy between the observed and calculated (Table IV) rubidium oven lifetimes at 110°C can be accounted for by a spot $\sim 10^\circ\text{C}$ colder than the lowest measured oven temperature. The specifics of this cold spot depend on how the oven is insulated.

APPENDIX B: ZEEMAN SLOWER

Every photon which scatters off an atom to slow the atom is radiated in a random direction, increasing the atoms spread in transverse velocity. The beam emerging from the tube needs to have sufficient forward mean velocity to load the MOT efficiently. Because of the random direction of the emission recoil, N photon scatterings increase the transverse velocity by $v_r\sqrt{N/3}$. The ^{23}Na slower operates with a recoil induced transverse exit velocity of $\approx 3\text{m/s}$, at a final forward velocity of 30 m/s so that the spatial transverse spread in the slowed beam matches the MOT capture area. The smaller initial and recoil velocities in the ^{87}Rb slower reduce the transverse velocity to $\approx 0.8\text{m/s}$, resulting in a more collimated slowed beam whose transverse width is smaller than the size of the MOT beams.

An additional concern in both slower is the fate of atoms not captured by the MOT. In ^{87}Rb we were concerned with the potential adverse impact a deposited film may have on the vapor pressure, and installed a cold plate near the slower window on the main chamber to capture desorbed Rb. Vacuum pressure has not been an issue and we have never needed to chill

is supplied from a Model ESS 30-500 15kW power supply, while the axial currents are driven with two Model EMS 20-250 5kW power supplies. Each power supply is protected against damage from reverse current with an International Rectifier SD600N04PC high-current diode.

To switch the high currents we use PowerEx models CM1000HA-24H and CM600HA-24H Integrated Gate Bipolar Transistors (IGBTs) controlled with PowerEx BG1A-F IGBT driver kits. The IGBTs and high current diodes dissipate several hundred W during operation, and are cooled with chilled water. Efficient heat sinking is critical for reliable operation, as thermal dissipation limits the maximum DC current. Fast turnoff of current on an inductive load, such as a coil, results in a large voltage spike. We have added a “de-bounce” circuit to each of the coil systems (Fig. 12) to control this process and prevent damage. The circuit consists of two different elements: a varistor (V) and a diode (D) in series with a low impedance resistor (R). The varistor shorts the circuit at high voltages to prevent this spike, and the diode (D) in series with a 1Ω resistor (R) dissipates the remaining current after varistor shutoff. Ref. [66] contains a thorough analysis of the behavior of a similar circuit. All control signals are electrically isolated from the high-current circuits to prevent voltage spikes from damaging connected hardware. Rapid, controlled magnetic field shutoff is important for quantitative interpretation of images taken after ballistic expansion.

3. Wire

Both the slower and the magnetic trap coils were fabricated using square hollow core (0.125 in./side, 0.032 in. wall) Alloy 101 soft temper copper tubing from Small Tube Products, Inc. of Altoona, PA, wrapped with double Dacron glass fuse insulation by Essex Group Inc., Magnet Wire & Insulation of Charlotte, NC. The coils are held together with Hysol Epoxi-Patch 1C White high temperature epoxy that is bakable to 170°C . Chilled water is forced through the hollow core of the copper wires to dissipate the $\approx 10\text{kW}$ of power generated from resistive heating in the magnetic trap and Zeeman slower coils. 200 psi of differential pressure is required for sufficient coolant flow. We designed all our coils to increase the cooling water temperature by less than 50°C . Ch. 3 of Ref. [67] has

an extensive discussion of water cooling in continuously powered resistive magnets. For our wire the following empirical relationships and numbers were measured,

$$\rho [\Omega/m] = 2.65 \times 10^{-3} \quad (\text{C4})$$

$$Q [\text{ml}/\text{sec}] = 2.07 \sqrt{\frac{\Delta P [\text{psi}]}{L [\text{m}]}} \quad (\text{C5})$$

$$\Delta T [^\circ\text{C}] = 259 I^2 [\text{Amps}] \rho \sqrt{\frac{L^3 [\text{m}]}{\Delta P [\text{psi}]}} \quad (\text{C6})$$

where Q is the water flow rate in ml/sec, $I^2 \rho L$ is the power dissipated by the coil, ΔP the pressure drop in psi (1 psi=6.89 kPa), and L the length of the coil in meters.

4. Fabrication

All of the components for each half of the magnetic trap were epoxied together for stability. Each assembly was then mounted in the bucket windows with an aluminum mounting plate backed by four threaded Alloy 316 stainless steel rods. No ferromagnetic materials were used in the mounting because of concern for irreproducibility from hysteresis effects. Table III lists the windings and typical parameters for each coil.

Coil	Winding		Current (A)	Inner \emptyset (cm)	Field
	Turns	Layers			
Antibias	3	6	95	10.5	$B'' = +9 \text{ G}/\text{cm}^2$ $B_0 = -243 \text{ G}$
Curvature	8	6	95	3.2	$B'' = +90 \text{ G}/\text{cm}^2$ $B_0 = +251 \text{ G}$
Gradient	3	4	470	0.8 x 2.3	$B' = 223 \text{ G}/\text{cm}$
MOT	7	4+2 ^a	15	~ 7 , to fit	16.5 G/cm in \hat{z}

^aSegmented for improved cooling.

TABLE III: Magnetic trap coil winding and performance specifications. Fig. 8 illustrates their assembly and direction of current flow.

-
- [1] E. A. Cornell and C. E. Wieman, Rev. Mod. Phys. **74**, 875 (2002).
[2] W. Ketterle, Rev. Mod. Phys. **74**, 1131 (2002).
[3] M. H. Anderson, J. R. Ensher, M. R. Matthews, C. E. Wieman, and E. A. Cornell, Science **269**, 198 (1995).
[4] K. B. Davis, M.-O. Mewes, M. R. Andrews, N. J. van Druten, D. S. Durfee, D. M. Kurn, and W. Ketterle, Phys. Rev. Lett. **75**, 3969 (1995).
[5] C. C. Bradley, C. A. Sackett, J. J. Tollett, and R. G. Hulet, Phys. Rev. Lett. **75**, 1687 (1995), *ibid.* **79**, 1170 (1997).
[6] C. Bradley, C. Sackett, and R. Hulet, Phys. Rev. Lett. **78**, 985 (1997).
[7] D. Fried, T. Killian, L. Willmann, D. Landhuis, S. Moss, D. Kleppner, and T. Greytak, Phys. Rev. Lett. **81**, 3811 (1998).
[8] S. Cornish, N. Claussen, J. Roberts, E. Cornell, and C. Wieman, Phys. Rev. Lett. **85**, 1795 (2000).
[9] A. Roberts, O. Sirjean, A. Browaeys, J. Poupard, S. Nowak, D. Boiron, C. Westbrook, and A. Aspect, Science **292**, 461 (2001).
[10] F. Santos, J. Wang, C. Barrelet, F. Perales, E. Rasel, C. Unnikrishnan, M. Leduc, and C. Cohen-Tannoudji, Phys. Rev. Lett **86**, 3459 (2001).
[11] G. Modugno, G. Ferrari, G. Roati, R. Brecha, A. Simoni, and M. Inguscio, Science **294**, 1320 (2001).

- [12] T. Weber, J. Herbig, M. Mark, H. Nagerl, and R. Grimm, *Science* **294**, 232 (2003).
- [13] Y. Takasu, K. Maki, K. Komori, T. Takano, K. Honda, M. Kumakura, T. Yabuzaki, and Y. Takahashi, *Phys. Rev. Lett.* **91**, 030404 (2003).
- [14] A. Griesmaier, J. Werner, S. Hensler, J. Stuhler, and T. Pfau, *Phys. Rev. Lett.* **94**, 160401 (2005).
- [15] H. Ott, J. Fortagh, G. Schlotterbeck, A. Grossmann, and C. Zimmermann, *Phys. Rev. Lett.* **87**, 230401 (2001).
- [16] K. Dieckmann, R. J. C. Spreeuw, M. Weidemüller, and J. T. M. Walraven, *Phys. Rev. A* **226**, 3891 (1998).
- [17] R. S. Conroy, Y. Xiao, M. Vengalattore, W. Rooijackers, and M. Prentiss, *Opt. Comm.* **226**, 259 (2003).
- [18] H. Lewandowski, D. Harber, D. Whitaker, and E. Cornell, *J. Low Temp Phys* **132**, 309 (2003).
- [19] T. Gustavson, A. Chikkatur, A. Leanhardt, A. Görlitz, S. Gupta, D. Pritchard, and W. Ketterle, *Phys. Rev. Lett.* **88**, 020401 (2002).
- [20] A. E. Leanhardt, A. P. Chikkatur, D. Kielpinski, Y. Shin, T. L. Gustavson, W. Ketterle, and D. E. Pritchard, *Phys. Rev. Lett.* **89**, 040401 (2002).
- [21] A. P. Chikkatur, Y. Shin, A. E. Leanhardt, D. Kielpinski, E. Tsikata, T. L. Gustavson, D. E. Pritchard, and W. Ketterle, *Science* **296**, 2193 (2002).
- [22] A. E. Leanhardt, T. A. Pasquini, M. Saba, A. Schirotzek, Y. Shin, D. Kielpinski, D. E. Pritchard, and W. Ketterle, *Science* **301**, 1513 (2003).
- [23] A. E. Leanhardt, Y. Shin, A. P. Chikkatur, D. Kielpinski, W. Ketterle, and D. E. Pritchard, *Phys. Rev. Lett.* **90**, 100404 (2003).
- [24] Y. Shin, M. Saba, M. Vengalattore, T. A. Pasquini, C. Sanner, A. E. Leanhardt, M. Prentiss, D. E. Pritchard, and W. Ketterle, *Phys. Rev. Lett.* **93**, 160406 (2004).
- [25] T. Pasquini, Y. Shin, C. Sanner, M. Saba, A. Schirotzek, D. Pritchard, and W. Ketterle, *Phys. Rev. Lett.* **93**, 223201 (2004).
- [26] Y. Shin, M. Saba, A. Schirotzek, T. A. Pasquini, A. E. Leanhardt, D. E. Pritchard, and W. Ketterle, *Phys. Rev. Lett.* **92**, 150401 (2004).
- [27] Y. Shin, M. Saba, T. Pasquini, W. Ketterle, D. Pritchard, and A. Leanhardt, *Phys. Rev. Lett.* **92**, 050405 (2004).
- [28] D. Schneble, Y. Torii, M. Boyd, E. Streed, D. E. Pritchard, and W. Ketterle, *Science* **300**, 475 (2003).
- [29] D. Schneble, G. K. Campbell, E. W. Streed, M. Boyd, D. E. Pritchard, and W. Ketterle, *Phys. Rev. A* **69**, 041601 (2004).
- [30] G. Campbell, M. Boyd, D. Pritchard, and W. Ketterle, *Phys. Rev. Lett.* **94**, 170403 (2005).
- [31] E. Raab, M. Prentiss, A. Cable, S. Chu, and D. Pritchard, *Phys. Rev. Lett.* **59**, 2631 (1987).
- [32] J. O'Hanlon, *A user's guide to vacuum technology* (Wiley-Interscience, Hoboken, NJ, 1989).
- [33] Simon Hanks of UKAEA, D4/05 Culham Science Center, Abingdon, UK.
- [34] A. P. Chikkatur, Ph.D. thesis, Massachusetts Institute of Technology (2002), http://cua.mit.edu/ketterle_group/Theses/thesis_APC.pdf.
- [35] H. Pauly and C. Scoles, *Atomic and Molecular Beam methods Vol I*. (Oxford University Press, Oxford, 1988).
- [36] D. Steck, <http://steck.us/alkalidata/sodiumnumbers.pdf> (2003).
- [37] C. Alcock, V. Itkin, and M. Horrigan, *Canadian Metallurgical Quarterly* **23**, 309 (1984).
- [38] M. Walkiewicz, P. Fox, and R. Scholten, *Rev. Sci. Instr.* **71**, 3342 (2000).
- [39] W. Phillips and H. Metcalf, *Phys. Rev. Lett.* **48**, 596 (1982).
- [40] T. Barrett, S. Daporeschwartz, M. Ray, and G. Lafyatis, *Phys. Rev. Lett.* **67**, 3483 (1991).
- [41] C. Slowe, L. Vernac, and L. V. Hau, *Rev. Sci. Instr.* **76**, 103101 (2005).
- [42] Y. Yoshikawa, T. Umeki, T. Mukae, Y. Torii, and T. Kuga, *Appl. Opt.* **42**, 6645 (2003).
- [43] C. Pearman, C. Adams, S. Cox, P. Griffin, D. Smith, and I. Hughs, *J. Phys. B* **35**, 5141 (2002).
- [44] A. Siegman, *Lasers* (University Science Books, Sausalito, CA, 1986).
- [45] D. M. Stamper-Kurn, Ph.D. thesis, Massachusetts Institute of Technology (2000), http://cua.mit.edu/ketterle_group/Theses/thesis_DMSK.pdf.
- [46] IPG Photonics EAD and RLM series amplifiers.
- [47] H. Moosmüller and J. Vance, *Optics Lett.* **22**, 1135 (1997).
- [48] J. Bienfang, C. A. Denman, B. W. Grime, P. D. Hillman, G. T. Moore, and J. M. Telle, *Optics Lett.* **28**, 2219 (2003).
- [49] R. J. Thompson, M. Tu, D. C. Aveline, N. Lundblad, and L. Maleki, *Optics Express* **11**, 1709 (2003).
- [50] S. Shang, B. Sheehy, P. van der Straten, and H. Metcalf, *Phys. Rev. Lett.* **67**, 1094 (1991).
- [51] W. Ketterle, K. Davis, M. Joffe, A. Martin, and D. Pritchard, *Phys. Rev. Lett.* **70**, 2253 (1993).
- [52] W. Ketterle and N. van Druten, in *Advances in AMO Physics*, edited by B. Bederson and H. Walther (Academic Press, San Diego, 1996), vol. 37, p. 181, http://cua.mit.edu/ketterle_group/Projects_1996/Pubs_96/kett96_evap_preprint.pdf.
- [53] W. Ketterle, D. S. Durfee, and D. M. Stamper-Kurn, Bose-Einstein Condensation in Atomic Gases, *Proceedings of the International School of Physics "Enrico Fermi" Course CXL* (IOS Press Amsterdam, 1999), cond-mat/9904034.
- [54] Y. Castin and R. Dum, *Phys. Rev. Lett.* **77**, 5315 (1996).
- [55] B. Borca, J. W. Dunn, V. Kokkoulina, and C. H. Greene, *Phys. Rev. Lett.* **91**, 070404 (2003).
- [56] J. Schuster, A. Marte, S. Amtage, B. Sang, G. Rempe, and H. C. W. Beijerinck, *Phys. Rev. Lett.* **87**, 170404 (2001).
- [57] E. A. Burt, R. W. Ghrist, C. J. Myatt, M. J. Holland, E. A. Cornell, and C. E. Wieman, *Phys. Rev. Lett.* **79**, 337 (1997).
- [58] B. Tolra, K. O'Hara, J. Huckans, W. Phillips, S. Rolston, and J. Porto, *Phys. Rev. Lett.* **92**, 190401 (2003).
- [59] D. Harber, H. Lewandowski, J. McGuirk, and E. Cornell, *Phys. Rev. A* **66**, 053616 (2002).
- [60] A. Görlitz, T. Gustavson, A. Leanhardt, R. Low, A. Chikkatur, S. Gupta, S. Inouye, D. Pritchard, and W. Ketterle, *Phys. Rev. Lett.* **90**, 090401 (2003).
- [61] S. Inouye, M. Andrews, J. Stenger, H.-J. Miesner, D. Stamper-Kurn, and W. Ketterle, *Nature* **392**, 151 (1998).
- [62] J. Stenger, S. Inouye, M. Andrews, H.-J. Miesner, D. Stamper-Kurn, and W. Ketterle, *Phys. Rev. Lett.* **82**, 2422 (1999).
- [63] A. Marte, T. Volz, J. Schuster, S. Durr, G. Rempe, E. G. M. van Kempen, and B. Verhaar, *Phys. Rev. Lett.* **89**, 283202 (2002).
- [64] D. S. Durfee, Ph.D. thesis, Massachusetts Institute of Technology (1999), <http://www.physics.byu.edu/faculty/durfee/DSDThesis.pdf>.
- [65] T. Bergeman, G. Erez, and H. J. Metcalf, *Phys. Rev. A* **35**, 1535 (1987).
- [66] B. F. Melton and V. L. Pollak, *J. Magn. Reson. A* **122**, 42 (1996).
- [67] D. Montgomery, *Solenoid magnet design; the magnetic and mechanical aspects of resistive and superconducting systems* (Wiley-Interscience, New York, 1969).
- [68] C. Samuelis, E. Tiesinga, T. Laue, M. Elbs, H. Knockel, and E. Tiemann, *Phys. Rev. A* **63**, 012710 (2000).

- [69] D. Steck, <http://steck.us/alkalidata/rubidium87numbers.pdf> (2002).
- [70] H. Metcalf and P. van der Straten, *Laser Cooling and Trapping*,

Graduate texts in contemporary physics (Springer-Verlag, New York, 1999).

Temp (°C)	Rb				Na			
	Velocity ^a (m/s)	Pressure [37] (torr)	Total Flux ^b #/sec	Lifetime ^c (hours)	Velocity ^a (m/s)	Pressure [36] (torr)	Total Flux ^b #/sec	Lifetime ^d (hours)
-30	266	2.5E-10	1.4E+10	-	513	1.9E-15	2.0E+05	-
0	282	2.0E-08	1.1E+12	-	544	5.7E-13	5.8E+07	-
25	295	4.0E-07	2.0E+13	-	569	2.8E-11	2.7E+09	-
39.3 ^e	302	1.8E-06	8.8E+13	-	582	1.9E-10	1.8E+10	-
90	325	1.2E-04	5.4E+15	1814	628	5.3E-08	4.7E+12	-
97.8 ^f	329	2.0E-04	9.1E+15	1070	634	1.1E-07	9.6E+12	-
110	334	4.5E-04	2.0E+16	489	645	3.3E-07	2.9E+13	-
120	339	8.3E-04	3.7E+16	267	653	7.9E-07	6.8E+13	-
130	343	1.5E-03	6.5E+16	151	661	1.8E-06	1.5E+14	-
140	347	2.6E-03	1.1E+17	87	669	4.0E-06	3.4E+14	-
150	351	4.4E-03	1.9E+17	52	677	8.6E-06	7.1E+14	-
160	355	7.3E-03	3.1E+17	32	685	1.8E-05	1.5E+15	-
230	383	1.5E-01	-	-	739	1.6E-03	1.2E+17	1487
240	387	2.1E-01	-	-	746	2.9E-03	2.2E+17	845
250	391	3.0E-01	-	-	753	5.0E-03	3.7E+17	486
260	394	4.1E-01	-	-	760	8.7E-03	6.4E+17	283
340	423	4.0E+00	-	-	815	5.2E-01	-	-
350	426	5.1E+00	-	-	822	8.3E-01	-	-
360	430	6.5E+00	-	-	829	1.3E+00	-	-

TABLE IV: Oven Design Parameters

^aMost probable,3D Beam, Sec 5.2 Ref. [70]^b5mm aperture^c5g Rb^d25g Na^emelting point Rb^fmelting point Na

Appendix C

Publication: Continuous and Discrete Quantum Zeno Effect

This appendix includes the paper "Continuous and Discrete Quantum Zeno Effect."

Continuous and Pulsed Quantum Zeno Effect

BECIV

MIT-Harvard Center for Ultracold Atoms, Research Laboratory of Electronics and Department of Physics,
Massachusetts Institute of Technology, Cambridge, MA 02139, USA

(Dated: January 8, 2006)

The quantum Zeno effect is the suppression of transitions between quantum states by frequent measurement. Oscillation between two ground hyperfine states of a magnetically trapped ^{87}Rb Bose-Einstein condensate, externally driven at a transition rate ω_R , was substantially suppressed by destructively measuring one of the levels with resonant optical scattering. While an ideal continuous measurement will stop the transition, any real measurement method will occur at a finite rate. The suppression of the transition rate in the two level system was quantified for pulsed measurements with a time between pulses δt and weak continuous measurements with a scattering rate γ . We observe that the weak continuous measurements exhibit the same suppression in the transition rate as the pulsed measurements when $\gamma\delta t = 3.60(0.43)$. This is in agreement with the previously predicted value of 4. Increasing the measurement frequency suppressed the transition rate to $0.005\omega_R$.

PACS numbers:

The quantum Zeno effect (QZE) is the suppression of transitions between states by frequent measurement. It was first considered as a theoretical problem relating to the decay of an unstable charged particle as it was measured traveling across a bubble chamber [1]. Under ideal continuous measurement the unstable particle would paradoxically remain in its initial state. The QZE is the quantum equivalent to the watched tea kettle that never boils. Understanding quantum measurement is essential in linking quantum systems to their classical surroundings.

The QZE can be used both to test fundamental physics and to solve practical problems. Agreement with existing theory can bound or exclude the effects of proposed extensions to quantum mechanics such as string theory or quantum gravity [2–4]. One example is using the agreement between experimental measurements of the QZE in an atomic system [5] and quantum mechanics to calculate an upper bound on possible stochastic perturbations in the Schrödinger equation [2]. This bound is similar to that obtained from particle physics experiments. Practical applications of QZEs include reducing irradiation levels in neutron tomography [6], managing decoherence in quantum computing [7–10], and reducing depolarization rates in spin polarized gases [11–13]. The security of quantum cryptography protocols [14] is derived from the nature of quantum measurement. In theory the Heisenberg uncertainty principal limits how frequently meaningful measurements can be performed. In practice imperfections in real measurements [15] cause losses which limit the maximum realizable suppression [16].

In a driven two level system the QZE from frequent optical scattering measurements to a third level [17] was shown to suppress the transition rate between hyperfine levels in trapped ions [5]. In addition to subsequent ion experiments [12, 18], QZEs have been observed in molecular collisions [11], neutral atoms tunneling out of an optical lattice [19], and the absorption of optical pumping light in spin polarized gas cells [13].

Oscillation between two states, externally driven at a transition rate ω_R , was substantially suppressed by destructive measurements of one of the levels with resonant optical scattering.

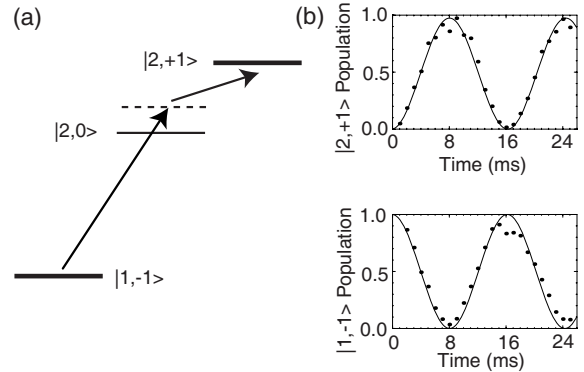


FIG. 1: The experimental two level quantum system consists of the $|1, -1\rangle$ and $|2, +1\rangle$ ground hyperfine states of ^{87}Rb . a. Ground hyperfine state energy level diagram for relevant levels in ^{87}Rb . Arrows depict the components of the two photon transition which connect the $|1, -1\rangle$ and $|2, +1\rangle$ states. 6.8 GHz microwaves couple the $|1, -1\rangle$ to a virtual intermediate state detuned 420 kHz above resonance with the $|2, 0\rangle$. Radio frequency (RF) at 1.68 MHz resonantly couples this virtual intermediate state to the $|2, +1\rangle$ state. b. Population of the $|1, -1\rangle$ and $|2, +1\rangle$ states as a function of time. Curves are fits to a two photon transition rate of $\omega_R/2\pi = 61.5(0.5)$ Hz. No population was detected in the intermediate $|2, 0\rangle$ state.

The suppression in the transition rate from continuous scattering measurements and pulsed scattering measurements were quantified and compared. For short times ($t \ll 1/\omega_R$) and when the initial population is only in one state the population transfer to the other state is $t^2\omega_R^2/4$. For frequent strong measurement pulses spaced δt , dividing this transfer rate by time gives an expected loss rate $1/\tau_{EP} = \delta t\omega_R^2/4$. τ_{EP} is the ideal initial state lifetime under pulsed measurement if no other loss mechanisms are present.

A laser beam with scattering rate γ has probability $1 - \exp(-t\gamma)$ of making a scattering measurement after time t . For large enough γ this probability $\rightarrow 1$ and the transition rate in the two level system is suppressed (strong measure-

ment limit), resulting in negligible QZE related atom decay rate. Other loss processes, such as background gas collisions, three body recombination, dipolar collisions, or off resonance scattering losses will then dominate the decay rate. For smaller γ the probabilistic nature of the scattering effectively allows free evolution for extended periods, such that the QZE measurement loss process dominates over that from other losses (weak measurement limit) and the expected loss rate is $1/\tau_{EC} = \gamma\omega_R^2$ [20]. τ_{EC} is the ideal initial state lifetime under continuous measurement if no other loss mechanisms are present. Both of these regimes are valid only in the frequent measurement limit $1/\delta t, \gamma \gg \omega_R$. We have measured these lifetimes and used them to verify the prediction [20] that the limit of many strong measurements with frequency $1/\delta t$ produces the same suppression of decay as a continuous weak measurement with a scattering rate γ when $\gamma\delta t = 4$. It is important to relate strong pulsed measurements to weak continuous measurements since any real strong measurement is only an approximation based on a series of weak continuous measurements. For practical applications, weak continuous measurements require fewer photons than pulsed measurements for the same suppression of the transition rate.

Here we have demonstrated the QZE in a magnetically trapped ^{87}Rb Bose-Einstein condensate. Externally driven transitions between two hyperfine states were suppressed by resonantly scattering optical photons off one hyperfine state. The 362 nK energy from a single photon recoil distinguishes scattered atoms from the $\mu=15\text{nK}$ subrecoil energy of the condensate atoms. The externally driven two level system [5, 18] and destructive measurement technique [19] are established techniques in QZE experiments. A condensate of $N_c = 5.0(0.5) \times 10^4$ ^{87}Rb atoms in the $5S_{1/2} |1, -1\rangle$ ($|F, m_F\rangle$) hyperfine ground state was prepared in a $\{63, 63, 6.6\}$ Hz magnetic trap [21]. An RF knife maintained a magnetic trap depth of $5 \mu\text{K}$. The observed lifetime of the condensate was greater than 5 s.

A two photon transition was used to drive coherent oscillations between the $5S_{1/2} |1, -1\rangle$ and $5S_{1/2} |2, +1\rangle$ states at a rate ω_R (Fig. 1). The $|1, -1\rangle$ and $|2, +1\rangle$ states were used because their magnetic moments exactly match at a magnetic field of 3.23 G [22]. Variations from this magnetic field would not change the transition frequency to first order. The magnetic bias field was lowered to 3.0 G [22] to compensate for the dephasing induced across the condensate by the density dependent clock shift. This created a uniform transition frequency across the condensate. A laser beam of 780 nm π polarized light tuned with an acousto-optic modulator to resonance with the $5S_{1/2} |2, +1\rangle \rightarrow 5P_{3/2} |3, +1\rangle$ transition at 3.0 G performed the optical scattering measurements. The laser beam had a $1/e^2$ diameter of $d_0 = 9.5(0.1)$ mm and was monitored with a photodiode. The condensate atom number was reduced from $N_c = 5.0(0.5) \times 10^6$ to $N_c = 5.0(0.5) \times 10^4$ by nearly adiabatic RF output coupling [23] to lower than density and collisional opacity. This reduced the chance of collisions between escaping atoms and the remaining condensate causing additional losses. After each QZE experiment was completed the magnetic trap was turned off and the surviving atoms were allowed to expand with 41 ms of ballistic expansion.

An RF pulse based state transfer technique [24] was used to map $|1, -1\rangle$ and $|2, +1\rangle$ populations into magnetically separable states where they could be simultaneously measured. When driven by the two photon transition the atoms coherently oscillated between the $|1, -1\rangle$ and $|2, +1\rangle$ states (Fig. 1) at a transition rate ω_R . Optical scattering measurements of atoms in the $|2, +1\rangle$ state reduced the total BEC population. When the frequency of measuring the $|2, +1\rangle$ state was increased the lifetime of atoms in the initial $|1, -1\rangle$ was increased by suppressing the transition rate to the $|2, +1\rangle$. The suppression of the transition rate through frequent measurements was because of the QZE.

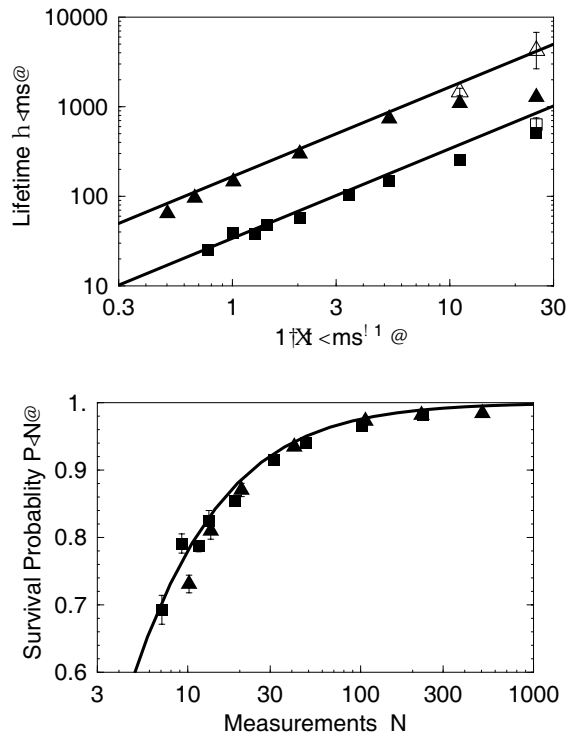


FIG. 2: Increase in the lifetime (upper) and survival probability (lower) of atoms in the initial $|1, -1\rangle$ state with more frequent pulsed measurements of the $|2, +1\rangle$ state. Solid lines indicate increases predicted for the pulsed QZE. Boxes (triangles) are data points for a transition rate $\omega_R/2\pi = 54.6(0.5)$ ($24.7(0.1)$) Hz between the $|1, -1\rangle$ and $|2, +1\rangle$ states without measurements. Upper: Observed lifetimes (Filled) for $|1, -1\rangle$ atoms measured with a time δt between $10 \mu\text{s}$ optical pulses resonant with the $|2, +1\rangle$. Lines indicate the expected QZE limited lifetime $\tau_{EP} = 1/4\delta t\omega_R^2$. Open symbols show lifetimes after correction for additional (non-QZE) measurement related losses by Eq. 1 ($\Gamma_m = 3.41(0.14)\text{s}^{-1}$, $2.96(0.22)\text{s}^{-1}$). Lower: The same data in terms of the survival probability for $N = \pi/\omega_R\delta t$ measurements performed during a π pulse time $t = \pi/\omega_R$ (without measurements the time to transfer 100% of the atoms from $|1, -1\rangle$ to $|2, +1\rangle$). The survival probability $P = \exp(-\pi/\omega_R\tau)$ is calculated from the observed lifetimes. The solid line is the expected survival probability $P(N) = [\cos(\frac{\pi}{2N})]^{(2N)}$ for an ideal N measurement QZE.

We quantified the QZE induced by repeated strong measurements. Optical scattering measurement pulses of $172 \mu\text{W}$ ($s_0=0.15$ where $s_0 = I/I_{sat}$ is the saturation parameter or laser intensity relative to saturation intensity) and $10 \mu\text{s}$ in duration were applied to the driven two state system. Each pulse scattered ~ 29 photons per atom. The pulses were separated by a dark free evolution time δt . The lifetime τ for a particular scattering measurement pulse rate $1/\delta t$ was determined by fitting the $|1, -1\rangle$ atom lifetime to an exponential decay curve over a range of times $>\sim 2\tau$. The upper plot in Fig. 2 shows the dramatic increase in the observed lifetimes (solid symbols) as the measurement frequency $1/\delta t$ was increased. The measured lifetimes for two different two photon transition rates ($\omega_R/2\pi = 24.7(0.1)$ Hz triangles, $\omega_R/2\pi = 54.6(0.5)$ Hz boxes) were plotted along with their expected values (upper and lower lines respectively). As expected for the strong measurement regime, the measured lifetimes were not found to be strongly sensitive to variations in optical power, pulse width, or laser detuning. The most frequent measurements (farthest right solid symbols in Fig. 2) show significant deviation from the expected lifetimes (lines). As the measurement frequency was increased the cumulative losses from other processes dominated over the increasingly suppressed QZE related losses. Further increases to the measurement rate would have resulted in a decrease in the measured lifetime. The greatest QZE enhanced lifetime in Fig. 2 (upper left most filled data point) shows an increase by a factor of $\tau\omega_R = 198(16)$ in lifetime at a measurement frequency of $1/\delta t = 25\text{ms}^{-1}$. Other works [5, 16, 18] express the QZE in terms of the survival probability $P(N)$ per number of measurements N during a π pulse ($t = \pi/\omega_R$), a duration where without measurements 100% of the atoms would be transferred into the other state. The lower plot in Fig. 2 translates our observed lifetimes into this generalized basis. In these terms the greatest Zeno effect is for $N=506(2)$ measurements with a survival probability $P=0.984(1)$.

To test the agreement between the predicted QZE and our observations we calculated a corrected QZE lifetime τ_{EP} by subtracting out a separately calibrated scattering measurement loss rate Γ_m . The total observed loss rate $1/\tau$ is split into two components, weighted by the duty cycle $f = 10\mu\text{s}/(10\mu\text{s} + \delta t)$ of the pulsed measurement laser beam. One component accounts for the expected QZE related loss rate $1/\tau_{EP}$ with a weighting $1 - f$. The other component accounts for additional other losses relating to the pulsed measurement process with a rate Γ_m and a weighting f . For all pulsed experiments the measurement laser beam duty cycle $f \leq 20\%$.

$$\frac{1}{\tau} = \frac{1}{\tau_{EP}} (1 - f) + \Gamma_m f \quad (1)$$

Data points in Fig. 2 where this correction had a significant impact on the lifetime are indicated by open symbols. The ideal lifetime would be $\tau_{EP} = 4/(\delta t\omega_R^2)$. We measured $\tau_{EP} = 0.836(0.014) \times 4/(\delta t\omega_R^2)$. Secondary collisions between recoiling, post measurement atoms and the remaining condensate would account for the gap between the

observed and expected lifetimes. Lower magnetic trap depths and stronger scattering measurement laser pulses could reduce these effects. Separate measurement of the additional scattering measurement loss rate Γ_m from the strong scattering measurement pulses showed no change with the removal of the RF component of the driven two photon transition and reduction by an order of magnitude without the microwave component. This suggests that the additional scattering measurement loss mechanism is dominated by two photon scattering through the $|2, 0\rangle$ virtual state to the $5P_{3/2} |3, 0\rangle$ excited state.

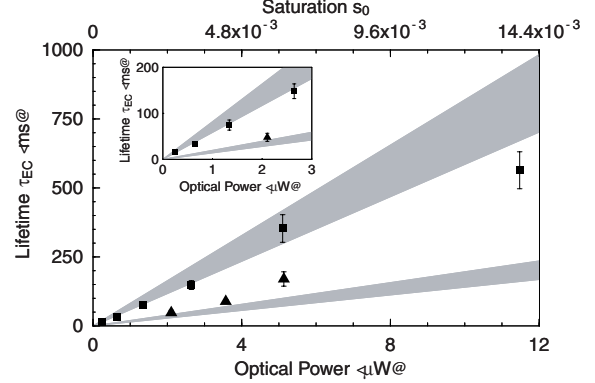


FIG. 3: Continuous QZE lifetime dependence on optical power with $\omega_R/2\pi = 48.5(0.9)$ Hz for laser detunings both on (Boxes) and $\delta_L = -5.4$ MHz off (Triangles) resonance. Grey bands indicates range of expected CW lifetimes from fit to separately measured AC Stark shift for on (upper) and $\delta_L = -5.4$ MHz off (lower) laser detunings. Inset highlights data from lower optical powers. The saturation parameter s_0 scale has an uncertainty of 17%.

In another experiment, the same initial system was subjected to a weak continuous measurement instead of repeated strong measurements. Fig. 3 shows the dramatic increase in lifetime with increasing scattering measurement laser beam power. While showing this qualitative relationship is straightforward, several issues complicate making an quantitative measurement of the continuous QZE. If the scattering measurement laser is detuned from the optical resonance it will have both a reduced scattering rate and also induce an AC Stark Shift δ_{RF} in the two photon resonance, reducing the effective Rabi frequency. In addition, imperfections in the beam can affect the intensity at the atoms. While these are not important for the pulsed measurement so long as the scattering measurement remains in the strong regime, they are critical to properly characterizing the weak continuous measurement experiment.

We were able to address all of these issues simultaneously by measuring the AC Stark shift at several different laser detunings. For each laser detuning δ_L and optical power we determined the AC Stark shift δ_{RF} by maximizing the atom loss as a function of RF frequency. At this point an exponential decay curve was then measured to determine the continuous measurement lifetime τ_{EC} . Fitting the measured AC Stark shifts to the dispersion relation for a multilevel atom [25] we were able to extract in-situ values for the saturation parameter

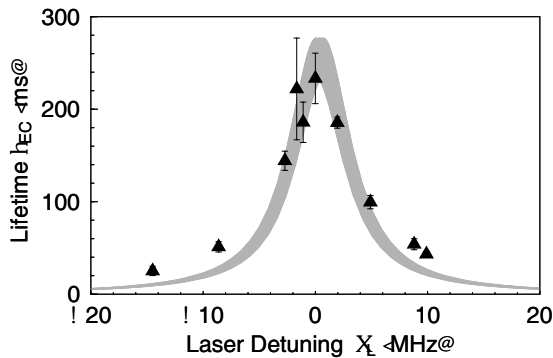


FIG. 4: Continuous quantum Zeno lifetime as a function of the scattering measurement laser detuning δ_L . Grey band indicates range of predicted CW Zeno lifetimes Eq. 2 from separately measured AC Stark shift parameters. Data is for $3.5 \mu\text{W}$ laser power, $\omega_R = 45.5(1.0)$ Hz.

$s_0 = 1.2(0.2) \times 10^{-3}$ at $3.5 \mu\text{W}$ laser power and detuning $\delta_0 = 0.34(0.36)$ MHz. This was in agreement with the values expected from measurements of the laser beam diameter, optical power, and laser frequency stabilization spectroscopy signal. The predicted continuous measurement lifetimes are then given by

$$\tau_{EC} = \frac{\gamma}{\omega_R^2} = \frac{\Gamma s_0}{2\omega_R^2} \left(\frac{1}{1 + 4 \left(\frac{\delta_L - \delta_0}{\Gamma} \right)^2} \right) \quad (2)$$

which are depicted as gray bands in Figs. 3 and 4. Similar to the longest lifetime point in the pulsed data (upper right solid triangle, Fig. 2), the highest power point in Fig. 3 shows significant deviation from the lifetime expected from Eq. 2.

From the AC Stark shift and Eq. 2 we calculate an expected lifetime of $\tau_{EC} = 250(8)$ ms that is in agreement $0.93(0.11)$ with the observed on resonance lifetime $\tau_{EC} = 233(26)$ ms in Fig. 4. The highest power point in Fig. 3 demonstrates a QZE enhancement of lifetime by a factor of $\tau_{EC}\omega_R = 162(20)$. Fig. 3 shows increasing lifetime with increasing measurement laser power, the signature of the continuous QZE. By matching the observed lifetimes for continuous and pulsed QZE measurements we find that $\gamma\delta t = 3.60(0.43)$, in agreement with the predicted ratio of 4 [20].

We have extended previous work in pulsed QZE measurements [5, 18, 19] by exploiting advantages inherent to Bose-Einstein condensates. Complications from an optically dense sample were avoided by working in the frequent measurement regime to prevent appreciable buildup of atoms in the measured state. In ion experiments optical pumping between states during the pulsed laser scattering measurements

changed the observed population [5, 18], requiring significant corrections for the $N=32$ and $N=64$ pulse measurements (Table I, [5]). With corrections on $N=64$ data the greatest survival probability observed was $P(64) = 0.943(20)$ or $\tau_{EP}\omega_R = 54(30)$. Unlike scattering photons off tightly trapped ions, the scattering of a single photon off a weakly trapped ultra-cold atom induces a dramatic and easily distinguishable change in momentum. Furthermore, repeated scatterings increase the momentum and enhance rather than degrade the contrast with unmeasured atoms. QZE experiments of an unstable system involving tunneling measurements of cold neutral atoms in an accelerating lattice [19] observed an increased in survival probability from $P=0.6$ to $P=0.8$ with $N=9$ measurements.

Previous demonstrations of the continuous QZE [11–13, 26] observed qualitative, but not quantitatively characterized suppression effects with increasing laser intensity. In a trapped ion system evolving with free Larmor precession in a magnetic field an $\sim 80\%$ reduction in fluorescence with increasing laser intensity (near and above saturation) was observed [12]. A less comparable continuous QZE system is that observed from molecular collisions in nuclear spin isomer polarized $^{13}\text{CH}_3\text{F}$ gas, where a 60% drop in the conversion rate of gas was observed when the pressure was increased by 12 times [11].

The large hyperfine splitting in ^{87}Rb is favorable for QZE type experiments because it reduces the chance of off resonant scattering of the measurement laser by atoms in the $|1, -1\rangle$ state to 2.8×10^{-7} of that for $|2, +1\rangle$ atoms. Substituting a single photon Rabi oscillation on the $F=1, m_F=0 \leftrightarrow F=2, m_F=0$ clock transition [27] in a low density sample could reduce the systematic limitations observed in this paper relating to the observed additional measurement related losses and collisional losses.

The QZE is closely related to the phenomena of interaction free measurements [28, 29], where information about the state of a system can be determined from the absence rather than presence of a scattering event.

In conclusion we have used a new system to perform QZE measurements deep in the limit of strong suppression. We have measured and quantified the suppression of evolution due both continuous weak measurement and frequent pulsed strong measurement. Our observed quantum Zeno suppressions are larger than both previous pulsed [5] and continuous [12] results, and is also greater than that expected from recently proposed experiments [6, 15, 16, 30]. We observe that the weak continuous measurements exhibit the same suppression in the transition rate as the pulsed measurements when $\gamma\delta t = 3.60(0.43)$. This is in agreement with the previously predicted value of 4 [20]. Initial state lifetimes were increased by factors of $198(16) 1/\omega_R$ in the pulse regime and $172(20) 1/\omega_R$ in the continuous regime.

[1] B. Misra and E. C. G. Sudarshan, J. Math. Phys. **18**, 756 (1977).

[2] S. L. Adler, Phys. Rev. D **67**, 025007 (2003).

- [3] I. L. Egusquiza and L. J. Garay, Phys. Rev. A **68**, 022104 (2003).
- [4] A. Camacho, Intl. J. Mod. Phys. D **10**, 9 (2001).
- [5] W. Itano, D. Heinzen, J. Bollinger, and D. Wineland, Phys. Rev. A **41**, 2295 (1990).
- [6] P. Facchi, Z. Hradil, G. Krenn, S. Pascazio, and J. Rehacek, Phys. Rev. A **66**, 012110 (2002).
- [7] J. D. Franson, B. C. Jacobs, and T. B. Pittman, Phys. Rev. A **70**, 062302 (2004).
- [8] E. Brion, V. M. Akulin, D. Comparat, I. Dumer, G. Harel, N. Kébaïli, G. Kurizki, I. Mazets, and P. Pillet, Phys. Rev. A **71**, 052311 (2005).
- [9] F. M. Spedalieri, H. Lee, M. Florescu, K. T. Kapale, U. Yurtsever, and J. P. Dowling, Opt. Comm **254**, 374 (2005).
- [10] P. Facchi, S. Tasaki, S. Pascazio, H. Nakazato, A. Tokuse, and D. A. Lidar, Phys. Rev. A **71**, 022302 (2005).
- [12] K. Mølhave and M. Drewsen, Phys. Lett. A **268**, 45 (2000).
- [11] B. Nagels, L. J. F. Hermans, and P. L. Chapovsky, Phys. Rev. Lett. **79**, 3097 (1997).
- [13] T. Nakanishi, K. Yamane, and M. Kitano, Phys. Rev. A **65**, 013404 (2001).
- [14] C. Bennett and G. Brassard, in *Proceedings of IEEE International Conference on Computers, Systems, and Signal Processing* (IEEE, New York, USA, 1984), pp. 157–159.
- [15] H. Rauch, Physica B **297**, 299 (2001).
- [16] P. Facchi, Y. Nakaguro, H. Nakazato, S. Pascazio, M. Unoki, and K. Yuasa, Phys. Rev. A **68**, 012107 (2003).
- [17] R. J. Cook, Phys. Scr. **T21**, 29 (1988).
- [18] C. Balzer, T. Hannemann, D. Reib, C. Wunderlich, W. Neuhauser, and P. E. Toschek, Optics Communications **211**, 235 (2002).
- [19] M. C. Fischer, B. Gutiérrez-Medina, and M. G. Raizen, Phys. Rev. Lett. **87**, 040402 (2001).
- [20] L. Schulman, Phys. Lett. A **57**, 1509 (1998).
- [21] E. W. Streed, A. P. Chikkatur, T. L. Gustavson, M. Boyd, Y. Torii, D. Schneble, G. K. Campbell, D. E. Pritchard, and W. Ketterle, cond-mat/0507348 (2005).
- [22] D. Harber, H. Lewandowski, J. McGuirk, and E. Cornell, Phys. Rev. A **66**, 053616 (2002).
- [23] M.-O. Mewes, M. R. Andrews, D. M. Kurn, D. S. Durfee, C. G. Townsend, and W. Ketterle, Phys. Rev. Lett. **78**, 582 (1997).
- [24] E. W. Streed, Ph.D. thesis, Massachusetts Institute of Technology (2006), forthcoming.
- [25] J. Dalibard and C. Cohen-Tannoudji, J. Opt. Soc. Am. B **6**, 2023 (1989).
- [26] P. Valente, H. Failache, and A. Lezama, Phys. Rev. A **65**, 023814 (2002).
- [27] C. Fertig and K. Gibble, Phys. Rev. Lett. **85**, 1622 (2000).
- [28] P. Kwiat, H. Weinfurter, T. Herzog, and A. Zeilinger, Phys. Rev. Lett. **74**, 4763 (1995).
- [29] T. Tsegaye, E. Goobar, A. Karlsson, G. Bjork, M. Y. Loh, and K. H. Lim, Phys. Rev. A **57**, 3987 (1998).
- [30] M. R. Jaekel, E. Jericha, and H. Rauch, Nuc. Inst. Meth. A **539**, 335 (2005).

Appendix D

Degenerate Bose gases in one and two dimensions

The majority of this thesis is about BECs in three dimensional traps. During my course of study we also considered investigating Bose-Einstein condensates in strongly confining systems with fewer degrees of motional freedom. Cold bosons were predicted to undergo very different phase transitions depending on the dimensionality of the system [116–118]. This Appendix contains my notes and calculations regarding these regimes.

Each dimension in an atom trap acts as a quantum harmonic oscillator. A trap frequency ω has an quantized energy spacing between motional states of $\hbar\omega$. Motion in a dimension freezes out when the strong confinement from high trap frequencies causes a quantum of motional energy $\hbar\omega$ to exceed all the other energies in the system. When the chemical potential μ of a BEC is less than a quantum of motional energy $\hbar\omega$ it no longer has enough energy to excite any motion in that direction. Then the ground state of the harmonic oscillator, rather than the mean field energy, dominates the quantum behavior of the BEC. The first notable change is that in the dimensions of strong confinement the profile in ballistic expansion changes from parabolic to Gaussian [119, 120].

D.1 Confinement to one dimension

Consider a cigar shaped trap with tight radial confinement ω_{\perp} in two directions and loose axial confinement ω_z in one direction. This regime has been of theoretical interest for many years [117, 118]. It possible to implement such a system in either a two dimensional optical lattice, creating an array of "needles" or in a Ioffe-Pritchard magnetic trap. Matching the chemical potential to the trapping frequency gives a maximum atom number N_{1D} for one dimensional behavior. In experimental work, the atom number of a tightly confined BEC was reduced by losses over time and dimensional phase change was observed [119] when the atom number fell below critical.

$$N_{1D} < \sqrt{\frac{32\hbar}{225ma^2}} \sqrt{\frac{\omega_{\perp}}{\omega_z^2}} \quad (\text{D.1})$$

1D BECs are not true condensates but are instead quasi-condensates. In a pure 3D BEC the correlation length extends over the entire sample. This can be observed in the interference between two 3D BECs [121]. In a 1D BEC the coherence extends only over part rather than all of the trapped atom sample. While neighbors remain correlated and coherent, the ends of the sample are not. The decreased correlation length is observable as a broadening and change of shape in the Bragg spectroscopy [122] of the BEC's momentum distribution [123].

Another unusual phenomena for strong confinement in two dimensions is that the atom-atom scattering is modified by the trapping potential [124]. These are often referred to as shape resonances. The atom-atom scattering length a changes to

$$a_{eff} = a \frac{1}{1 - 1.032a/a_{\perp}} \quad (\text{D.2})$$

for strong confinement in two dimensions with quantum harmonic oscillator length $a_{\perp} = \sqrt{\frac{\hbar}{m\omega_{\perp}}}$ [125]. For Rb 87, with $a=5.3$ nm, the shape resonance is predicted to occur at trapping frequencies ≈ 4 MHz, much higher than the $\sim 20 - 50$ kHz that has been achieved in optical lattices. Corrections due to changes in the scattering length have been reported at much lower trap frequencies [73].

If we integrate the density in the two tightly confining directions we can define a one dimensional linear density as

$$n_{1D} = \pi a_x a_y n_{3D} \quad (\text{D.3})$$

The one dimensional chemical potential $\mu_{1D} = g_{1D} n_{1D}$ where

$$g_{1D} = \frac{4\hbar^2 a_{eff}}{m a_x a_y} \quad (\text{D.4})$$

and the overall chemical potential $\mu_{3D} = g_{1D} n_{1D} + \hbar\omega_{\perp}$.

D.1.1 Tonks-Girardeau Transition

The Tonks-Girardeau transition occurs when cold atoms are strongly confined in two dimensions such that the atom atom scattering repulsion energy is balanced by a quantum energy cost for knowing the two atoms are separated. The bosons then cease to be degenerate and instead become distinguishable particles, based on their ordered position in the one dimensional line. This state has the surprising property that the strength of its interaction becomes stronger as the system becomes more dilute.

$$\gamma = \frac{E_{uncor}}{4E_{cor}} \quad (\text{D.5})$$

where E_{uncor} is the mean field energy $\mu = g_{1D}n_{1D}$, associated with atoms repelling each other and $E_{cor} = \frac{\hbar^2}{2m}n_{1D}^2$ is the energy associated with the atoms being separated. This has the odd effect of the Tonks-Girardeau parameter γ being greater for lower densities. Very odd for a system to become more strongly interacting as the density drops.

in terms of trap frequencies

$$\gamma \propto \left(\frac{\omega_{\perp}^6}{\omega_z^2} \right)^{1/5} \quad (\text{D.6})$$

$$\gamma = \frac{2a_{eff}}{\pi a_x^2 a_y^2 n_{3D}} \quad (\text{D.7})$$

The effects for the specific case of the crossover from a BEC in a 3D potential to a tightly confining 2D potential has been recently calculated [126] and observed [73, 127–129]. One of the changes in low dimensional behavior is that in the Tonks-Girardeau limit the three atom correlation function $g^{(3)}$ should drop to zero and three body recombination losses should vanish. In preliminary studies the three body loss rate was observed to drop to 15% of the 3D rate [73].

D.2 Confinement to two dimensions

Consider a circular pancake shaped trap with tight confinement ω_z in one directions and loose confinement ω_{\perp} in the other two direction. Two dimensional systems such as these have also been of theoretical interest for many years [117, 118]. They also have practical interest for creating gyroscopic atom interferometers [130] from quantized persistent currents. Systems available for trapping cold atoms in two dimensions include optical lattices [131], and evanescent optical surface traps [132–138], dressed state “egg shell” gravito-magnetic traps [139, 140], and surface magnetic traps [141]. As with the 1D case, preliminary experimental work in an optical trap demonstrated a dimensional phase change [119] when the atom number fell below critical. Matching the chemical potential to the trap frequency energy gives two dimensional behavior when the atom number N is less then

$$N_{2D} < \sqrt{\frac{32\hbar}{225ma^2}} \sqrt{\frac{\omega_z^3}{\omega_{\perp}^4}} \quad (\text{D.8})$$

D.2.1 Berezinskii-Kosterlitz-Thouless Transition

It has been predicted that a trapped, interacting two dimensional Bose gas will undergo two quantum phase transitions as the temperature is reduced [142]. The system becomes superfluid for $T < T_BKT$, the Berezinskii-Kosterlitz-Thouless phase transition [143, 144]. Unlike the 3D case, where superfluidity is a sign that the system has undergone the 3D Bose-Einstein condensate transition, in the 2D case the system is not required to have long range order, making it instead a quasi-condensate. The trapped atoms are predicted to have

”patches” of phase coherence of size equal to the correlation length. As the temperature is lowered this correlation length grows until it encompasses the entire finite sample. A second, Bose-Einstein condensate like phase transition is predicted to occur at this point.

Unlike the one dimensional case, experiments have been performed in thin films of liquid Helium [145,146] and hydrogen [147]. The superfluid transition was observed in liquid helium through studies of rotational inertia [145,146] and optical polarization [148] properties. Further evidence of a quantum phase transition is the reduction in the three body recombination rate for a 2D hydrogen gas was also observed [147]. To date this phenomena has not been observed in cold alkali gases. The BKT transition temperature is purely a function of the surface mass density

$$k_B T_{BKT} = \frac{\pi \hbar^2}{2m} n_{surface} \quad (D.9)$$

In a harmonic trap with a finite number of particles the transition temperature is then

$$k_B T_{BKT} \approx 0.44 \hbar \omega_{\parallel} N^{1/2} \quad (D.10)$$

For comparison the three dimension Bose-Einstein condensate transition temperature is

$$k_B T_c \approx 0.94 \hbar \bar{\omega} N^{1/3} \quad (D.11)$$

The wavefunction of a BEC is

$$\psi(x, y, z) = \sqrt{n(x, y, z)} \exp(i\mu/\hbar t) \quad (D.12)$$

where in 2 dimensions

$$n(x, y, z) = n_p^{3D} \left(1 - \frac{x^2}{r_x^2} - \frac{y^2}{r_y^2} \right) \exp^{-z^2/a_z^2} \quad (D.13)$$

Integrating in all three directions we can determine the total atom number

$$N = n_p^{3D} \frac{\pi}{2} r_x r_y \sqrt{\pi} a_z \quad (D.14)$$

$$N = \frac{\pi}{2} r_x r_y n_p^{2D} \quad (D.15)$$

instead of the usual 3D result

$$N = n_p^{3D} \frac{8\pi}{15} r_x r_y r_z \quad (D.16)$$

The two dimensional mean field energy is then

$$\mu_{2D} = \frac{4\pi \hbar^2 a}{m a_z \sqrt{\pi}} n_p^{2D} \quad (D.17)$$

and using the Thomas Fermi criteria that $\mu_{2D} = \frac{1}{2}m\omega_i^2 r_i^2$ we can determine

$$\mu_{2D} = \frac{1}{2}\hbar\omega_{2D}\sqrt{\frac{16aN}{a_z\sqrt{\pi}}} \quad (\text{D.18})$$

and

$$n_p^{2D} = \frac{1}{\bar{a}_{2D}^2}\sqrt{\frac{N}{4\pi^{3/2}}\frac{a_z}{a}} \quad (\text{D.19})$$

Similar to the 1D case, the overall chemical potential is the reduced dimensionality potential plus the harmonic oscillator energy in the frozen direction.

$$\mu_{3D} = \mu_{2D} + \hbar\omega_{\perp}/2 \quad (\text{D.20})$$

Appendix E

Rubidium Properties

E.1 Physical Properties of Rubidium

Rubidium is an extremely reactive silvery white metal which melts a few degrees above body temperature (39.31 ° C,103 °F). Upon contact with water it liberates hydrogen gas and forms the caustic base rubidium hydroxide. 28% of naturally occurring rubidium is ^{87}Rb . A β^- emitter with a half life of 50 billion years, ^{87}Rb is not considered to be a radiological hazard. The radioactivity level of naturally occurring rubidium is similar to that of potassium. The potassium in a 5 lb sack of potatoes has greater radioactivity than that from a 5 gm ampoule of rubidium.

Reactivity

Compound	State	Color	$\Delta H_{formation}$ (kJ/mol)	$\Delta H_{solution}$ (kJ/mol)
RbOH	solid	white	424	60
Rb ₂ O	solid	black	347	
Rb ₂ O ₂	solid	yellow	448	
Rb ₂ O ₄	solid	orange	565	
H ₂ O	liquid	clear	286	
H ₂ O	gas	clear	242	

Table E.1: Energy released from formation of select compounds from their constituent elements.

From table E.1 we can calculate that 5 gm of Rb reacting with humid air will liberate 17 kJ.

Toxicity

Rb metal is highly reactive and will form alkaline salts upon exposure to air or water. As of 2002 no toxicity data specific to Rb metal was obtainable through conventional searches. The product Rb salts have toxicities (LD50) comparable to their Na counterparts.

Disposal

Rb metal is a hazardous material and should be disposed of by professionals. Rb salts are less hazardous than Rb metal and may be classified as “sinkable”. Please consult your local environmental safety officer for current regulations.

E.1.1 Vapor Pressure

The saturated vapor pressure of rubidium as a function of temperature (Fig. E-1) is an important parameter in the design of atomic beam ovens and spectroscopy cells. Two formulas are commonly used to calculate the vapor pressure. One is based on experimental measurements of the vapor pressure [52] while the other is a theoretical curve which incorporates various physical measurements of rubidium [149].

The simple formula given by [52] provides the pressure in atmospheres as a function of the temperature in Kelvin. The formula is only considered valid for temperatures above room temperature, although it agrees with the results from [149] down to much lower temperatures.

$$\log_{10} P = A + B/T \tag{E.1}$$

State	A	B (K)	Temp Range (K)
solid	4.857	-4215	298-312
liquid	4.312	-4040	312-600

Table E.2: Constants for Rubidium vapor pressure formula [52]

The much more elaborate formula of [149] gives the pressure in torr as a function of the temperature in Kelvin. Values for the vapor pressure of Rb_2 molecules are also included.

$$\log_{10} P = A - B/T + CT + D\log_{10}T \tag{E.2}$$

E.1.2 Spectroscopy Cell Maintenance

We use the absorption signal from rubidium spectroscopy cells is used to stabilize laser frequencies to resonances in ^{87}Rb . The absorption signal is proportional to the density of rubidium vapor in the cell. In a good room temperature cell 50 mm long the typical optical

State	A	B (K)	C (/K)	D	Temp Range (K)
solid Rb	-94.04826	1961.258	-0.03771687	42.57526	<312
liquid Rb	15.88253	4529.635	0.00058663	-2.99138	>312
solid Rb ₂	-211.33010	966.918	-0.07829240	91.59149	<312
liquid Rb ₂	41.27530	7226.316	0.00333213	-11.85510	>312

Table E.3: Constants for extended Rubidium vapor pressure formula [149]

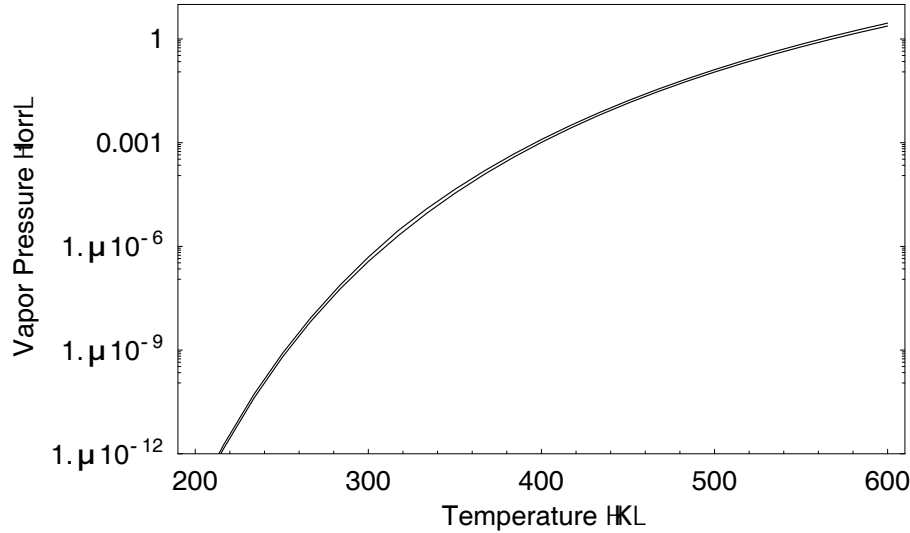


Figure E-1: Saturated vapor pressure of rubidium as a function of temperature. Upper curve is from [52]. Lower curve is from [149]

density is $\sim 30\%$ when Doppler broadening is included. The partial pressure of rubidium in the cell is saturated when exposed rubidium metal or liquid is in equilibrium with the vapor phase. Rubidium also acts as a getter vacuum pump, reacting with oxygen and water which may leak into the cell. Over time a layer of surface oxide and hydroxide salts can build up over exposed rubidium metal, reducing the amount of metal available to maintain the saturated vapor equilibrium. After several years the absorption of optical cells can be reduced because of the covering of the rubidium metal with this salt layer. These salts are easily recognizable by their dull gray appearance.

Old cells often have usable quantities of Rb metal buried under this layer of salts. To make a fresh layer of Rb metal in the cell, heat a bowl of water to $\sim 50^\circ\text{C}$ and float the cell in it. You will see a diffuse line layer of Rb metal forming above the water line, where Rb metal is condensing on the coldest surface. In cells with an appreciable (mg) amount of Rb, it may visibly bead up, sluffing off salt flakes. This procedure will restore the saturated vapor pressure in the cell and improve the absorption signal.

Caution: DO NOT USE BOILING WATER The low melting point of rubidium

metal means that water which is warm to the touch is sufficient. Adverse thermal stress on glass cells can cause them to shatter. The rapid production of flying glass shards in the lab is inadvisable.

Bibliography

- [1] F. Gregoire, S. Wei, E. W. Streed, K. Brameld, D. Fort, L. Hanely, J. Walls, W. Goddard, and J. Roberts, “Conformational equilibria of beta-alanine and related compounds as studied by NMR spectroscopy,” *J. Am. Chem. Soc.* **120**, 7537 (1998).
- [2] J. W. Jr., “The dielectric constant of mixtures of ethyl alcohol and water from -5 to 40°,” *J. Amer. Chem. Soc.* **53**, 3292 (1931).
- [3] A. Einstein, *Sitzber. Kgl. Preuss. Akad. Wiss.* **261**, (1924).
- [4] S. Bose, “Plancks Gesetz und Lichtquantenhypothese,” *Z. Phys.* **26**, 178 (1924).
- [5] L. de Broglie, “Recherches sur la Theorie des Quanta,” *Ann. Phys. (Fr.)* **3**, 22 (1925).
- [6] W. Phillips and H. Metcalf, “Laser deceleration of an atomic beam,” *Phys. Rev. Lett.* **48**, 596 (1982).
- [7] S. Chu, L. Hollberg, J. Bjorkholm, A. Cable, and A. Ashkin, “Three-Dimensional Viscous Confinement and Cooling of Atoms by Resonance Radiation Pressure,” *Phys. Rev. Lett.* **55**, 48 (1985).
- [8] S. Chu, J. Bjorkholm, A. Ashkin, and A. Cable, “Experimental observation of optically trapped atoms,” *Phys. Rev. Lett.* **57**, 314 (1986).
- [9] E. Raab, M. Prentiss, A. Cable, S. Chu, and D. Pritchard, “Trapping of Neutral Sodium Atoms with Radiation Pressure,” *Phys. Rev. Lett.* **59**, 2631 (1987).
- [10] A. Aspect, E. Arimondo, R. Kaiser, N. Vansteenkiste, and C. Cohen-Tannoudji, “Laser Cooling Below the One-Photon Recoil Energy by Velocity-Selective Coherent Population Trapping,” *Phys. Rev. Lett.* **61**, 826 (1988).
- [11] P. Lett, R. Watts, C. Westbrook, W. Phillips, P. Gould, and H. Metcalf, “Observation of atoms laser cooled below the Doppler limit,” *Phys. Rev. Lett.* **61**, 169 (1988).
- [12] D. Weiss, E. Riis, Y. Shevy, P. Ungar, and S. Chu, “Optical molasses and multilevel atoms: experiment,” *J. Opt. Soc. Am. B* **6**, 2072 (1989).
- [13] P. Lett, W. Phillips, S. Rolston, C. Tanner, and R. W. C. Westbrook, “Optical Molasses,” *J. Opt. Soc. Am. B* **6**, 2084 (1989).
- [14] C. N. Cohen-Tannoudji, “Manipulating atoms with photons (Nobel lecture),” *Rev. Mod. Phys.* **70**, 707 (1998).

- [15] S. Chu, “The manipulation of neutral particles (Nobel lecture),” *Rev. Mod. Phys.* **70**, 685 (1998).
- [16] W. D. Phillips, “Laser cooling and trapping of neutral atoms (Nobel lecture),” *Rev. Mod. Phys.* **70**, 721 (1998).
- [17] E. A. Cornell and C. E. Wieman, “Nobel Lecture: Bose-Einstein condensation in a dilute gas, the first 70 years and some recent experiments,” *Rev. Mod. Phys.* **74**, 875 (2002).
- [18] W. Ketterle, “When atoms behave as waves: Bose-Einstein condensation and the atom laser,” *Rev. Mod. Phys.* **74**, 1131 (2002).
- [19] M. H. Anderson, J. R. Ensher, M. R. Matthews, C. E. Wieman, and E. A. Cornell, “Observation of Bose-Einstein Condensation in a Dilute Atomic Vapor,” *Science* **269**, 198 (1995).
- [20] K. B. Davis, M.-O. Mewes, M. R. Andrews, N. J. van Druten, D. S. Durfee, D. M. Kurn, and W. Ketterle, “Bose-Einstein Condensation in a Gas of Sodium Atoms,” *Phys. Rev. Lett.* **75**, 3969 (1995).
- [21] C. C. Bradley, C. A. Sackett, J. J. Tollett, and R. G. Hulet, “Evidence of Bose-Einstein Condensation in an Atomic Gas with Attractive Interactions,” *Phys. Rev. Lett.* **75**, 1687 (1995), *ibid.* **79**, 1170 (1997).
- [22] C. Bradley, C. Sackett, and R. Hulet, “Bose-Einstein condensation of Lithium: Observation of Limited Condensate Number,” *Phys. Rev. Lett.* **78**, 985 (1997).
- [23] D. Fried, T. Killian, L. Willmann, D. Landhuis, S. Moss, D. Kleppner, and T. Greytak, “Bose-Einstein condensation of atomic hydrogen,” *Phys. Rev. Lett.* **81**, 3811 (1998).
- [24] S. Cornish, N. Claussen, J. Roberts, E. Cornell, and C. Wieman, “Stable ^{85}Rb Bose-Einstein condensation with widely tunable interactions,” *Phys. Rev. Lett.* **85**, 1795 (2000).
- [25] A. Roberts, O. Sirjean, A. Browaeys, J. Poupard, S. Nowak, D. Boiron, C. Westbrook, and A. Aspect, “A Bose-Einstein condensation of metastable atoms,” *Science* **292**, 461 (2001).
- [26] F. Santos, J. Wang, C. Barrelet, F. Perales, E. Rasel, C. Unnikrishnan, M. Leduc, and C. Cohen-Tannoudji, “Bose-Einstein condensation of metastable Helium,” *Phys. Rev. Lett.* **86**, 3459 (2001).
- [27] G. Modugno, G. Ferrari, G. Roati, R. Brecha, A. Simoni, and M. Inguscio, “Bose-Einstein condensation of Potassium atoms by sympathetic cooling,” *Science* **294**, 1320 (2001).
- [28] T. Weber, J. Herbig, M. Mark, H. Nagerl, and R. Grimm, “Bose-Einstein condensation of Cesium,” *Science* **294**, 232 (2003).
- [29] Y. Takasu, K. Maki, K. Komori, T. Takano, K. Honda, M. Kumakura, T. Yabuzaki, and Y. Takahashi, “Spin-singlet Bose-Einstein condensation of two-electron atoms,” *Phys. Rev. Lett.* **91**, 030404 (2003).

- [30] A. Griesmaier, J. Werner, S. Hensler, J. Stuhler, and T. Pfau, “Bose-Einstein condensation of Chromium,” *Phys. Rev. Lett.* **94**, 160401 (2005), cond-mat/0503044.
- [31] H. Ott, J. Fortagh, G. Schlotterbeck, A. Grossmann, and C. Zimmermann, “Bose-Einstein Condensation in a surface micro trap,” *Phys. Rev. Lett.* **87**, 230401 (2001).
- [32] K. Dieckmann, R. J. C. Spreeuw, M. Weidemüller, and J. T. M. Walraven, “Two-dimensional magneto-optical trap as a source of slow atoms,” *Phys. Rev. A* **226**, 3891 (1998).
- [33] R. S. Conroy, Y. Xiao, M. Vengalattore, W. Rooijackers, and M. Prentiss, “Compact, robust source of cold atoms for efficient loading of a magnetic guide,” *Opt. Comm.* **226**, 259 (2003), physics/0308108.
- [34] H. Lewandowski, D. Harber, D. Whitaker, and E. Cornell, “Simplified system for Creating a Bose-Einstein condensate,” *J. Low Temp Phys* **132**, 309 (2003).
- [35] T. Gustavson, A. Chikkatur, A. Leanhardt, A. Görlitz, S. Gupta, D. Pritchard, and W. Ketterle, “Transport of Bose-Einstein Condensates with Optical Tweezers,” *Phys. Rev. Lett.* **88**, 020401 (2002).
- [36] A. E. Leanhardt, A. P. Chikkatur, D. Kielpinski, Y. Shin, T. L. Gustavson, W. Ketterle, and D. E. Pritchard, “Propagation of Bose-Einstein Condensates in a Magnetic Waveguide,” *Phys. Rev. Lett.* **89**, 040401 (2002).
- [37] A. P. Chikkatur, Y. Shin, A. E. Leanhardt, D. Kielpinski, E. Tsikata, T. L. Gustavson, D. E. Pritchard, and W. Ketterle, “A Continuous Source of Bose-Einstein Condensed Atoms.,” *Science* **296**, 2193 (2002).
- [38] A. E. Leanhardt, T. A. Pasquini, M. Saba, A. Schirotzek, Y. Shin, D. Kielpinski, D. E. Pritchard, and W. Ketterle, “Adiabatic and Evaporative Cooling of Bose-Einstein condensates below 500 Picokelvin.,” *Science* **301**, 1513 (2003).
- [39] A. E. Leanhardt, Y. Shin, A. P. Chikkatur, D. Kielpinski, W. Ketterle, and D. E. Pritchard, “Bose-Einstein Condensates near a Microfabricated Surface,” *Phys. Rev. Lett.* **90**, 100404 (2003).
- [40] Y. Shin, M. Saba, M. Vengalattore, T. A. Pasquini, C. Sanner, A. E. Leanhardt, M. Prentiss, D. E. Pritchard, and W. Ketterle, “Dynamical Instability of a Doubly Quantized Vortex in a Bose-Einstein condensate.,” *Phys. Rev. Lett.* **93**, 160406 (2004).
- [41] T. Pasquini, Y. Shin, C. Sanner, M. Saba, A. Schirotzek, D. Pritchard, and W. Ketterle, “Quantum reflection of atoms from a solid surface at normal incidence.,” *Phys. Rev. Lett.* **93**, 223201 (2004).
- [42] Y. Shin, M. Saba, A. Schirotzek, T. A. Pasquini, A. E. Leanhardt, D. E. Pritchard, and W. Ketterle, “Distillation of Bose-Einstein condensates in a double-well potential.,” *Phys. Rev. Lett.* **92**, 150401 (2004).
- [43] Y. Shin, M. Saba, T. Pasquini, W. Ketterle, D. Pritchard, and A. Leanhardt, “Interferometry in a double-well potential.,” *Phys. Rev. Lett.* **92**, 050405 (2004).

- [44] D. Schneble, Y. Torii, M. Boyd, E. Streed, D. E. Pritchard, and W. Ketterle, “The Onset of Matter-Wave Amplification in a Superradiant Bose-Einstein Condensate,” *Science* **300**, 475 (2003).
- [45] D. Schneble, G. K. Campbell, E. W. Streed, M. Boyd, D. E. Pritchard, and W. Ketterle, “Raman amplification of matter waves,” *Phys. Rev. A* **69**, 041601 (2004).
- [46] G. Campbell, A. E. Leanhardt, J. Mun, M. Boyd, E. Streed, D. Pritchard, and W. Ketterle, “Photon recoil momentum in Dispersive media,” *Phys. Rev. Lett.* **94**, 170403 (2005).
- [47] J. O’Hanlon, *A user’s guide to vacuum technology* (Wiley-Interscience, Hoboken, NJ, 1989).
- [48] E. W. Streed, A. P. Chikkatur, T. L. Gustavson, M. Boyd, Y. Torii, D. Schneble, G. K. Campbell, D. E. Pritchard, and W. Ketterle, “Large atom number Bose-Einstein Condensate machines,” *cond-mat/0507348* (2005).
- [49] A. P. Chikkatur, Ph.D. thesis, Massachusetts Institute of Technology, 2002, http://cua.mit.edu/ketterle_group/Theses/thesis_APC.pdf.
- [50] H. Pauly and C. Scoles, *Atomic and Molecular Beam methods Vol I.* (Oxford University Press, Oxford, 1988), p. 83.
- [51] D. Steck, “Sodium D Line Data,” <http://steck.us/alkalidata/sodiumnumbers.pdf> (2003).
- [52] C. Alcock, V. Itkin, and M. Horrigan, “Vapor-pressure equations for the metallic elements- 298-2500 K,” *Canadian Metallurgical Quarterly* **23**, 309 (1984).
- [53] H. Gray, *Chemical Bonds* (University Science Books, Mill Valley, CA, 1994), p. 44.
- [54] M. Walkiewicz, P. Fox, and R. Scholten, “Candlestick rubidium beam source,” *Rev. Sci. Instr.* **71**, 3342 (2000).
- [55] H. Metcalf and P. van der Straten, *Laser Cooling and Trapping, Graduate texts in contemporary physics* (Springer-Verlag, New York, 1999).
- [56] T. Barrett, S. Daporeschwartz, M. Ray, and G. Lafyatis, “Slowing atoms with (sigma(-))-polarized light,” *Phys. Rev. Lett.* **67**, 3483 (1991).
- [57] C. Slowe, L. Vernac, and L. V. Hau, “High flux source of cold rubidium atoms,” *Rev. Sci. Instr.* **76**, 103101 (2005).
- [58] Y. Yoshikawa, T. Umeki, T. Mukae, Y. Torii, and T. Kuga, “Frequency stabilization of a laser diode with use of light induced birefringence in an atomic vapor,” *Appl. Opt.* **42**, 6645 (2003).
- [59] C. Pearman, C. Adams, S. Cox, P. Griffin, D. Smith, and I. Hughs, “Polarization spectroscopy of a closed atomic transition: applications to laser frequency locking,” *J. Phys. B* **35**, 5141 (2002).
- [60] A. Siegman, *Lasers* (University Science Books, Sausalito, CA, 1986).

- [61] H. Moosmüller and J. Vance, “Sum-frequency generation of continuous-wave sodium D₂ resonance radiation,” *Optics Lett.* **22**, 1135 (1997).
- [62] J. Bienfang, C. A. Denman, B. W. Grime, P. D. Hillman, G. T. Moore, and J. M. Telle, “20 W of continuous-wave sodium D₂ resonance radiation from sum-frequency generation with injection locked lasers,” *Optics Lett.* **28**, 2219 (2003).
- [63] R. J. Thompson, M. Tu, D. C. Aveline, N. Lundblad, and L. Maleki, “High power single frequency 780nm laser source generated from frequency doubling of a seeded fiber amplifier in a cascade of PPLN crystals,” *Optics Express* **11**, 1709 (2003).
- [64] Y. Castin and R. Dum, “Bose-Einstein condensates in time dependent traps,” *Phys. Rev. Lett.* **77**, 5315 (1996).
- [65] W. Ketterle, K. Davis, M. Joffe, A. Martin, and D. Pritchard, “High Densities of Cold Atoms in a Dark Spontaneous-Force Atom Trap,” *Phys. Rev. Lett.* **70**, 2253 (1993).
- [66] S. Shang, B. Sheehy, P. van der Straten, and H. Metcalf, “Velocity-selective magnetic resonance laser cooling,” *Phys. Rev. Lett.* **67**, 1094 (1991).
- [67] T. Bergeman, G. Erez, and H. J. Metcalf, “Magnetostatic trapping fields for neutral atoms,” *Phys. Rev. A* **35**, 1535 (1987).
- [68] S. Inouye, A. P. Chikkatur, D. M. Stamper-Kurn, J. Stenger, D. E. Pritchard, and W. Ketterle, “Superradiant Rayleigh Scattering from a Bose-Einstein Condensate,” *Science* **285**, 571 (1999).
- [69] D. Montgomery, *Solenoid magnet design; the magnetic and mechanical aspects of resistive and superconducting systems* (Wiley-Interscience, New York, 1969).
- [70] T. NESLAB, “System III Liquid to Liquid Heat Exchanger,” Thermo NESLAB Manual P/N 013736 Rev 11/07/00 15 (2000).
- [71] W. Ketterle, D. S. Durfee, and D. M. Stamper-Kurn, in Bose-Einstein Condensation in Atomic Gases, *Proceedings of the International School of Physics “Enrico Fermi” Course CXL*, edited by M. Inguscio, S. Stringari, and C. E. Wieman (IOS Press Amsterdam, ADDRESS, 1999), cond-mat/9904034.
- [72] D. S. Durfee, Ph.D. thesis, Massachusetts Institute of Technology, 1999, <http://www.physics.byu.edu/faculty/durfee/DSDThesis.pdf>.
- [73] B. Tolra, K. O’Hara, J. Huckans, W. Phillips, S. Rolston, and J. Porto, “Observation of Reduced Three-Body Recombination in a Fermionized 1D Bose Gas,” *Phys. Rev. Lett.* **92**, 190401 (2003).
- [74] A. Görlitz, T. Gustavson, A. Leanhardt, R. Low, A. Chikkatur, S. Gupta, S. Inouye, D. Pritchard, and W. Ketterle, “Sodium Bose-Einstein condensates in the F=2 state in a large volume optical trap,” *Phys. Rev. Lett.* **90**, 090401 (2003).
- [75] D. Harber, H. Lewandowski, J. McGuirk, and E. Cornell, “Effect of cold collisions on spin coherence and resonance shifts in a magnetically trapped ultracold gasy,” *Phys. Rev. A* **66**, 053616 (2002).

- [76] C. Samuelis, E. Tiesinga, T. Laue, M. Elbs, H. Knockel, and E. Tiemann, “Cold atomic collisions studied by molecular spectroscopy,” *Phys. Rev. A* **63**, 012710 (2000).
- [77] D. Steck, “Rubidium 87 D Line Data,” <http://steck.us/alkalidata/rubidium87numbers.pdf> (2002).
- [78] B. Borca, J. W. Dunn, V. Kokoouline, and C. H. Greene, “Atom-Molecule Laser fed by Stimulated Three-Body recombination,” *Phys. Rev. Lett.* **91**, 070404 (2003).
- [79] J. Schuster, A. Marte, S. Amthage, B. Sang, G. Rempe, and H. C. W. Beijerinck, “Avalanches in a Bose-Einstein condensate,” *Phys. Rev. Lett.* **87**, 170404 (2001).
- [80] E. A. Burt, R. W. Ghrist, C. J. Myatt, M. J. Holland, E. A. Cornell, , and C. E. Wieman, “Coherence, Correlations, and Collisions: What One Learns about Bose-Einstein Condensates from Their Decay,” *Phys. Rev. Lett.* **79**, 337 (1997).
- [81] B. Misra and E. C. G. Sudarshan, “The Zeno paradox in quantum theory,” *J. Math. Phys.* **18**, 756 (1977).
- [82] W. Itano, D. Heinzen, J. Bollinger, and D. Wineland, “Quantum Zeno effect,” *Phys. Rev. A* **41**, 2295 (1990).
- [83] R. J. Cook, “What are quantum jumps,” *Phys. Scr.* **T21**, 29 (1988).
- [84] C. Balzer, T. Hannemann, D. Reib, C. Wunderlich, W. Neuhauser, and P. E. Toschek, “A relaxationless demonstration of the Quantum Zeno paradox on an individual atom,” *Optics Communications* **211**, 235 (2002).
- [85] M. C. Fischer, B. Gutiérrez-Medina, and M. G. Raizen, “Observation of the quantum zeno and anti-zeno effects in an unstable system,” *Phys. Rev. Lett.* **87**, 040402 (2001).
- [86] B. Nagels, L. J. F. Hermans, and P. L. Chapovsky, “Quantum Zeno Effect induced by collisions,” *Phys. Rev. Lett.* **79**, 3097 (1997).
- [87] K. Mølhave and M. Drewsen, “Demonstration of the continuous quantum Zeno effect in optical pumping,” *Phys. Lett. A* **268**, 45 (2000).
- [88] T. Nakanishi, K. Yamane, and M. Kitano, “Absorption-free optical control of spin systems: The quantum Zeno effect in optical pumping,” *Phys. Rev. A* **65**, 013404 (2001).
- [89] P. Valente, H. Failache, and A. Lezama, “Comparative study of the transient evolution of Hanle electromagnetically induced transparency and absorption resonances,” *Phys. Rev. A* **65**, 023814 (2002).
- [90] S. L. Adler, “Weisskopf-Wigner decay theory for the energy-driven stochastic Schrodinger equation,” *Phys. Rev. D* **67**, 025007 (2003).
- [91] I. L. Egusquiza and L. J. Garay, “Real clocks and the Zeno effect,” *Phys. Rev. A* **68**, 022104 (2003).
- [92] A. Camacho, “Quantum Zeno effect and the detection of gravitomagnetism,” *Intl. J. Mod. Phys. D* **10**, 9 (2001).

- [93] O. Alter and Y. Yamamoto, “Fundamental quantum limit to external force detection via monitoring a single harmonic oscillator or free mass,” *Phys. Lett. A* **263**, 226 (1999).
- [94] J. D. Franson, B. C. Jacobs, and T. B. Pittman, “Quantum computing using single photons and the Zeno effect,” *Phys. Rev. A* **70**, 062302 (2004).
- [95] E. Brion, V. M. Akulin, D. Comparat, I. Dumer, G. Harel, N. Kébaili, G. Kurizki, I. Mazets, and P. Pillet, “Coherence protection by the quantum Zeno effect and non-holonomic control in a Rydberg rubidium isotope,” *Phys. Rev. A* **71**, 052311 (2005).
- [96] F. M. Spedalieri, H. Lee, M. Florescu, K. T. Kapale, U. Yurtsever, and J. P. Dowling, “Exploiting the Quantum Zeno effect to beat photon loss in linear optical quantum information processor,” *Opt. Comm* **254**, 374 (2005).
- [97] P. Facchi, S. Tasaki, S. Pascazio, H. Nakazato, A. Tokuse, and D. A. Lidar, “Control of decoherence: Analysis and comparison of three different strategies,” *Phys. Rev. A* **71**, 022302 (2005).
- [98] C. Bennett and G. Brassard, in *Proceedings of IEEE International Conference on Computers, Systems, and Signal Processing* (IEEE, New York, USA, ADDRESS, 1984), pp. 157–159.
- [99] P. Kwiat, H. Weinfurter, T. Herzog, and A. Zeilinger, “Interaction-Free Measurement,” *Phys. Rev. Lett.* **74**, 4763 (1995).
- [100] T. Tsegaye, E. Goobar, A. Karlsson, G. Bjork, M. Y. Loh, and K. H. Lim, “Efficient interaction-free measurements in a high finesse interferometer,” *Phys. Rev. A* **57**, 3987 (1998).
- [101] P. Facchi, Z. Hradil, G. Krenn, S. Pascazio, and J. Rehacek, “Quantum zeno tomography,” *Phys. Rev. A* **66**, 012110 (2002).
- [102] R. Mair and R. Walsworth, “Novel MRI Applications of Laser-Polarized Noble Gases,” *App. Mag. Res.* **22**, 159 (2005).
- [103] R. Mair, M. Hrovat, S. Patz, M. Rosen, I. Ruset, G. Topulos, L. Tsai, J. Butler, F. Hersman, and R. Walsworth, “A System for Open-Access ^3He Human Lung Imaging at Very Low Field pdf icon submitted to *Journal of Magnetic Resonance*,” *Mag. Res. Med.* **53**, 745 (2005).
- [104] H. Rauch, “Quantum Zeno effect with polarized neutrons,” *Physica B* **297**, 299 (2001).
- [105] P. Facchi, Y. Nakaguro, H. Nakazato, S. Pascazio, M. Unoki, and K. Yuasa, “Optimization of a neutron-spin test of the quantum Zeno effect,” *Phys. Rev. A* **68**, 012107 (2003).
- [106] M.-O. Mewes, M. R. Andrews, D. M. Kurn, D. S. Durfee, C. G. Townsend, and W. Ketterle, “Output Coupler for Bose-Einstein Condensed Atoms,” *Phys. Rev. Lett.* **78**, 582 (1997).
- [107] C. Fertig and K. Gibble, “Measurement and cancellation of the cold collision frequency shift in a ^{87}Rb fountain clock,” *Phys. Rev. Lett.* **85**, 1622 (2000).

- [108] P. J. Mohr and B. N. Taylor, “CODATA recommended values of the fundamental physical constants: 1998,” *Rev. Mod. Phys.* **72**, 351 (1998).
- [109] S. Bize, Y. Sortais, M. S. Santos, C. Mandache, A. Clairon, and C. Salomon, “High accuracy measurement of the ^{87}Rb ground state hyperfine splitting in an atomic fountain,” *Europhys. Lett.* **45**, 588 (1999).
- [110] E. Arimondo, M. Inguscio, and P. Violino, “Experimental determination of the hyperfine structure in the alkali atoms,” *Rev. Mod. Phys.* **49**, 31 (1977).
- [111] L. Schulman, “Continuous and pulsed observations in the quantum Zeno effect,” *Phys. Lett. A* **57**, 1509 (1998).
- [112] J. Dalibard and C. Cohen-Tannoudji, “Laser cooling below the Doppler limit by polarization gradients: simple theoretical models,” *J. Opt. Soc. Am. B* **6**, 2023 (1989).
- [113] E. M. Lifshitz and L. D. Landau, *Quantum Mechanics: Non-Relativistic Theory, Volume 3* (Butterworth-Heinemann, ADDRESS, 1981).
- [114] P. S. Julienne and J. Vigue, “Cold collisions of ground- and excited-state alkali-metal atoms,” *Phys. Rev. A* **44**, 4464 (1991).
- [115] M. R. Jaekel, E. Jericha, and H. Rauch, “New developments in cold neutron storage with perfect crystals,” *Nuc. Inst. Meth. A* **539**, 335 (2005).
- [116] V. Bagnato and D. Kleppner, “Bose-Einstein condensation in low-dimensional traps,” *Phys. Rev. A* **44**, 7439 (1991).
- [117] E. Lieb and W. Linger, “Exact analysis of an interacting Bose Gas. I. The general solution and the ground state,” *Phys. Rev.* **130**, 1605 (1963).
- [118] E. Lieb, “Exact analysis of an interacting Bose Gas. II. The excitation spectrum,” *Phys. Rev.* **130**, 1616 (1963).
- [119] A. Görlitz, J. M. Vogels, A. E. Leanhardt, C. Raman, T. L. Gustavson, J. R. Abo-Shaer, A. P. Chikkatur, S. Gupta, S. Inouye, T. P. Rosenband, D. E. Pritchard, and W. Ketterle, “Realization of Bose-Einstein condensates in lower dimensions,” *Phys. Rev. Lett.* **87**, 130402 (2001).
- [120] Karnachatnov, “Expansion of a Bose-Einstein condensate in lower dimensions,” *JETP* **98**, 908 (2003).
- [121] M. Andrews, C. Townsend, H.-J. Miesner, D. Durfee, D. Kurn, and W. Ketterle, “Observation of Interference Between Two Bose-Einstein Condensates,” *Science* **275**, 637 (1997).
- [122] J. Stenger, S. Inouye, A. P. Chikkatur, D. M. Stamper-Kurn, D. E. Pritchard, and W. Ketterle, “Bragg Spectroscopy of a Bose-Einstein Condensate,” *Phys. Rev. Lett.* **82**, 4569 (1999).
- [123] S. Richard, F. Gerbier, J. H. Thywissen, M. Hugbart, P. Bouyer, and A. Aspect, “Momentum spectroscopy of phase fluctuations of 1D phase fluctuations in Bose-Einstein condensate,” *Phys. Rev. Lett* **91**, 010405 (2003).

- [124] M. Olshanii, “Atomic Scattering in the Presence of an External Confinement and a Gas of Impenetrable Bosons,” *Phys. Rev. Lett.* **81**, 938 (1998).
- [125] M. Olshanii, “Atomic Scattering in the Presence of an external confinement and a gas of impenetrable bosons,” *Phys. Rev. Lett.* **81**, 938 (1998).
- [126] M. D. Girardeau and E. M. Wright, “Bose-Fermi variational Theory of the Bose-Einstein condensate crossover to the Tonks gas,” *Phys. Rev. Lett.* **87**, 210401 (2001).
- [127] H. Moritz, T. Stoferle, M. Kohl, and T. Esslinger, “Excited collective oscillations in a trapped 1D gas,” *Phys. Rev. Lett.* **91**, 250402 (2003).
- [128] T. Kinoshita, T. R. Wenger, and D. S. Weiss, “Observation of a one-dimensional Tonks-Girardeau gas,” *Science* **305**, 1125 (2004).
- [129] B. Paredes, A. Widera, V. Murg, O. Mandel, S. Fölling, I. Cirac, G. V. Shlyapnikov, T. W. Hansch, and I. Bloch, “3D lattice tonks with one weak lattice,” *Nature* **429**, 277 (2004).
- [130] D. W. Keith, C. R. Ekstrom, Q. A. Turchette, and D. E. Pritchard, “An Interferometer for Atoms,” *Phys. Rev. Lett.* **66**, 2689 (1991).
- [131] A. Trombettoni, A. Smerzi, and P. Sodano, “Observable Signature of the Berezinskii-Kosterlitz-Thouless Transition in a Planar Lattice of Bose-Einstein Condensates,” *New Journal of Physics* **7**, 57 (2005).
- [132] T. Esslinger, M. Weidemüller, A. Hemmerich, and T. Hänsch, “Surface-plasmon mirror for atoms,” *Opt. Lett.* **18**, 450 (1993).
- [133] C. Aminoff, A. Steane, P. Bouyer, P. Desbiolles, J. Dalibard, and C. Cohen-Tannoudji, “Cesium Atoms Bouncing in a Stable Gravitational Cavity,” *Phys. Rev. Lett.* **71**, 3083 (1993).
- [134] Y. B. Ovchinnikov, I. Manek, and R. Grimm, “Surface trap for Cs based on evanescent-wave cooling,” *Phys. Rev. Lett.* **79**, 2225 (1997).
- [135] M. Hammes, D. Rychtarik, V. Druzhinia, U. Moslener, I. Manek-Hönninger, and R. Grimm, “Optical and evaporative cooling in the gravito-optical surface trap,” physics/0005305 (2000) subm. to *Journal of Modern Optics* (2005).
- [136] D. Schneble, H. Gauck, M. Hartl, T. Pfau, and J. Mlynek, in Ref. [71] (PUBLISHER, ADDRESS, YEAR), pp. 469–490.
- [137] D. Schneble, H. Gauck, M. Hartl, T. Pfau, and J. Mlynek, in *Bose-Einstein Condensation in Atomic Gases, Proceedings of the International School of Physics “Enrico Fermi” Course CXL*, edited by M. Inguscio, S. Stringari, and C. E. Wieman (IOS Press Amsterdam, ADDRESS, 1999, and references therein), pp. 469–490.
- [138] R. J. C. Spreeuw, D. Voigt, B. T. Wolschrijn, and H. B. van Linden van den Heuvell, “Creating a low-dimensional quantum gas using dark states in an inelastic evanescent-wave mirror,” *Phys. Rev. A* **61**, 053604 (2000).
- [139] O. Zobay and B. M. Garraway, “Two dimensional atom trapping in Field-Induced adiabatic potentials,” *Phys. Rev. Lett* **86**, 1195 (2001).

- [140] Y. Colombe, E. Knyazchyan, O. Morizot, B. Mercier, V. Lorent, and H. Perrin, “Ultracold atoms confined in rf-induced two-dimensional trapping potentials,” *Europhys. Lett.* **67**, 593 (2004).
- [141] E. A. Hinds, M. G. Boshier, and I. G. Hughes, “Magnetic waveguide for trapping cold atom gases in two dimensions,” *Phys. Rev. Lett.* **80**, 645 (1998).
- [142] T. P. Simila, M. D. Lee, and D. A. W. Hutchinson, “Transition from a Bose-Einstein condensate to Berezinskii-Kosterlitz-Thouless Phase,” (2004), cond-mat/0412512.
- [143] J. M. Kosterlitz and D. J. Thouless, “Ordering, metastability and phase transitions in two-dimensional systems,” *J. Phys. C* **6**, 1181 (1973).
- [144] J. M. Kosterlitz, “The critical properties of the two-dimensional xy model,” *J. Phys. C* **7**, 1046 (1974).
- [145] D. J. Bishop and J. D. Reppy, “Study of the superfluid transition in two-dimensional $^4\text{Helium}$ films,” *Phys. Rev. Lett* **40**, 1727 (1978).
- [146] D. J. Bishop and J. D. Reppy, “Study of the superfluid transition in two-dimensional $^4\text{Helium}$ films,” *Phys. Rev. B* **22**, 11 (1980).
- [147] A. I. Safonov, S. A. Vasilyev, I. S. Yasnikov, I. I. Likashevich, and S. Jaakkola, “Observation of Quasicondensate in Two-Dimensional Atomic Hydrogen,” *Phys. Rev. Lett* **81**, 4545 (1998).
- [148] T. McMillan, P. Taborek, and J. E. Rutledge, “Ellipsometric study of superfluid onset in thin films of $^4\text{Helium}$ films,” *J. Low Temp. Phys* **134**, 303 (2004).
- [149] A. Nesmeianov, *Vapour pressure of the elements*. (New York Academic Press, Oxford, UK, 1963).